THE UNIVERSITY OF MANITOBA

A CORRELATION STUDY OF THE BREAK-UP OF TRIONS INDUCED BY 45 MEV PROTONS

by

E. S. Y. Tin

A THESIS

SUBMITTED TO THE FACULTY OF GRADUATE STUDIES

IN PARTIAL FULFILMENT OF THE REQUIREMENTS FOR THE DEGREE

OF DOCTOR OF PHILOSOPHY

DEPARTMENT .....PHYSICS.....

WINNIPEG, MANITOBA

May, 1974

A CORRELATION STUDY OF THE BREAK-UP OF TRIONS INDUCED BY 45 MEV PROTONS

by

E.S.Y. TIN

A dissertation submitted to the Faculty of Graduate Studies of the University of Manitoba in partial fulfillment of the requirements of the degree of

DOCTOR OF PHILOSOPHY

ABSTRACT

The $^3H(p,2p)nn$, $^3H(p,pd)n$, $^3He(p,2p)d$ and $^3He(p,2p)pn$ reactions have been studied at an incident proton energy of 45 MeV at a variety of coplanar symmetric and asymmetric angle pairs.

Momentum distributions of the d and [nn] systems in ^3H and of the d and d* systems in ^3He have been extracted within the framework of the Plane Wave Impulse Approximation. d* and [nn] respectively refers to a n-p and n-n pair with low energy for their relative motion. Good agreement can be obtained for the shape of the momentum distributions if an Irving-Gunn wave function is used for the tri-nucleon (trion) system. However, a cut-off radius is found to be necessary for the reactions $^3H(p,pd)n$ and $^3He(p,2p)d$. The shape of the angular correlation momentum distribution for the $^3H(p,2p)[nn]$ reaction is sensitive to the approximation used for the off-the-energy-shell scattering amplitude.

The PWIA predicts cross sections which are typically a few times greater than the experimental ones indicating the presence of multiple scattering effects. Shifts are observed in the positions of the quasi-free scattering peaks in the $^3H(p,pd)n$ reaction which might be attributable to the neutron pick-up process.

The Watson-Migdal model fails to explain the final state interaction between the unobserved pair of nucleons for both the $^3H(p,2p)nn$ and $^3He(p,2p)pn$ reactions.

Comparison of the continua for the $^3H(p,2p)nn$ reaction with four-body differential phase space distributions shows no evidence for a resonance in the ^3H system but reveals some hitherto unobserved pseudo two-body processes, namely the p-d* quasi-free scattering process and the $p + t \longrightarrow d^* + d^*$ reaction.

ACKNOWLEDGEMENTS

The author is indebted to the participants of this project for their assistance and suggestions. These include Drs. D.I. Bonbright, S.A.Elbakr, A.Houdayer, C.A.Miller, W.T.H.van Oers and J.W.Watson and Mr. D.J.Roberts.

In particular, Dr. Bonbright's expertise in theoretical methods and Dr. Miller's ingenuity with computer software contributed much to the early completion of this work.

The continual guidance and encouragement offered by Dr. van Oers at various stages of this project is also gratefully acknowledged.

CONTENTS PAGE

PAGE

1. INTRODUCTION

1.1 Nuclear forces and the few-nucleon problem

Since the discovery of the neutron in 1932 and the realization that the nucleus is composed of spin ½ protons and neutrons, the search for an understanding of the forces which bind the nucleus became a major part of nuclear physics. It became clear shortly afterwards that the nuclear force is exceedingly complicated compared to the electromagnetic forces, being strong, short-range, non-local, spin dependent, charge symmetric and to a large extent charge independent; specifically, the nuclear part of the n-n, n-p and p-p interactions being identical in identical spin and space states. Yukawa (Yu35) in 1935 showed that a strong short-range force could be interpreted as due to the existence of finite mass quanta strongly coupled to the nucleons. Such quanta were indeed found and turned out to be the pi-mesons. This theoretical insight did not however lead rapidly to a quantitative understanding of the nuclear force. Instead, the development in the understanding of nuclear forces proceeds in two separate ways, one is the so-called phenomenological approach involving phase-shift and potential parametrizations of nucleon-nucleon (N-N) scattering data, the other is the meson-theoretic approach in which the nuclear interaction is treated as arising from exchanges of pions and other bosons.

It is true that great progress has been made in both approaches and that a great deal has been learned about the two-nucleon problem. The understanding of the nuclear interaction is still inadequate in the following aspects:

1. Explanation of the repulsive core in terms of meson exchanges.
2. The nucleon-nucleon off-the-energy-shell interaction.
3. The degree of validity of charge symmetry and charge independence of nuclear forces.
4. The significance of three-body and many-body forces.

Studies of nucleon-nucleon bremsstrahlung and nuclear reactions leading to three or four particles in the final state might shed light on some of these problems. Extensive work has already been done in both studies and valuable information obtained. In particular, since the three-body problem can be solved exactly using the Faddeev formalism (Fa60), one can test the validity of many approximations and models of the nucleon-nucleon interaction by studying reactions involving break-up of the lightest nuclei. Indeed, remarkable agreement has been obtained in fitting the nucleon-deuteron break-up data with the Faddeev formalism in which the nucleon-nucleon interaction is assumed to be represented by a separable potential (Am63, Aa64, Aa65, Or69, Ca70). A review of the recent development in low and medium energy few-nucleon systems may be found in the Proceedings of the International Conference on Few Particle Problems in the Nuclear Interaction (Fe72).

1.2 Multiparticle reactions

Any reaction leading to three or more particles in the final state may exhibit peaks in the energy spectra of the emitted particles due to one or more of several processes (Sl70). Fig.1.2.1 shows the various processes leading to a three-body final state. Process (a) is a quasi-elastic process, more often called quasi-

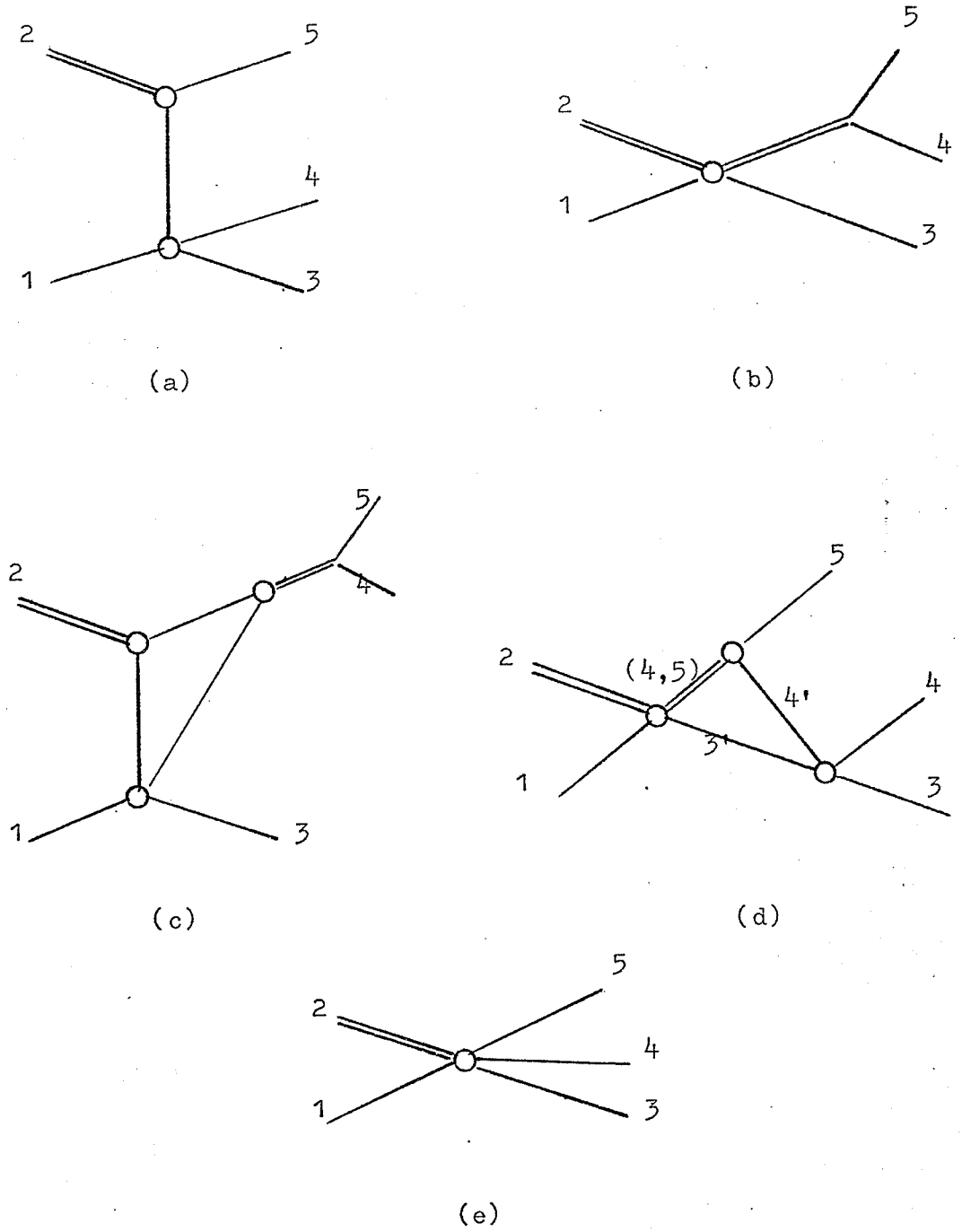

Fig.1.2.1: Diagrams representing various processes leading to a three-body final state from the reaction $1 + 2 \longrightarrow 3 + 4 + 5$ (a) quasi-free scattering (b) sequential break-up (c) quasi-free scattering followed by final state interaction (d) sequential decay followed by rescattering (e) simultaneous break-up.

free scattering (QFS) in which the projectile interacts primarily with a single constituent of the nucleus leaving the residual particle with the momentum it had inside the target nucleus before the interaction took place. This momentum is in general small and the residual particle is therefore called the spectator particle in the laboratory system. Process (b) is a sequential break-up process in which two of the emerging particles interact strongly with each other in the final state compared with their interactions with the third particle. One may distinguish nucleon-nucleon final state interactions (FSI) and sequential decay through particle unstable nuclear states. In the case of N-N final state interactions, the strong interaction of a nucleon-nucleon pair occurs with a low energy for the relative motion of the two nucleons whereas the delay in the decay of a nuclear particle unstable state is characterized by the energy width of the state and by barrier penetration effects (B152). Process (c) represents quasi-free scattering followed by a final state interaction (Cr61, Cr63). Process (d) represents the first of an infinite series of rescattering corrections. In this particular case, in terms of a classical picture, particle 3' and resonance (4,5) travel in opposite directions in their overall centre of mass system. Resonance (4,5) decays into particles 4' and 5 after a time determined by its lifetime. If particle 4' is emitted in the direction of 3' and has a higher velocity, it can catch up to and scatter from particle 3'. Such an effect, if kinematically allowed, should be observable and can in fact be used to estimate the lifetime of resonance (4,5) (Fo62). Process (e), a simultaneous break-up process, is a direct reaction in which

the three particles emerge simultaneously in the final state. In the absence of resonant processes and if the scattering matrix elements are independent of momentum transfer variables, the distribution of events is given by the available phase space (Ha64). A more detailed discussion of phase space will be given in Ch. 2.

1.3 Status of available data

Coincidence studies of nucleon induced break-up of the trion (^{3}He and ^{3}H) began a few years ago but because of the extra precaution that is needed in handling radioactive tritium targets, the data are essentially limited to the break-up of ^{3}He. These include studies of the ^{3}He(p,2p)d and ^{3}He(p,pd)p reactions at 35 MeV by Slaus et al.(Sl71), at 45 MeV by Jain et al. (Bu72, Ja74), at 65 MeV by Pugh et al. (Pu74), at 155 MeV by Frascaria et al. (Fr71, Fr74) and at 590 MeV by Kitching et al. (Ki72).

There also exist data on the ^{1}H(^{3}He,pd)p and ^{1}H(^{3}He,pp)d reactions at 69 MeV by Wielinga et al. (Wi72) and the reaction ^{2}H(^{3}He,tp)p at 27 MeV by Warner et al. (Wa71). Studies of the ^{3}He(p,2p)d^* reaction have been made at 45 MeV (Ja74) and at 155 MeV (Fr71). Here d^* refers to a ^1S_o n-p pair with low relative energy.

On the other hand, the only existing data on the break-up of tritium are those of Slaus et al. (Sl73) in which ^{3}He particles and deuterons were used as bombarding particles and those of Fritts et al. (Fr72) who investigated the ^{3}H(p,2p)nn reaction at 20 MeV in a comparative study with the ^{3}He(p,2p)pn reaction.

Due to the complexity of the reactions, most of the above experiments were designed such that kinematical conditions satisfied either quasi-free scattering or final state interaction processes. The quasi-free scattering data have generally been analysed in the framework of the plane wave impulse approximation (PWIA) (see chapter 2). The most important conclusion of these analyses is that the behavior of the QFS peak is extremely sensitive to the asymptotic form of the ^{3}He wave function in coordinate space. In general, the PWIA gives good agreement with the shape and position of the QFS peak if ^{3}He wave functions with appropriate tails are used but predicts cross sections considerably larger than the experimental values. The extent of the discrepancy increases as the incident energy decreases. It is not surprising that such a discrepancy should exist since the PWIA is only an approximation to the single-scattering contribution in the quasi-free scattering process. This suggests that double and higher order scattering processes reduce the cross section. In terms of the Faddeev formalism, such interactions correspond to the higher order terms in the multiple scattering series generated by iterating the Faddeev equations. A number of phenomenological models has been used with varying degree of success to simulate such multiple scattering corrections. These include:

1. The introduction of an adjustable cut-off radius in the overlap function calculated in the PWIA (Ma70, Sl71, Ja74).
2. The use of distorted waves in both the initial and final state (Fr71, Fr74) resulting in the distorted wave impulse approxi-

mation (DWIA).

3. The attenuation model (Ro72, Ha73) in which rescattering is interpreted as an attenuation due to the emerging particle scattering from the spectator particle after it has undergone quasifree scattering. Such a secondary scattering will remove particles from the QFS kinematic region.

The only analysis of the three-body break-up of ^{3}He by nucleons has been that performed by Lehman (Le72). He analysed Frascaria's data at 155 MeV in the pole-dominance approximation with final-state rescattering included between the spectator nucleons (i.e. the p-n pair in ^{3}He(p,2p)pn) and found that final-state rescattering reduces the cross section by a factor of two with the shape remaining effectively unaltered. In Lehman's approach, the break-up reaction is represented by pole diagrams (see Fig.1.2.1) and the coincidence cross section is given in terms of the amplitudes for all the important pole diagrams present. The vertices of a given pole diagram are calculated from wave functions derived from a separable-potential model of the two-nucleon interaction. This approach permits cross section predictions to be made which are independent of other three-body data and further allows the final state rescattering between the spectator particles to be treated in a consistent manner.

It must be mentioned that prior to studies of the kind mentioned above, much information about the three-nucleon system has been gained through studies of photodisintegration and electrodisintegration on ^{3}He and ^{3}H. The advantage of using gamma rays

and electrons over nucleons as incident particles is that there is no additional complication connected with the strong interaction between the incident particle and the target nucleus. Moreover, the electromagnetic interaction, known with high accuracy, permits the application of perturbation theory. In photodisintegration studies, the quantity generally measured is the total cross sections for the reactions (γ,p) and (γ,n) on ^3He and ^3H in the gamma energy range from threshold to about 150 MeV (Fe65). The simplicity of the production mechanism is a consequence of the dominance of electric dipole (E1) transitions. However, the form of the operator $\vec{E}\cdot\vec{r}$ implies that such reactions are to a large extent independent of the detailed properties of the three-nucleon ground state and any reasonable wave function with the correct rms radius is sufficient. This is indeed found to be so from early calculations for the two-body break-up channel (e.g. $^3He(\gamma,p)d$). However, similar approaches to the three-body channel (e.g. $^3He(\gamma,p)pn$) showed a sharp discrepancy between experiment and theory, the calculated cross sections being as much as three times the experimental values (Fe65). In a recent paper, Barbour and Phillips (Ba70) were able to show that the analytic and asymptotic form of the wave function, short-range correlations, and the S'-state admixture all have minor effects on the total cross section; the latter being crucially dependent on the nuclear interaction in the final continuum state. Moreover, by using a reasonable three nucleon bound state wave function and describing the final states by the Faddeev equations in the separable approximation, the same authors were able to

obtain a rough but nonetheless simultaneous agreement for the total two-and three-body break-up cross sections and the charge form factors of the three particle nuclei.

Electron scattering appears to be a much more powerful tool to probe the structure of the trions and to provide detailed information about the three-nucleon ground state. The electric and magnetic form factors have been measured by elastic electron scattering (Co63, Co65) for both ^{3}He and ^{3}H. To explain the observed difference between the electric and magnetic form factors, it was found (Sc64) necessary to introduce an admixture of the S' state (S state of mixed symmetry) to the completely symmetrical S state. The amount of admixture required depends to a large extent on the type of wave function used. A recent electron scattering experiment (Mc70) has yielded the ^{3}He charge and magnetic form factors for momentum transfers up to 20 fm^{-2} and showed a deep minimum at q^2= 11.6 fm^{-2} in the charge form factor. Using phenomenological S' and D-state wave function components (Mc70b) along with the symmetric S-state component developed from the Bressel-Kerman-Rouben (Br69) soft-core potential using an altered Feshbach-Rubinow (Fe55) equivalent two-body method, McMillan (Mc71) was able to reproduce the minimum with $P_{S'}$ = 2% and P_D = 9%. Although a great amount of work has been done both experimentally and theoretically on elastic electron scattering, work on inelastic electron scattering from ^{3}He and ^{3}H are much more sparse (Jo64, Hu66). In principle, coincidence measurement of the quasi-free electron-proton scattering in ^{3}H and ^{3}He should be sensitive to the wave function of a proton

inside the nucleus. However, because of the exceedingly low cross section for this reaction, existing data (Jo64) do not have sufficient statistics to allow any conclusive remarks to be made about the small-components of the ground-state wave function. Calculation of the coincidence cross section has been performed by Griffy and Oakes (Gr64), Gibson and West (Gi67) and Lehman (Le71) in the impulse approximation. In these calculations, good agreement was obtained for the two-body break-up data if the ground-state ^{3}He wave function had the correct asymptotic behavior. As already mentioned, Lehman used a model in which wave functions were derived from separable potentials thus allowing the three-body break-up cross section to be treated consistently. Just as in the ^{3}He(p,2p)pn reaction, rescattering corrections between the spectator particles were found to be important in calculating three-body electrodisintegration.

1.4 Objectives of the present experiment

In this work, a correlation study has been made on the break-up of trions induced by 45 MeV protons. The reactions that we have studied in detail are:

^{3}H(p,2p)nn at 45.75 MeV	Q = -8.482 MeV	I
^{3}H(p,pd)n at 45.75 MeV	Q = -6.258 MeV	II
^{3}He(p,2p)d at 45.00 MeV	Q = -5.494 MeV	III
^{3}He(p,2p)pn at 45.00 MeV	Q = -7.718 MeV	IV

Reactions I and II have been performed at a variety of coplanar angle pairs. Reactions III and IV have only been studied at one

angle pair since data at other angle pairs have already been obtained earlier in this laboratory (Bu72, Ja74). This one angle pair was chosen so that the spectator (a n-p pair with zero relative energy) has zero laboratory momentum. In addition, a very careful study has been made of the ^{3}H(p,2p)[nn] and ^{3}He(p,2p)d* reactions. The symbol [nn] is used to denote a ^1S_o n-n pair with low energy for their relative motion. The objectives of these studies are five fold:

1. To investigate in a 'kinematically complete' way the reaction mechanisms for the break-up of ^{3}H induced by protons in various regions of phase space.

2. To extract the momentum distribution of the proton and of the deuteron in ^{3}H from the ^{3}H(p,2p)[nn] and ^{3}H(p,pd)n reactions, respectively. An analysis using the PWIA may then provide information on the ^{3}H ground state wave function. It was already indicated that the shape of the momentum distribution is very sensitive to the asymptotic form in coordinate space of the dominant S-state component of the trion wave function. It would be interesting to see if the small component (S'- and D-state) contributions would manifest themselves within the range of momentum transfer studied in the present experiment.

3. To examine to what extent the p-p interaction is off-the-energy-shell in the ^{3}H(p,2p)[nn] reaction.

4. To search for possible excited states or resonances in the ^{3}H system by comparing the measured four-body continua from the ^{3}H(p,2p)[nn] reaction with phase space predictions.

5. From a detailed comparison of the $^{3}H(p,2p)nn$ and $^{3}He(p,2p)pn$ reactions, performed under identical kinematical conditions, to extract possibly the low-energy nucleon-nucleon scattering parameters(in particular a_{nn}) from an analysis based on the Watson-Migdal model. At low nucleon-nucleon relative energies, only S-waves are of importance. Moreover, since the $^{1}S_{o}$ (singlet) state is almost bound, the scattering length is very sensitive to the strength of the potential. In the effective range approximation, a relative change in the depth of a potential V is related to a relative change in the singlet scattering length and the effective range by the expression (Ma64):

$$\frac{\Delta V}{V} = A\frac{\Delta a}{a} + B\frac{\Delta r_o}{r_o}$$

where A is ~ 0.1 and B is relatively shape independent. A 2% increase in V will produce a 20% decrease in a but only a 1% decrease in r_o. Table 1.1 summaries the currently known reliable effective range parameters for the $^{1}S_{o}$ nucleon-nucleon system (He72).

Table 1.1

Effective Range Parameters for the $^{1}S_{o}$ nucleon-nucleon system

	Experiment	a (fm)	r_o (fm)	Ref.
pp	$^{1}H(p,p)^{1}H$	-7.817 ± 0.007	2.810 ± 0.018	(Gu64,No64,He67)
np	$^{1}H(n,n)^{1}H$	-23.715 ± 0.013	2.758 ± 0.003	(No63,No68)
nn	$D(\pi^-,\gamma)2n$	-16.4 ± 1.6		(Sa72)
	$D(n,2n)p$	-17.1 ± 0.8	3.4 ± 0.6	(Ze72)
		-16.0 ± 1.2		(Br72)
	$^{3}H(t,\alpha)2n$	-17.0 ± 0.5		(Gr70)
		-15.0 ± 1.0		(Ku72)
	Average	-16.4 ± 0.2		(He72)
$(nn)^{pp}$		-17.1 ± 0.2		(Mi69,Sh70,He69)
$(nn)^{np}$		-23.72		(Sh70)

Elastic scattering experiments provide accurate determinations of both the n-p and p-p scattering lengths but because of the lack of suitable free neutron targets, values of a_{nn} have generally been extracted via final-state interactions, analysed in terms of the Watson-Migdal model or Born approximation. Due to the form of the effective range expansion, N-N final-state interactions are less suitable to extract r_{nn}. A value of $r_{nn} \sim 2.6\text{-}3$ is generally assumed in extracting a_{nn}. An exception is the $D(\mu^-,\nu)2n$ reaction which at present is still the most promising candidate for an accurate determination of r_{nn}. It should be mentioned that the analyses of FSI are rather model dependent (Oe71). However, a comparison procedure in which all the reactions leading to the members of the nucleon-nucleon isospin triplet and a specified third particle are studied, allows a test of the reliability of the n-n scattering parameter extracted (e.g. simultaneous studies of the reactions $^3He(p,d)2p$, $^3He(n,d)np$, $^3H(p,d)np$ and $^3H(n,d)2n$). The most reliable experimental value for a_{nn} comes from the $D(\pi^-,\gamma)2n$ reaction. It is noteworthy that in order to determine a_{nn} to $\pm$ 0.5fm from break-up reactions, the relative differential cross sections should be known to $\pm$ (1-2)% and the energy calibration to $\pm$ 20 keV (Oe67).

The value a_{nn}^{pp} represents the n-n scattering length derived from a_{pp} after correction for the Coulomb potential, the vacuum polarization effects and the neutron-proton mass difference, the magnitude of the corrections being dependent on the nuclear potential used in the calculation. The difference between a_{nn} and a_{nn}^{np} ($\sim$1 fm) implies a weaker n-n than p-p interaction. However, in

view of the theoretical and experimental uncertainties, no statement about symmetry breaking should be made. The value of $a_{nn}^{np} = -23.72$ fm shows clearly that charge-independence breaking effects are present even after direct electromagnetic corrections are carried out.

Charge-symmetry and charge-independence breaking of the nuclear force can occur in a variety of ways. These include the 'direct' electromagnetic effects which are present even when the hadronic forces are turned off:

1. Electrostatic interaction between two point charges in the case of the p-p system.
2. Modification of the Coulomb potential due to the vacuum polarization.
3. The magnetic interactions of the spin-orbit and moment-moment types.
4. The finite size of the nucleons and the neutron-proton mass difference.

The 'indirect' electromagnetic effects, which are absent when the hadronic forces are turned off, include:

1. The mass difference of neutral and charged mesons which are exchanged between the nucleus.
2. The mass differences of baryons (including the nucleons) which occur in the exchange of more than one meson.
3. Radiative corrections to the meson-nucleon coupling constants.
4. Isovector-isoscalar meson mixing effects, e.g. ρ-ω mixing and π-η mixing. Henley and Keliher (He72b) estimated the last effect to make a correction of $\sim$1 fm to the value of a_{nn}.

2. THEORY

2.1 Kinematics and phase space

Kinematics

Since no standard convention exists for denoting the various variables necessary to describe the three body kinematics, it is essential at the onset to give the convention that we have adopted. Fig.2.1.1 depicts the situation of a three body reaction 1 + 2 --> 3 + 4 + 5 and summarises the notation that we will use for the different variables. Except where specified, relativistic kinematics has been used throughout this thesis.

If the mass of a particle is known, its 4-momentum has three independent components related by $E^2 = (pc)^2 + m^2c^4$. Thus, for a three body reaction in which there are three particles in the final state of known masses, we require nine kinematical variables to completely specify the motion in the final state. Conservation of 4 - momentum provides four constraints, leaving five independent variables to be measured. A kinematically complete experiment is one in which all the five variables are measured. Experimentally, the variables determined are usually the polar angles θ_3 and θ_4, the azimuthal angle ϕ_{34}, the kinetic energies T_3 and T_4, thus requiring a coincidence measurement. In general, for reactions with N particles of known masses in the final state, 3N - 4 independent variables are needed to completely specify the kinematics. In kinematically incomplete experiments, an implicit integration over several kinematical variables is made. This integration makes the interpretation of the data rather difficult. A discussion of the limit-

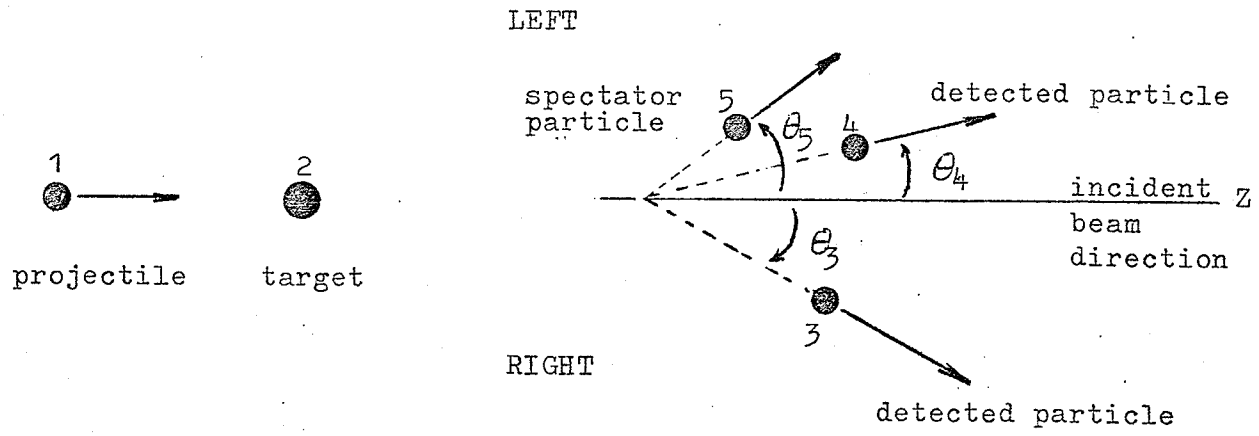

Initial State

Final State

$\phi_{ij} = \phi_j - \phi_i$ ($\phi_{ij} = 180^\circ$ represents particles i and j to be coplanar and on opposite sides of the incident beam)

E = Total energy in the laboratory system

T = Kinetic energy in the laboratory system

m = Rest mass

$\vec{p} = \hbar\vec{k}$ (where $\vec{k}$ is the wave vector in the laboratory system) represents the momentum vector in the laboratory system

p = magnitude of the momentum

T_{ij} = Relative energy of particles i and j

M_{ij} = Invariant mass of particles i and j

$\vec{q} = -\vec{p}_5$ represents the momentum transfer vector

$q = |\vec{q}|$ is arbitrarily assigned a positive/negative value if particle 5 is emitted in the positive/negative Z-direction or in the opposite/same side as particle 3.

T_{inc} = Kinetic energy of the incident beam in the laboratory system. $T_1 = T_{inc}$ in the absence of any degrader

Fig.2.1.1 Convention adopted for the kinematics of a three-body reaction 1 + 2 ---> 3 + 4 + 5

ations of kinematically incomplete experiments can be found in references (S167, S170, Oe67).

A two-dimensional plot of the kinetic energies of the two detected particles generates a locus characteristic of the reaction, each point of which corresponds to a particular value of the relative energy of any pair of the three particles in the final state. Details of the equations relating the various kinematic variables can be found in references (Ha64, Wa70). In a reaction where there are four particles in the final state, the undetected pair is treated as a single particle (particle 5) such that T_5 represents the laboratory kinetic energy of the overall centre-of-mass of the undetected pair while T_{56} represents the relative energy of the undetected pair. A four-body decay may be viewed as a series of three-body loci with varying invariant masses (or equivalently relative energies since $T_{56} = M_{56} - m_5 - m_6 = \Delta M$) of the undetected two-body system. In particular, at the spectator angle pair where T_5 is kinematically allowed to reach zero, the experiment effectively detects three particles since the relative momentum between a particle in the pair and either one of the undetected particles is constrained. Fig.2.1.2 shows the kinematic loci for the $^3H(p,2p)nn$ reaction for different symmetric coplanar angle pairs. Each curve corresponds to the boundary of the allowed four-body decay region. Four-body decay is allowed anywhere inside the T_3 versus T_4 locus. The behavior of the T_3 versus T_4 locus for different relative energies of the spectator pair is shown in Fig.2.1.3(a) for $\theta_3 = \theta_4 = 38^\circ$, $\phi_{34} = 180^\circ$ which is the symmetric spectator angle pair. Fig.2.1.3(b) shows the behavior of the T_3 versus T_5 (5 refers to the n-n spectator pair) curves for different relative energies of the spectator pair. It is seen that the T_5 minimum is broad for contours of low ΔM (or T_{56}). This implies that at the spectator angle pair the relative energies between the

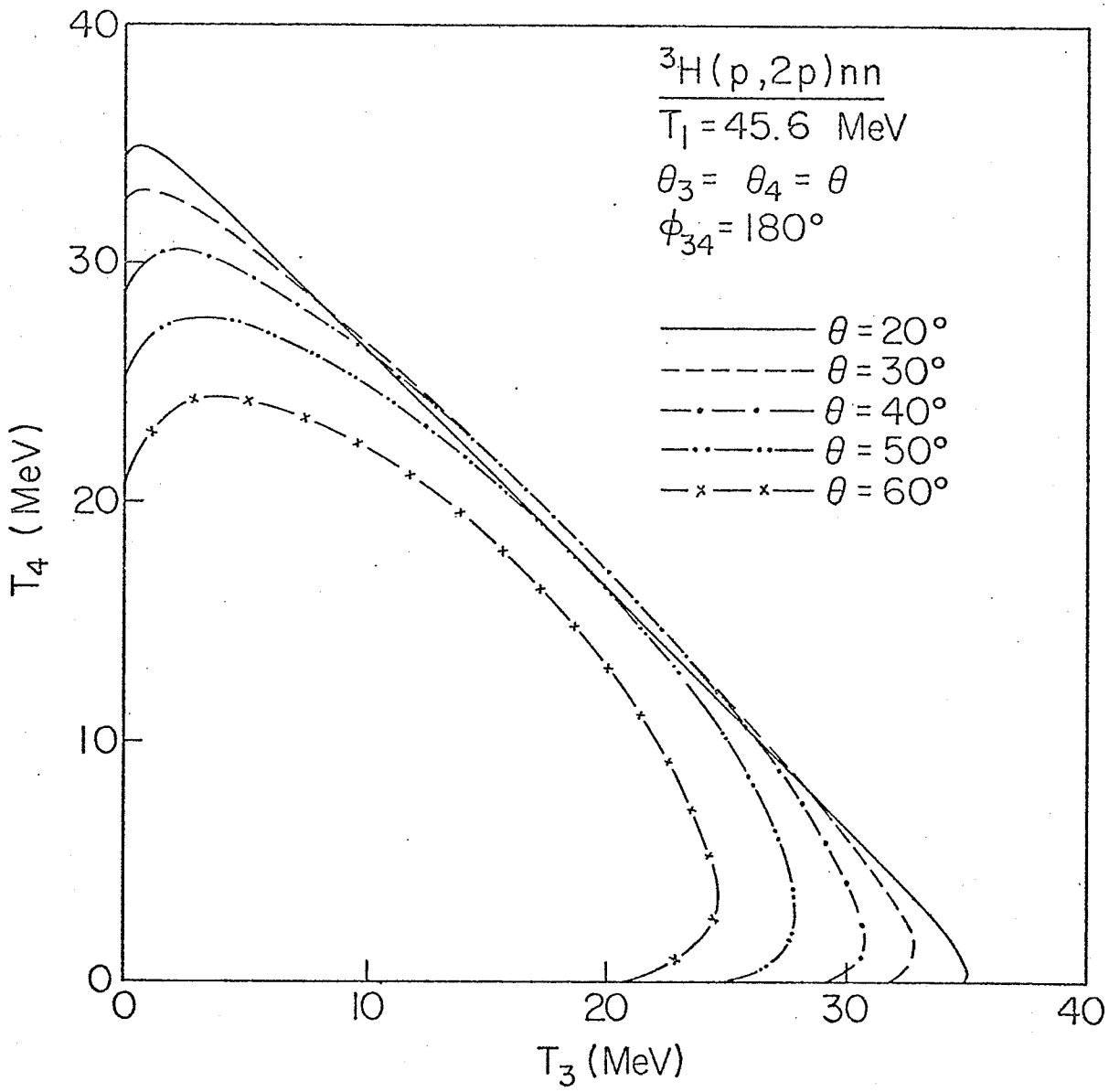

Fig.2.1.2 Kinematics for the ^{3}H(p,2p)nn reaction for different symmetric coplanar angle pairs. Each curve corresponds to the boundary of the allowed four-body decay region.

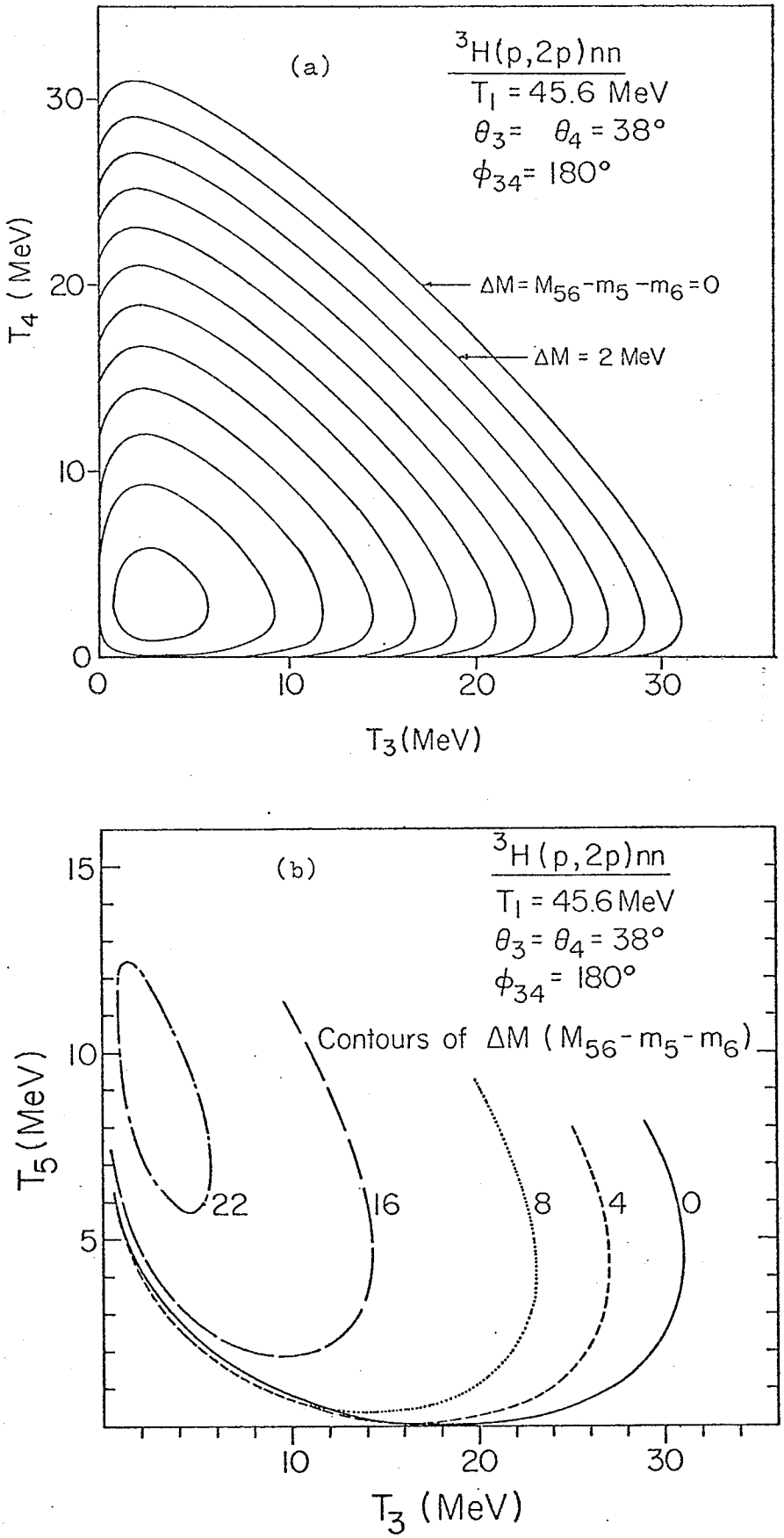

Fig.2.1.3: Behavior of the T_3 versus T_4 (a) and T_3 versus T_5 (b) kinematic loci for different relative energies between the unobserved particles. Angles depicted being the symmetric spectator angle pair.

detected particles (proton) and either one of the particles of the undetected spectator pair (n-n) is high; final state interactions between the proton and neutron are therefore expected to be unimportant in the region near minimum M_{56}. The dominant final-state interaction is that between the undetected particles and in fact constitutes one of the rescattering corrections to the QFS process. For angle pairs other than the spectator angle pair, the minimum in T_5 no longer reaches zero and becomes less broad.

Phase Space

The total phase space volume available to a reaction is determined by the kinematics of the reaction. The phase space density (phase space for short) as a function of a given kinematical variable (e.g. momentum) is governed by the requirements of energy and momentum conservation. Physically, it represents the statistical probability of an event yielding a state with the i^{th} (i=1,2,-- n) particle in momentum range $d\vec{p}_i$. Further, if the transition matrix element for the reaction (representing the dynamical effects) is independent of the momentum variables, the phase space distribution alone will determine the distribution of events of that reaction. The transition probability for a reaction of the type $1+2 \longrightarrow 3+4+5+---n$ is related to the T-matrix by Fermi's golden rule No.2

$$W = \frac{2\pi}{\hbar} |T|^2 R(E) \qquad (1)$$

where T is the Lorentz invariant transition matrix element and R(E) is the Lorentz invariant phase space. For a system of n-2 particles in the final state of total momentum $\vec{P}$ and total energy E, the phase space is usually defined as

$$R_{n-2}(\vec{P},E) = \int \prod_{i=3}^{n} \left[d^4 q_i \, \delta(q_i^2 - m_i^2) \right] \delta^4\left(\sum_{i=3}^{n} q_i - Q \right) \qquad (2)$$

where $q = (\vec{p}_i, E_i)$ is the four-momentum for particle i, and $Q = (\vec{P},E)$. q^2 is understood to be $= E_i^2 - p_i^2$ ($= m_i^2$). Integrating over all E_i yields (Sk64, Zu64, Oe73)

$$R_{n-2}(\vec{P},E) = \int \prod_{i=3}^{n} \frac{d^3p_i}{2E_i}\, \delta^3\Big(\sum_{i=3}^{n}\vec{p}_i - \vec{P}\Big)\, \delta\Big(\sum_{i=3}^{n} E_i - E\Big) \qquad (3)$$

The factor $2E_i$ enters from a normalization of the wave function in field theory. Equation (3) can be written as

$$R_{n-2}(\vec{P},E) = \int \frac{d^3p_3}{2E_3}\,\frac{d^3p_4}{2E_4} \int \prod_{i=5}^{n} \frac{d^3p_i}{2E_i}\, \delta^3\Big(\sum_{i=5}^{n}\vec{p}_i - (\vec{P}-\vec{p}_3-\vec{p}_4)\Big)$$

$$\delta\Big(\sum_{i=5}^{n} E_i - (E-E_3-E_4)\Big)$$

$$= \int \frac{d^3p_3}{2E_3}\,\frac{d^3p_4}{2E_4}\, R_{n-4}(\vec{P}-\vec{p}_3-\vec{p}_4,\ E-E_3-E_4) \qquad (4)$$

Since R_{n-4}, the phase space for the undetected particles is also invariant, one can write in the c.m. system of the undetected particles

$$R_{n-2}(\vec{P},E) = \int \frac{d^3p_3}{2E_3}\,\frac{d^3p_4}{2E_4}\, R_{n-4}(0,\varepsilon) \qquad (5)$$

where $\varepsilon^2 = (E-E_3-E_4)^2 - (\vec{P}-\vec{p}_3-\vec{p}_4)^2 = M^2_{56---n}$ (6)

which is the invariant mass of particles 5,6,---- and n once $\vec{p}_3$ and $\vec{p}_4$ are given. Thus one has for the three-body phase space:

$$R_3(\vec{P},E) = \int \frac{d^3p_3}{2E_3}\,\frac{d^3p_4}{2E_4}\, R_1(0,\varepsilon)$$

with $R_1(0,\varepsilon) = \delta(\varepsilon^2 - m_5^2)$ (7)

Similarly one has for the four body phase space:

$$R_4(\vec{P},E) = \int \frac{d^3p_3}{2E_3}\,\frac{d^3p_4}{2E_4}\, R_2(0,\varepsilon)\ , \qquad (8)$$

where $R_2(0,\varepsilon)$ represents the two-body phase space for a system of two particles (the undetected pair) with masses m_5 and m_6 and with a total energy $\varepsilon = M_{56}$. It is relatively easy to show (see Appendix I) that

$$R_2(0,M_{56}) = \frac{\pi}{2M_{56}^2}\left\{\left[M_{56}^2 - (m_5+m_6)^2\right]\left[M_{56}^2 - (m_5-m_6)^2\right]\right\}^{1/2} \qquad (9)$$

Hence we have for the four body phase space:

$$R_4(\vec{P},E) = \frac{d^3p_3}{2E_3}\frac{d^3p_4}{2E_4}\frac{\pi}{2M_{56}^2}\left\{\left[M_{56}^2 - (m_5+m_6)^2\right]\left[M_{56}^2 - (m_5-m_6)^2\right]\right\}^{\frac{1}{2}} \qquad (10)$$

and for the differential phase space distribution:

$$\frac{dR_4(\vec{P},E)}{dE_3 d\Omega_3 dE_4 d\Omega_4} = \frac{\pi p_3 p_4}{8 M_{56}^2}\left\{\left[M_{56}^2 - (m_5+m_6)^2\right]\left[M_{56}^2 - (m_5-m_6)^2\right]\right\}^{\frac{1}{2}} \qquad (10a)$$

In the absence of resonant processes and when the T-matrix is not a function of the way the energy is distributed among the emerging particles, the distribution of events in the (T_3,T_4) spectrum should follow the phase space distribution given by equation (10a). Conversely, equation (10a) may be used to detect the presence of any resonant process such as a two body final state interaction and/or a three-body resonance. For example, in the $^3H(p,2p)nn$ reaction, a resonance in the n-n system can be observed as an intensified 'locus' inside the four body continuum. However, an n-p resonance cannot be observed since these events are dispersed in the allowed continuum. The presence of a three-body resonance (p-n-n) will show up as an enhancement parallel to one or both of the energy axes in the continuum. This corresponds to the detection of an inelastically scattered proton in one detector and a proton emitted sequentially from the excited three nucleon system in the other detector. No similar effect can be observed if the three-body resonance occurs between particles (p-p-n) where two of the resonant particles (protons) are detected simultaneously; these events do not lie on a curve in the T_3-T_4 plane. Results of the comparison between data and phase space predictions will be shown in section 6.3.

2.2 The Plane Wave Impulse Approximation (PWIA)

The three-body system has been solved exactly by Faddeev (Fa60) in terms of a set of coupled integral equations which contain all the two-body T-matrices as parameters. Although the Faddeev formalism has been generalized to the four-body system, no practical method exists at present for solving the equations involved. For this reason, it is still not possible from a practical point of view to treat a four-body reaction such as ^{3}He(p,2p)pn exactly. However, if we consider only ^{3}He(p,2p)d* events where d* refers to the unobserved p-n pair with near zero relative energy, the reaction can be approximated by a three-body reaction in which the d* is treated as a composite particle, described by a two-body scattering wave function.

In what follows, we shall discuss the approximations involved in the PWIA as applied to a three-body reaction 2(1,34)5 shown pictorially in Fig.2.2.1. Particles 4' and 5' respectively refer to particles 4 and 5 as they exist inside the nucleus (particle 2) before the collision. The transition matrix elements for this reaction is given by

$$T_{fi} = \langle \psi_3 \psi_4 \psi_5 | T_{3b} | \psi_1 \psi_2 \rangle \qquad (11)$$

where T_{3b} is the full three-body transition operator. The PWIA assumes the following:

1. All the unbound particles are described by plane waves so that the final state wave function can be described by $|\vec{k}_3, \vec{k}_4, \vec{k}_5\rangle$ where $\langle \vec{r} | \vec{k} \rangle = \left(\frac{1}{2\pi}\right)^{3/2} \exp(i\vec{k}\cdot\vec{r})$.
2. The incident particle interacts only with particle 4' in the nucleus and that the residual nucleus 5 is a spectator to the reaction. This means that T_{3b} is to be replaced by T_{2b}, the T-operator for the interaction of particle 1 and particle 4'. Furthermore, since particle 5 is the spectator, $\vec{k}_5 = \vec{k}_{5'}$, i.e. the spectator retains the momentum

(a)

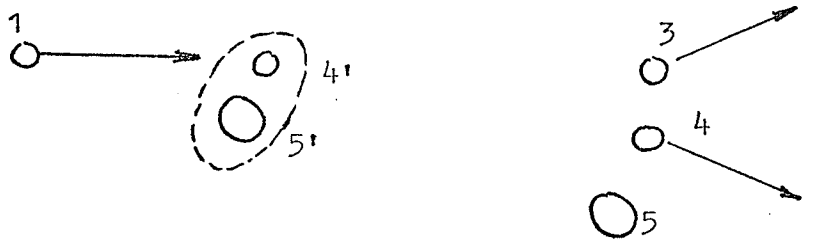

Initial state Final state

(b)

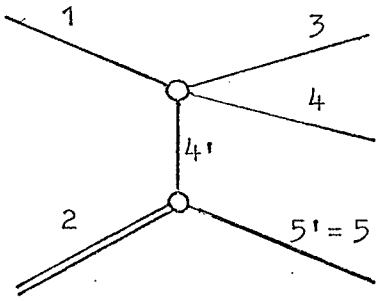

Fig.2.2.1: Pictorial representation (a) and pole diagram (b) for quasi-free scattering.

it had inside the nucleus. With this approximation the transition matrix element can now be written as

$$\begin{aligned} T_{fi} &= \langle \vec{k}_3, \vec{k}_4, \vec{k}_5 \mid T_{2b} | \vec{k}_1, \psi_2 \rangle \\ &= \int d^3\vec{k}_4' \langle \vec{k}_3, \vec{k}_4, \vec{k}_5 | T_{2b} | \vec{k}_1 \rangle | k_4' \rangle \langle k_4' | \psi_2 \rangle \\ &= \int d^3\vec{k}_4' \langle \vec{k}_3, \vec{k}_4 | T_{2b} | \vec{k}_1, \vec{k}_4' \rangle \langle \vec{k}_4', \vec{k}_5 | \psi_2 \rangle \\ &= \int d^3\vec{k}_4' \langle \vec{k}_3, \vec{k}_4 | T_{2b} | \vec{k}_1, \vec{k}_4' \rangle \Phi(\vec{k}_{rel}) \delta(k_4' + k_5') \quad . \end{aligned} \tag{12}$$

In the cluster model, ψ_2 is taken to be the relative motion wave function of the clusters while $\Phi(\vec{k}_{rel})$ represents the Fourier transform of ψ_2. $\vec{k}_{rel}$ is the relative momentum of the clusters in the target. The δ-function arises from momentum conservation within the nucleus viz. $\vec{k}_4' = -\vec{k}_5'$. Integrating out the δ-function yields

$$T_{fi} = \langle \vec{k}_3, \vec{k}_4 | T_{2b} | \vec{k}_1, -\vec{k}_5 \rangle \Phi(-\vec{k}_5) \tag{13}$$

where $\vec{k}_5' = \vec{k}_5$ has been used. In the tri-nucleon system where no definite clusters exist, it is more realistic to take ψ_2 as the overlap between the spatial wave function of the target and the residual nucleus. In both cases, $\Phi(-\vec{k}_5)$ represents the momentum distribution of the struck particle (equivalently the recoil particle because of momentum conservation) inside the nucleus. $\langle \vec{k}_3, \vec{k}_4 | T_{2b} | \vec{k}_1, -\vec{k}_5 \rangle$ is just the matrix element for the two-body system describing the transition from the initial state $(\vec{k}_1, -\vec{k}_5)$ to the final state $(\vec{k}_3, \vec{k}_4)$.

The differential cross section for the reaction 2(1,34)5 with particles 3,4 and 5 in the momentum range $d^3\vec{k}_3$, $d^3\vec{k}_4$, $d^3\vec{k}_5$ is

$$d\sigma = \frac{(2\pi)^4}{|\vec{v}_{rel}|} d^3\vec{k}_3 \, d^3\vec{k}_4 \, d^3\vec{k}_5 \, |T_{fi}|^2 \, \delta(Q_i - Q_f) \tag{14}$$

where Q_i and Q_f are the four-momenta of the system in the

initial and final state respectively, and $\vec{v}_{rel}$ is the relative velocity between the incident particle and the target.

Explicit integration over $d^3\vec{k}_5$ (the momentum variable of the unobserved particle) has been obtained by Jain (Ja69). The result is

$$\frac{d^3\sigma}{d\Omega_3\, d\Omega_4\, dT_3} = KF \left(\frac{d\sigma}{d\Omega}\right)^{3-4}_{c.m.} N_F \left|\Phi(-\vec{k}_5)\right|^2 \qquad (15)$$

where KF, the kinematic factor containing the non-invariant phase space distribution factor, is given by

$$KF = \frac{k_3 k_4^2 E_5 E_{34}^2}{k_1 E_4 \left[k_4 E_5 + E_4 (k_4 - k_1 \cos\theta_4 + k_3 \cos(\theta_3 + \theta_4)\right]} \qquad (16)$$

and $\left(\frac{d\sigma}{d\Omega}\right)^{3-4}_{c.m.}$ is the free two-body scattering cross section on-the-energy-shell for particles 3 and 4 . It represents an approximation to the square of the off-the-energy-shell scattering amplitude given previously as $\langle \vec{k}_3, \vec{k}_4 | T_{2b} | \vec{k}_1, -\vec{k}_5 \rangle$. The scattering is off-the-energy-shell since particle 4 is not free in the nucleus but is bound by an amount determined by the Q-value of the reaction. The normal relationship among the components of its four-momentum no longer holds, i.e. $q^2 \neq E^2 - m^2$. N_F is a factor due to spin and antisymmetrization.

In terms of the pole diagram for quasi-free scattering (Fig. 2.2.1 (b)) , the lower vertex yields a form factor characterizing the momentum distribution of the struck particle in the nucleus while the upper vertex yields the off-the-energy-shell scattering amplitude for the incident and struck particle. A more complete discussion of the use of vertices in pole diagrams can be found in reference (Sh66).

It is evident from equation (15) that a measurement of the cross section can yield information on the momentum distribution of the constituent particles in a nucleus provided one can evaluate the off-the-energy-shell two-body scattering amplitude. The use of $\left(\frac{d\sigma}{d\Omega}\right)^{3-4}_{c.m.}$ ignores the off-the-energy-shell effects . Moreover, there exists an ambiguity in the c.m. energy E_{34} which is to be used in obtaining $(d\sigma/d\Omega)^{3-4}_{c.m.}$. Several prescriptions have been taken:

1. The final state energy prescription in which the cross section is evaluated on-the-energy-shell at the centre of mass energy of the final state of the two detected particles.
2. The initial state energy prescription in which the cross section is again evaluated on-the-energy shell at the centre of mass energy of the initial state of the two interacting particles, i.e. the incident particle and the struck particle. The momentum of the struck particle before the collision is assumed to be equal to the recoil momentum of the spectator.
3. The third approximation is that due to Stern and Chamberlain (Ch54) and has been used by Frascaria et al (Fr71). In this approximation, the off-the-energy-shell cross section is evaluated at a centre of mass energy E'' of the two interacting particles where corresponding to this centre-of-mass energy are the relative momentum $\vec{p}''_{rel}$ and scattering angle θ'' which satisfy

$$\left.\begin{aligned} |\vec{p}_{rel} + \vec{p}'_{rel}|^2 &= 2p''^2_{rel}\,(1 + \cos\theta'') \\ |\vec{p}_{rel} - \vec{p}'_{rel}|^2 &= 2p''^2_{rel}\,(1 - \cos\theta'') \quad . \end{aligned}\right\} \qquad (17)$$

$\vec{p}_{rel}$ and $\vec{p'}_{rel}$ are respectively the relative momentum of the interacting particles in their centre of mass system before and after the collision.

4. The half-off-the-energy-shell T-matrix approximation. For p-p scattering in S-states only, the off-the-energy-shell T-matrix can be expressed in terms of a separable two-nucleon interaction (Ya54)

$$t(p^2,p'^2,k^2+i\epsilon) = g(p^2)g(p'^2)\tau(k) \qquad (18)$$

where p and p' are respectively the c.m. momentum before and after the collision. Explicitly, in terms of the Yamaguchi form factors,

$$t(p^2,p'^2,k^2+i\epsilon) = \frac{1}{(p^2+\beta^2)} \cdot \frac{1}{(p'^2+\beta^2)} \cdot \frac{\lambda(k+i\beta)^2}{(k-i\alpha)(k-i\gamma)} \qquad (19)$$

The term half-off-the-energy-shell refers to the prescription in which k is set equal to p'. A modification to equation (19) can be made to fit the on-the-energy-shell data in the laboratory energy range 20-80 MeV. Following Wallace (Wa73), the modification takes the form

$$t(p^2,p'^2,k^2+i\epsilon) = g(p^2)g(p'^2)\tau(k)\frac{\rho(k)}{1+ikg^2(k^2)\tau(k)[1-\rho(k)]} \qquad (20)$$

where
$$\rho(k) = 1 + \left(\frac{k^2+\alpha^2}{U_o^2+\alpha^2}\right)\Delta\left(1+e^{-uk^2}\right)^{-1} \qquad (21)$$

Figure 2.2.1 shows the fit to the p-p and n-p data obtained by Wallace. The parameters which we have used (Bo73) and which reproduce the fit up to 80 MeV are $\alpha = -0.1112$ fm^{-1}, $\beta = 1.2$ fm^{-1}, $\gamma = -2\beta-\alpha$, $\lambda = 2\beta(\alpha+\beta)^2$, $U_o = 25/\hbar^2$ fm^{-2}, $u = \hbar^2/3$ fm^2 and $\Delta_{pp} = 0.480$.

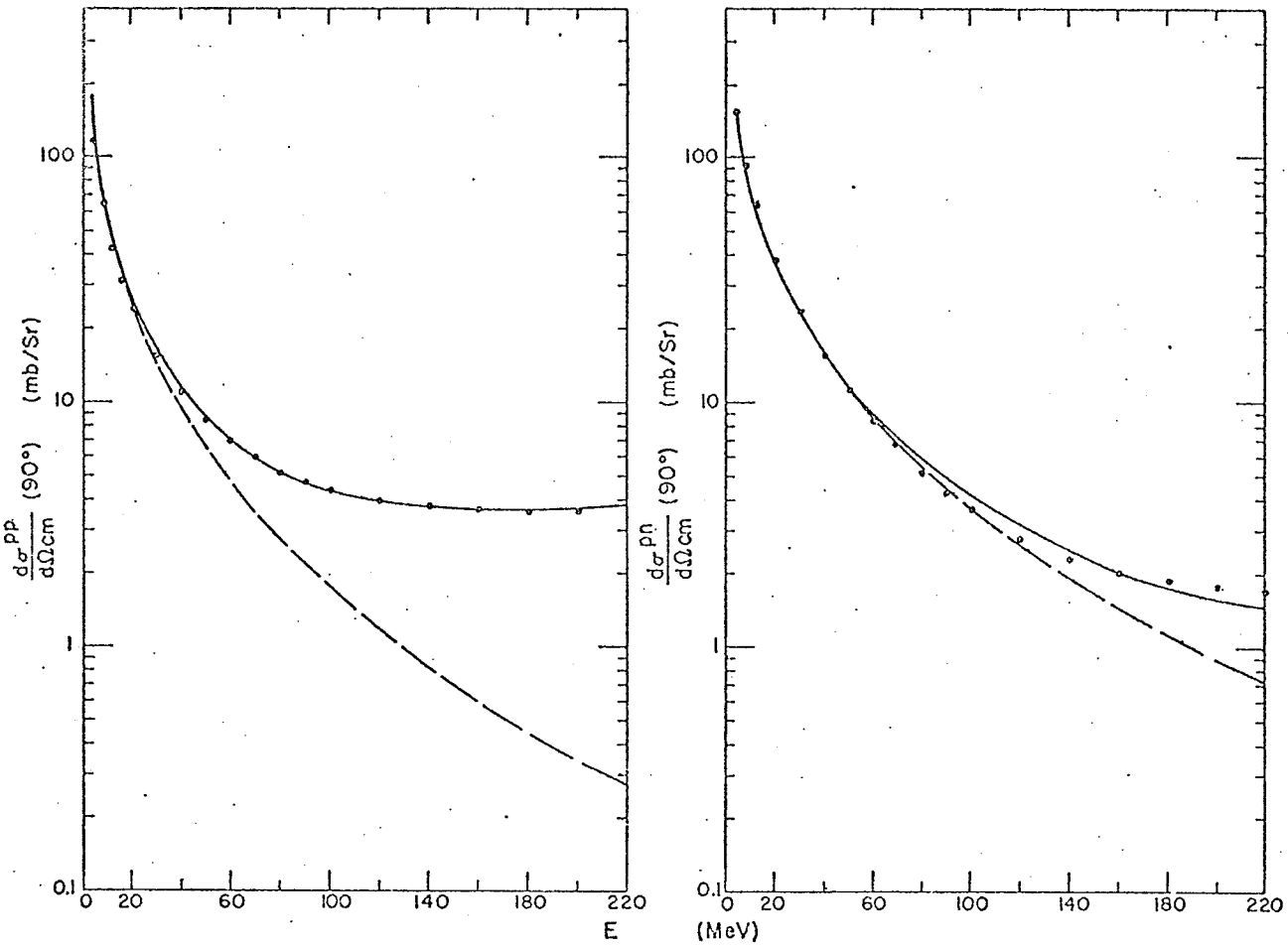

Fig.2.2.2: Fits to the p-p and n-p elastic scattering data from a modified separable potential (solid curves) (Wa73). The dashed curves indicate the predictions of the S-wave Yamaguchi amplitudes.

Redish et al.(Re70) have shown that the off-shell cross sections can differ appreciably from the above on-shell approximations. For the ^{3}H(p,2p)[nn] reaction, all four approximations have been used while for the ^{3}H(p,pd)n reaction, only the final state energy prescription was used. The results are presented in section 6.1.1.

In the evaluation of the Fourier transform of the overlap integral, different wave functions for the target and recoil particle have been used and these are summarized in Table 2.1. The coordinate system used for the trion wave function is given in Fig.2.2.3.

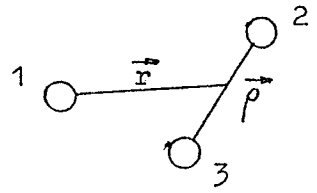

Fig.2.2.3: Coordinate system for the tri-nucleon.

The vectors $\vec{\rho}$ and $\vec{r}$ are related to $\vec{r}_{12}$, $\vec{r}_{13}$, $\vec{r}_{23}$ through the equations $\vec{r}_{23} = \vec{\rho}$, $\vec{r}_{12} = \vec{r} - \vec{\rho}/2$, $\vec{r}_{13} = \vec{r} + \vec{\rho}/2$ so that $\vec{r} = \frac{1}{2}(\vec{r}_{12} + \vec{r}_{13})$.
For the Irving wave function, the value of α is that found by Schiff (Sc64) in his analysis of the elastic e-^{3}He and e-^{3}H experiments. In the case of the Irving-Gunn wave function for ^{3}He, α is that obtained in the analysis of the photodisintegration of ^{3}He which was also found to fit the charge form factor and the Coulomb energy of ^{3}He (Be64). α occuring in the Irving-Gunn wave function for ^{3}H is obtained from variational calculation on the binding energy of the ^{3}H system (Gu51). Details of the evaluation of the Fourier transform of the overlap integral are given in Appendix II.

Nucleus/ Virtual state	Type	Form of the coordinate space wave function	Values of parameter	Ref.
^{3}He	Irving	$A \exp\left\{-\frac{1}{2}\alpha(r_{12}^2+r_{23}^2+r_{13}^2)^{\frac{1}{2}}\right\}$	$A=3^{\frac{3}{4}}\alpha^3/(120)^{\frac{1}{2}}\pi^{\frac{3}{2}}$ $\alpha=1.265$ fm^{-1}	(Gu51)
^{3}He	Irving-Gunn	$\dfrac{A \exp\left\{-\frac{1}{2}\alpha(r_{12}^2+r_{23}^2+r_{13}^2)^{\frac{1}{2}}\right\}}{(r_{12}^2+r_{13}^2+r_{23}^2)^{\frac{1}{2}}}$	$A=3^{\frac{1}{4}}\alpha^2/\sqrt{2}\,\pi^{3/2}$ $\alpha=0.77$ fm^{-1}	(Gu51) (Be64)
^{3}H	Irving-Gunn	"	$A=3^{\frac{1}{4}}\alpha^2/\sqrt{2}\,\pi^{3/2}$ $\alpha=1.00$ fm^{-1}	(Gu51)
d	Hulthén	$\dfrac{[2ab(a+b)]^{\frac{1}{2}}}{\sqrt{4\pi}(b-a)}\dfrac{e^{-a\rho}-e^{-b\rho}}{\rho}$	$a=0.232$ fm^{-1} $b=1.440$ fm^{-1}	(Hu57)
d*	Hulthén-Sugawara	$a_{np}(1-\dfrac{\rho}{a_{np}}-e^{-\xi\rho})/\rho$	$\xi=1.14$ fm^{-1} $a_{np}=-23.7$ fm	(Hu57, Ar71, Ja74)
[nn]	"	$a_{nn}(1-\dfrac{\rho}{a_{nn}}-e^{-\xi\rho})/\rho$	$\xi=1.19$ fm^{-1} $a_{nn}=-16.4$ fm	(Hu57)

Table 2.1 Spatial wave functions for ^{3}He, ^{3}H, d, d*, and [nn].

2.3 Watson-Migdal theory of final-state interaction

The diffential cross section for a reaction of the type $1 + 2 \longrightarrow 3 + 4 + 5 + - - - n$ may be written as

$$\sigma = \frac{2\pi\mu_i}{\hbar\hbar k_i} \rho \sum_{\text{spin}} |T_{fi}|^2$$

where μ_i and k_i are the reduced mass and the wave number of the relative motion in the initial state and ρ is the non-relativistic phase space factor. T_{fi} is the transition matrix element and $\sum_{\text{spin}}$ represents an average over the initial spin states and a sum over the final spin states. Watson (Wa52) and independently Migdal (Mi55) derived expressions to account for the peaking due to a final state interaction. The conditions for applicability of the W-M model may be summarised as follows:

1. The primary reaction mechanism is characterized by a short-range interaction (i.e. confined to a certain volume of order b^3) irrespective of what happens to the particles produced in the reaction.
2. The effect of the final state interaction must be considered only for low relative energy of the interacting particles.
3. The final state interaction must be strong and attractive.

With these conditions satisfied, the transition amplitude $|T_{fi}|^2$ may be factorized into two terms, one due to the primary reaction and the other due to an enhancement from the two body final state interaction.

Further, if only S-waves are considered and the effective range approximation applied (in case of nucleon-nucleon final state

interaction), $|T_{fi}|^2$ may be written as (Gi64)

$$|T_{fi}|^2 = \frac{\left[r_o^{-1} - a^{-1} + r_o k^2/2 + r_o^{-1}(1-2r_o a^{-1})^{1/2}\right]^2}{k^2 + (r_o k^2/2 - a^{-1})^2} |T_{fi}^{(o)}|^2 \qquad (22)$$

where a is the scattering length, r_o is the effective range and k is the relative momentum of the interacting pair. $T_{fi}^{(o)}$, the production amplitude, represents the primary reaction. It should be noted that the above expression is applicable only for a FSI between a n-p or n-n pair. The p-p interaction requires additional terms to account for Coulomb effects.

To include the possible contribution of the $^3S_1$ n-p FSI, the following expression was used,

$$d\sigma \sim \rho(\vec{P},E)\ (F_s + W_t F_t)\ |T_{fi}^{(o)}|^2 \qquad (23)$$

where F_s and F_t have the form of the first term in equation (22) with appropriate singlet and triplet scattering parameters. W_t is a real number weighting factor. Equation (23) has been used to give predictions for the shape of the missing mass spectra of the ^{3}H(p,2p)nn and the ^{3}He(p,2p)pn reactions and also for the projected energy spectrum of the ^{3}H(p,pd)n reaction. In all cases, $|T_{fi}^{(o)}|^2$ is assumed to be a constant. For the missing mass predictions, the invariant phase space $R_4(\vec{P},E)$ as given by equation (10) in chapter 2 is used in place of the non-invariant phase space $\rho_4(\vec{P},E)$. Results of these comparisons are shown in section 6.2.

3. THE EXPERIMENT

3.1 Kinematical regions studied

A list of the reactions studied has been given in section 1.4. Since the masses of ^3H and ^3He are almost the same, the kinematics for the charge symmetric reactions are almost identical. Fig.3.1.1 shows the kinematic loci for the various reactions which can be considered two-body processes. Each square in the diagram represents one particular angle pair. In the first of the two runs of this experiment, the following coplanar angle pairs were studied: $\theta_3 = \theta_4 = 30^\circ$, 35°, 37.5°, 40°, 42.5°, 50° and 60°, $\phi_{34} = 180^\circ$ for all cases. In this run, only (p,2p) data were obtained. In the second run, both symmetric and asymmetric coplanar angle pairs were studied. The former include $\theta_3 = \theta_4 = 25^\circ$, 30°, 38°, 47.5°, and 55°. The asymmetric angle pairs include $\theta_3 = 26^\circ$, $\theta_4 = 48^\circ$; $\theta_3 = 30^\circ$, $\theta_4 = 45^\circ$; $\theta_3 = 34^\circ$, $\theta_4 = 41.5^\circ$ and $\theta_3 = 41.6^\circ$, $\theta_4 = 60^\circ$, $\phi_{34} = 180^\circ$ in all cases. The first three angle pairs correspond to p-p quasi-free scattering while the last one corresponds to p-d quasi-free scattering. In addition to detecting (p,2p) events, provisions were made in the second run to detect (p,pd) and (p,dp) coincidence events simultaneously. The $^3He(p,2p)$ data were obtained in the second run.

It is evident from Fig.3.1.1 that much of the phase space studied pertains to p-p QFS, p-d QFS and n-p FSI. Angle pairs with θ_3 or θ_4 less than 25° have not been studied because of the limitations imposed by the design of the scattering chamber and detector mount system. Angle pairs with θ_3 or θ_4 larger than 60° generally have such a low cross section that to obtain statistically meaningful

Fig.3.1.1: Kinematic loci for the various possible reactions resulting from the break-up of ^3H by 45.6 MeV protons. The squares correspond to the angle pairs studied in this experiment.

———	$^3H(p,2p)nn$	p-p QFS, n-n pair has zero relative energy and zero laboratory momentum.
— — —	$^3H(p,pd)n$	p-d QFS
——·—	$^3H(p,pd^*)n$	p-d* QFS, d* here represents an n-p pair with zero relative energy
—··—	$^3H(p,dp)n$	as $^3H(p,pd)n$ with θ_3 and θ_4 interchanged
—···—	$^3H(p,d^*p)n$	as $^3H(p,pd^*)n$ with θ_3 and θ_4 interchanged
— —·	$^3H(p,d^*d^*)$	d* here refers to an n-p pair with zero relative energy
— —··	$^3H(p,dd^*)$	
———	$^3H(p,dd)$	neutron pick-up reaction

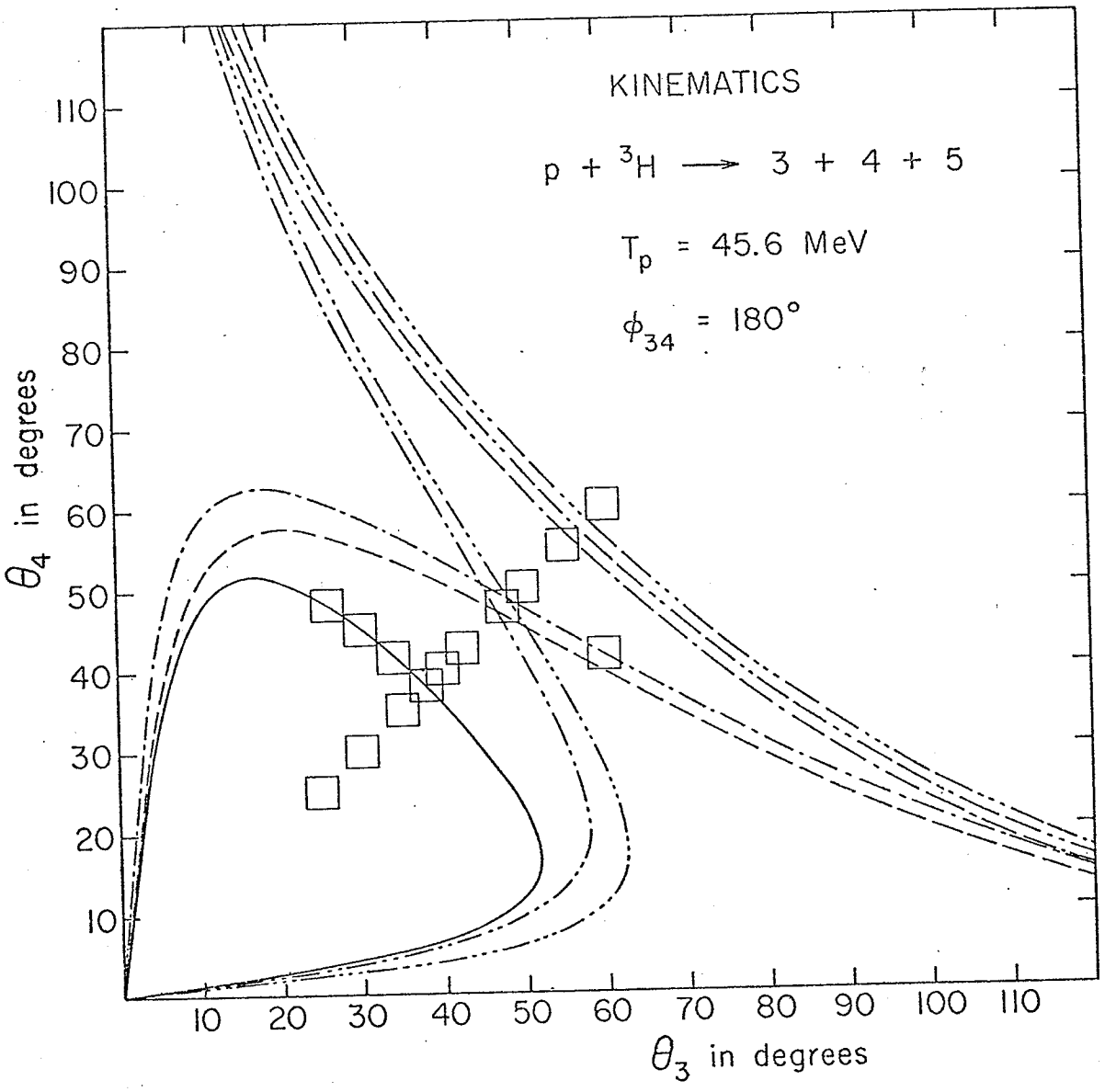

Fig.3.1.1: (see caption on opposite page)

data would require unusually long times for the typical beam currents of 20-40 nA which were available.

3.2 Experimental apparatus

3.2.1 Accelerator and experimental area

The Manitoba sector-focused cyclotron (Bu66) accelerates negative hydrogen ions resulting in external proton beams variable in energy from 20 to 49 MeV. The variable energy extraction system is copied from the one at the UCLA cyclotron (Pa66,Pa67). The negative ions are stripped of their two electrons at a chosen radius by a thin metal foil (e.g. 0.0005" thick aluminium foil). The radius of curvature of the resultant proton beam becomes opposite to that of the negative ion beam inside the magnetic field of the cyclotron. The protons pass through the cyclotron fringing field into the combination magnet which corrects the direction of the beam to allow for different trajectories of the different energy beams inside the cyclotron. The stripping foil is adjustable in both radius and azimuth so that beams of any energy can be made to pass along the fixed axis of the external beam analysing system.

Fig.3.2.1 shows the complete layout of the cyclotron and the various experimental areas. The present experiment was performed using the 28" scattering chamber in the 45° right beam line, a photograph of which is shown in Fig,3.2.2.

The external beam analysing system consists of the following units (see Fig.3.2.1): steering magnet #1 (SM1), quadrupole doublet (Q1,Q2), steering magnet #2 (SM2), first slit system (S_1), bending magnet (SW), second slit system (S_2) and quadroupole doublet (Q9,Q10). The beam emerging from the cyclotron is diverging in the horizontal

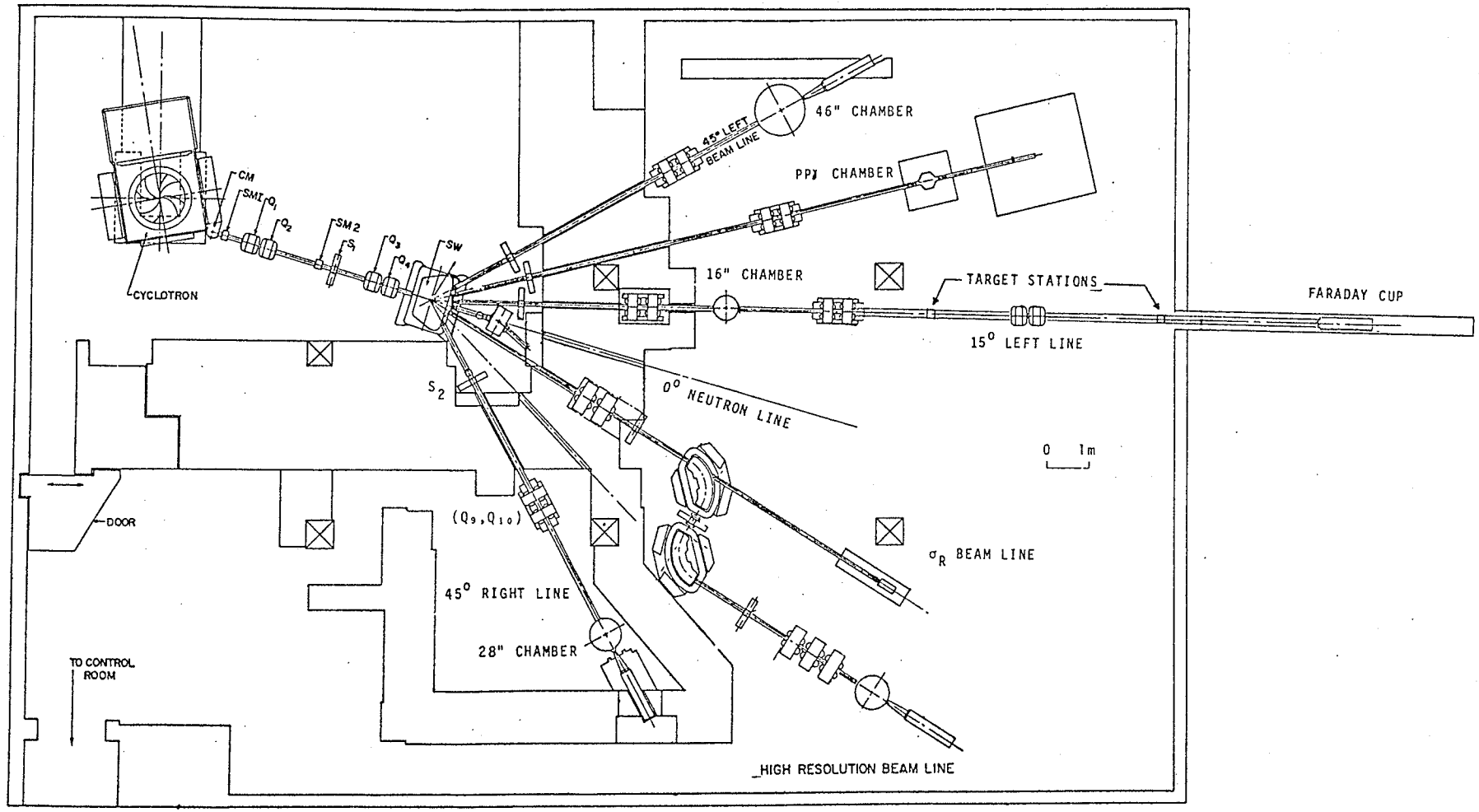

Fig. 3.2.1: Cyclotron layout showing external beam lines and the experimental areas.

Fig.3.2.2: A photograph of the 45° right experimental area showing the beam pipe with cold trap (foreground), the 28" scattering chamber with target lock and the Faraday cup (inside steel shielding).

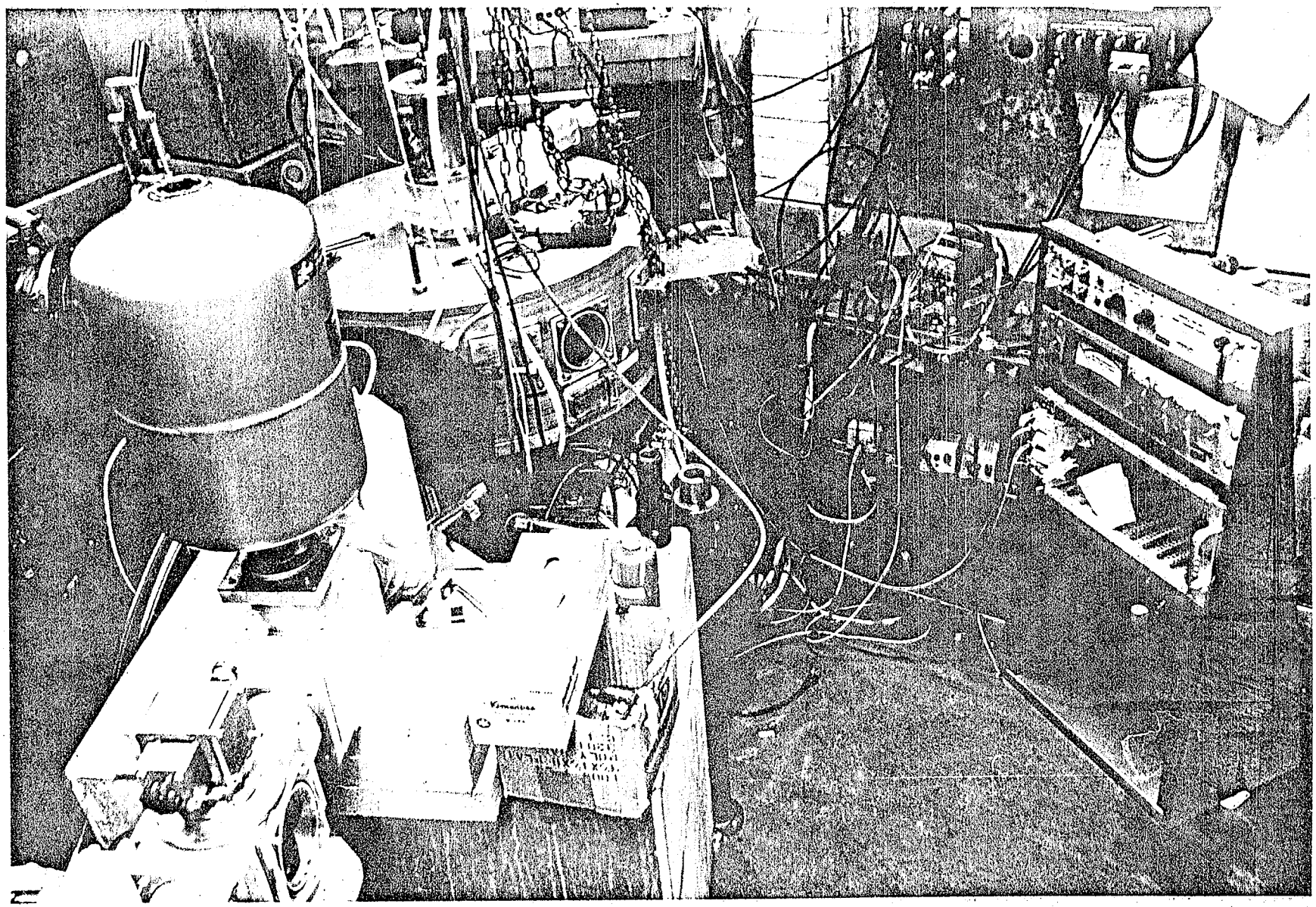

plane. A waist is produced at the position of the first slit system by (Q_1,Q_2). After the bending magnet, a focus occurs at the second slit system (S_2). The third quadrupole doublet (Q_9,Q_{10}) produces a waist at the scattering chamber centre with an approximately rectangular shape. The steering magnets are used only if proper beam tuning conditions cannot be found. The size and energy resolution of the beam spot obtained at the scattering chamber centre depends on the apertures of both sets of defining slits. The first set of slits was typically fixed to give an aperture 0.2" wide by 0.8" high for a beam intensity of about 20 nA on target. The second set of slits was set to have an aperture 0.15" wide by 0.60" high. With this configuration, the beam spot on a target at the scattering chamber centre was smaller than 1/8" wide by 1/4" high while the beam energy resolution was typically 200 keV at 45 MeV. In general, the slits were varied (remotely controlled) and made as narrow as possible while maintaining an usable beam current. The energy of the incident beam follows from a calibration of the bending magnet, obtained previously from cross-over measurements. The field of the magnet is determined by means of an NMR probe which is located between the magnet poles. The beam energy is related to the the NMR frequency by $\gamma_{NMR} = cp$ where p is the proton momentum in the magnet. The constant c is in principle energy independent and was determined experimentally by measuring the beam energy as function of the NMR frequency by the cross-over method (Ba64, Sm64).

The scattering chamber has a 28" inner diameter and contains two movable platforms (arms), both of which can be positioned to an accuracy of 0.02°. On the platforms may be mounted detector holders

(cubes). To ensure that the detector cubes on which the collimators are mounted be positioned with high degree of reproducibility, a dowel-pin system is used for the detector cubes and the platforms. Moreover, the detector cubes can be placed at different distances from the centre of the chamber in steps of 1.250". Typically, the detector cubes are positioned at 4" from the centre and could be brought to between 25° and 160° relative to the beam, although individually, either cube may be brought to a more forward angle (~15°). The whole scattering chamber was made electrically floating so as to prevent any ground loops from contributing to the noise pick-up of the solid state detectors.

The beam left the scattering chamber through an exit foil of 0.002" thick Kapton-H foil, passed through a 1/2" air gap before entering a 6 ft long Faraday cup which also had a 0.002" thick Kapton-H foil over its entrance. The Faraday cup was well shielded by steel bricks to minimize background. A repeller ring near the front of the cup was maintained at a potential of -1.5 kV with respect to ground to stop secondary electrons from leaving or entering the Faraday cup. The beam current was integrated by a commercial current integrator which had an accuracy of 0.1% for its digitized output. At 37.5° on both sides of the scattering chamber are mounted two monitors (NaI scintillation counters) which can be used to check the position of the beam on target. A poorly centred beam incident on a high Z target (e.g. thin nickel foil) will result in different number of counts in the proton elastic scattering peak in both monitors.

3.2.2 Targets

Ideally, gaseous targets should be used for both ^{3}He and ^{3}H but because of the radioactive property of tritium the handling of tritium gas requires a great deal of precautionary measures. These include installing sensitive monitors to detect any leakage and a fail-safe containment system in the event of a rupture of the gas cell containing the tritium gas. Since the laboratory was not adequately equipped for these measures, a 'solid' tritium target was used instead. In this target, the tritium gas, total activity quoted by the manufacturer (Oak Ridge Isotopes Sales Division, Oak Ridge, USA) as being 7.6 Curies, was absorbed in a 4 mg/cm^2 thick, 0.5" diameter titanium foil which in turn had a gold backing of 10 mg/cm^2 thickness and 0.6" diameter. The gold backing served to maintain the shape of the titanium foil during the absorption process which involved heating the titanium to a very high temperature. The presence of titanium and gold in the target necessitated the subtraction of events contributed by both materials. For this reason, two identical targets were made, one with tritium and one without. During data taking, each run with the tritium target was followed immediately by a run with the dummy target. Fig.3.2.3 shows a photograph of the tritium target mount assembly. The top cell contained the tritium target mounted in a stainless steel holder. This containment cell had a 0.001" thick Kapton-H foil window and was evacuated by a separate pumping system, thus preventing any released tritium from contaminating the main pumping system of the scattering chamber. The exhaust from the tritium pumping system was lead to the outside atmosphere

Fig.3.2.3: A photograph of the tritium target ladder showing the Ti-^{3}H target inside its containment cell (top), the plastic scintillator screen (second from top), the dummy target inside a duplicate cell (third from top) and the CD_2 target (bottom).

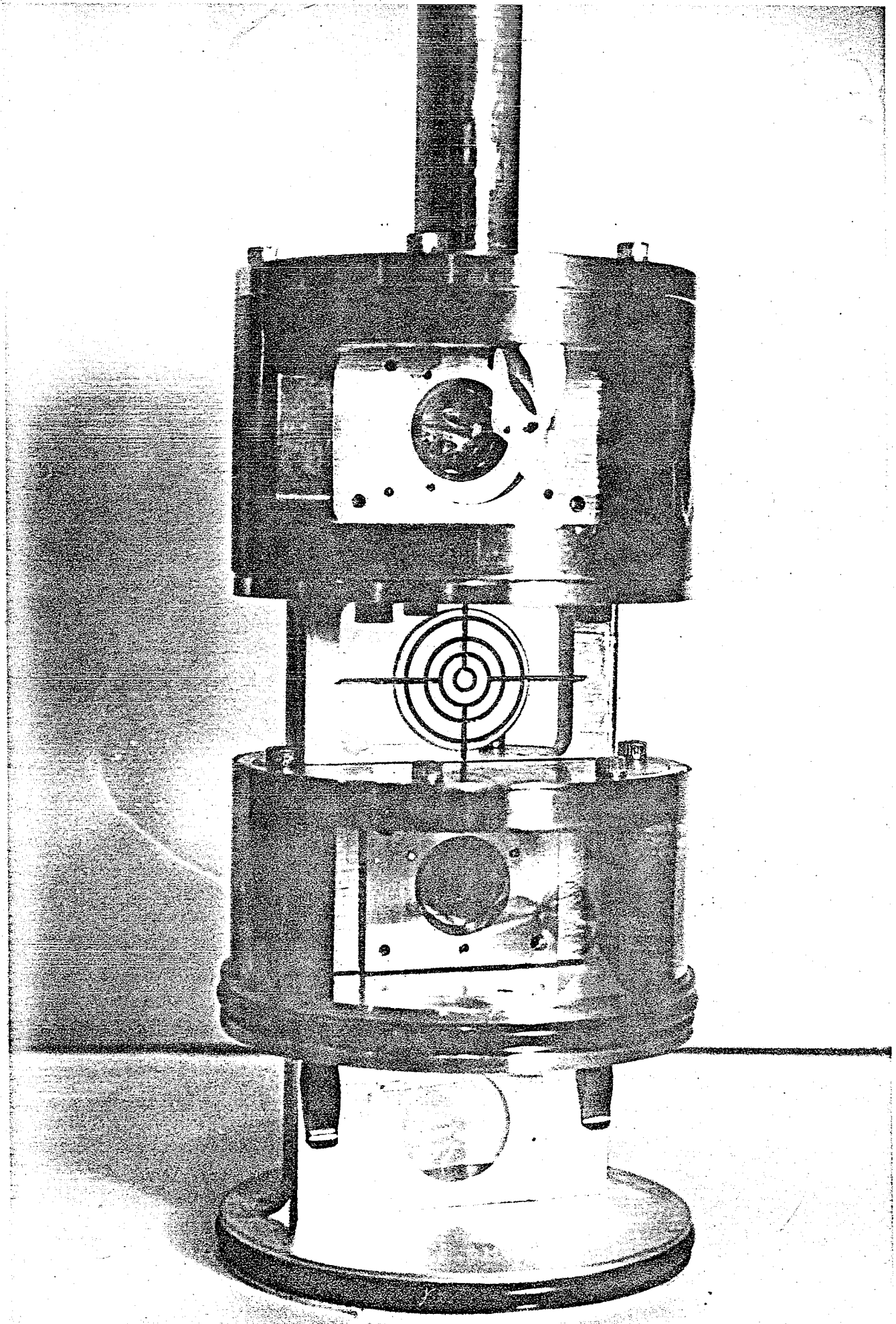

via closed pipes. In the event of a sudden venting of the scattering chamber, the foil also served to prevent the tritium target from being shattered by the implosion. The second target from the top was a screen made from plastic scintillator material and was used for checking the beam spot with the aid of a closed circuit television camera. This screen was essential for the adjustment of the beam optics before each run. The third target was the dummy target mounted in an identical holder and contained in an identical cell as the tritium target. The bottom target contained a CH_2 foil and a CD_2 foil mounted on top of one another. Each of the four targets could be brought to the centre of the scattering chamber by lifting or lowering the targer ladder. The O-ring seen at the bottom of the ladder served to align the ladder vertically as it entered the catcher cup mounted inside the chamber. Observation of the centre line of the plastic scintillator screen with a theodolite did not indicate lateral movement when the ladder was rotated as long as the bottom O-ring remained inside the catcher cup. If a change of target should become necessary, the whole target ladder could be lifted up and withdrawn completely into the target lock seated on top of the chamber (see Fig.3.2.2). With the gate valve closed, the whole target lock could then be removed from the chamber.

The major drawback of using a solid Ti-^{3}H target was that a dummy run had to be taken for every angle pair thus doubling the beam time required. Futhermore, the subtraction procedure reduced the statistical accuracy significantly in regions where the Ti contribution was the greatest. Fig.3.2.4 shows the kinematic loci for the

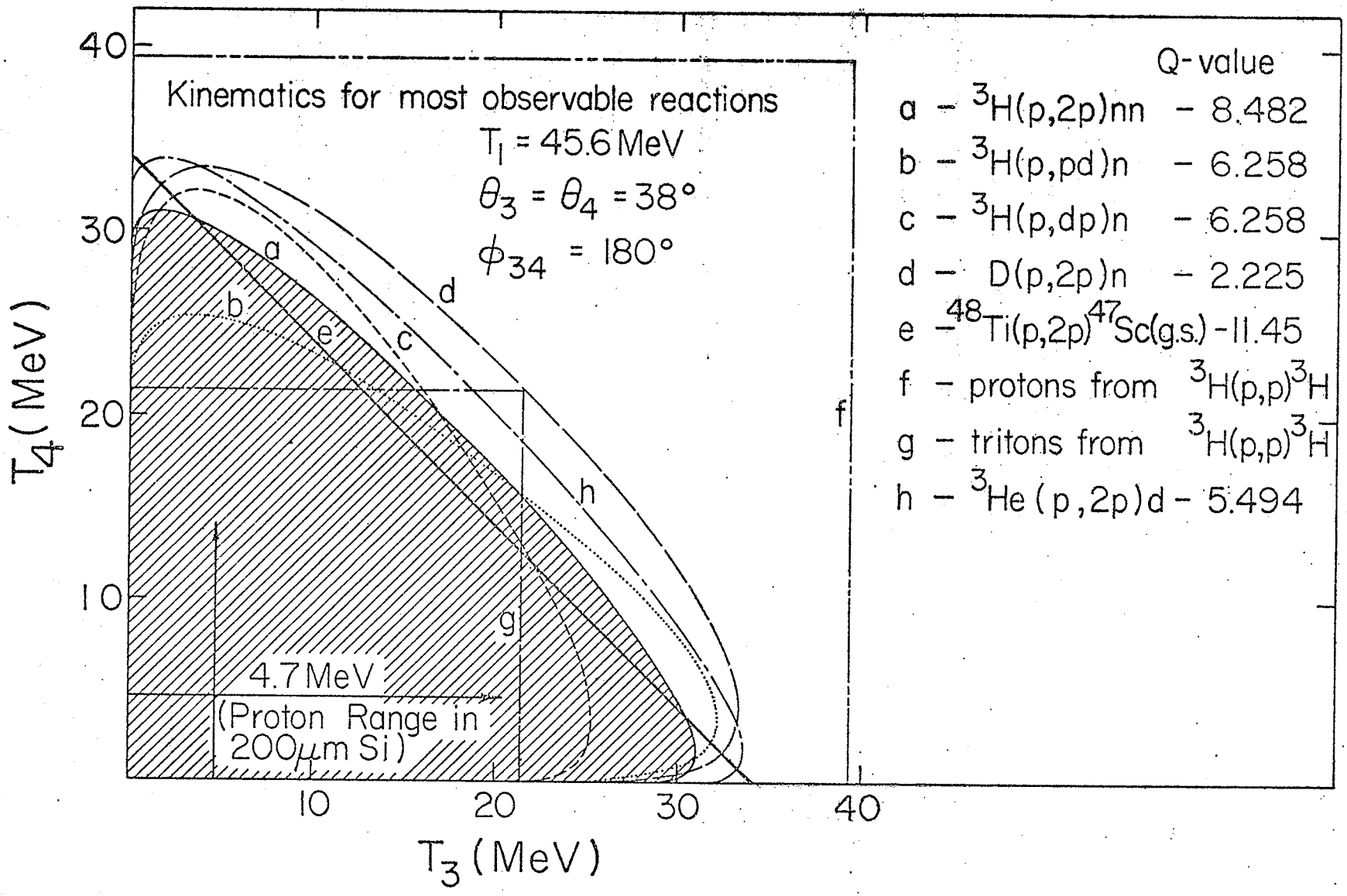

Fig. 3.2.4: Kinematic loci for the various reactions which occur when a 45.75 MeV proton beam bombards a Ti-^{3}H target.

various reactions which could be observed from the Ti-^{3}H target. The deuterium was present as a contaminant in the tritium used by the manufacturer. The ^{3}He contaminant originated from the decay of the tritium ($^3H \dashrightarrow {}^3He + \beta^- + \nu$, E_{β^-}= 18.6 keV, $t_{1/2}$ = 12.26 years). Fig.3.2.5. shows the missing mass spectra for the tritium target (a) and that for the dummy target of equal integrated charge. The left-most peak in (a) is due to the deuterium contaminant while the middle peak is due to the ^{3}He contaminant. It is evident from (b) that the (p,2p) events from the dummy target (Ti and Au) do not contribute significantly. In particular, Fig.3.2.6 shows that under the p-p QFS peak region, the contribution from the Ti and Au is negligible.

For the ^{3}He(p,2p) reaction, an isotopically pure (99.5%) gas target was used. The 2.45" diameter stainless steel gas cell had an outer appearance similar to that of the containment cell (Fig.3.2.3) but with a narrower gap (0.75") which was covered by 0.001" thick Kapton-H foil. The cell could be evacuated and filled through the hollow rod on top (see Fig.3.2.3). The pressure of the gas in the cell was monitored every hour during data taking using a Wallace and Tiernan precision pressure gauge. The gauge was calibrated from 0 to 30 p.s.i.a. in steps of 0.02 p.s.i.a. and had an accuracy of 0.2% of full scale. The gas pressure was set at slightly above one atmosphere at the beginning of the experiment and found to decrease by 1 p.s.i. in about 14 hours. The temperature in the cell was measured using a precision mercury in glass thermometer. Over the course of the experiment, the temperature was found to vary by less than 1°C.

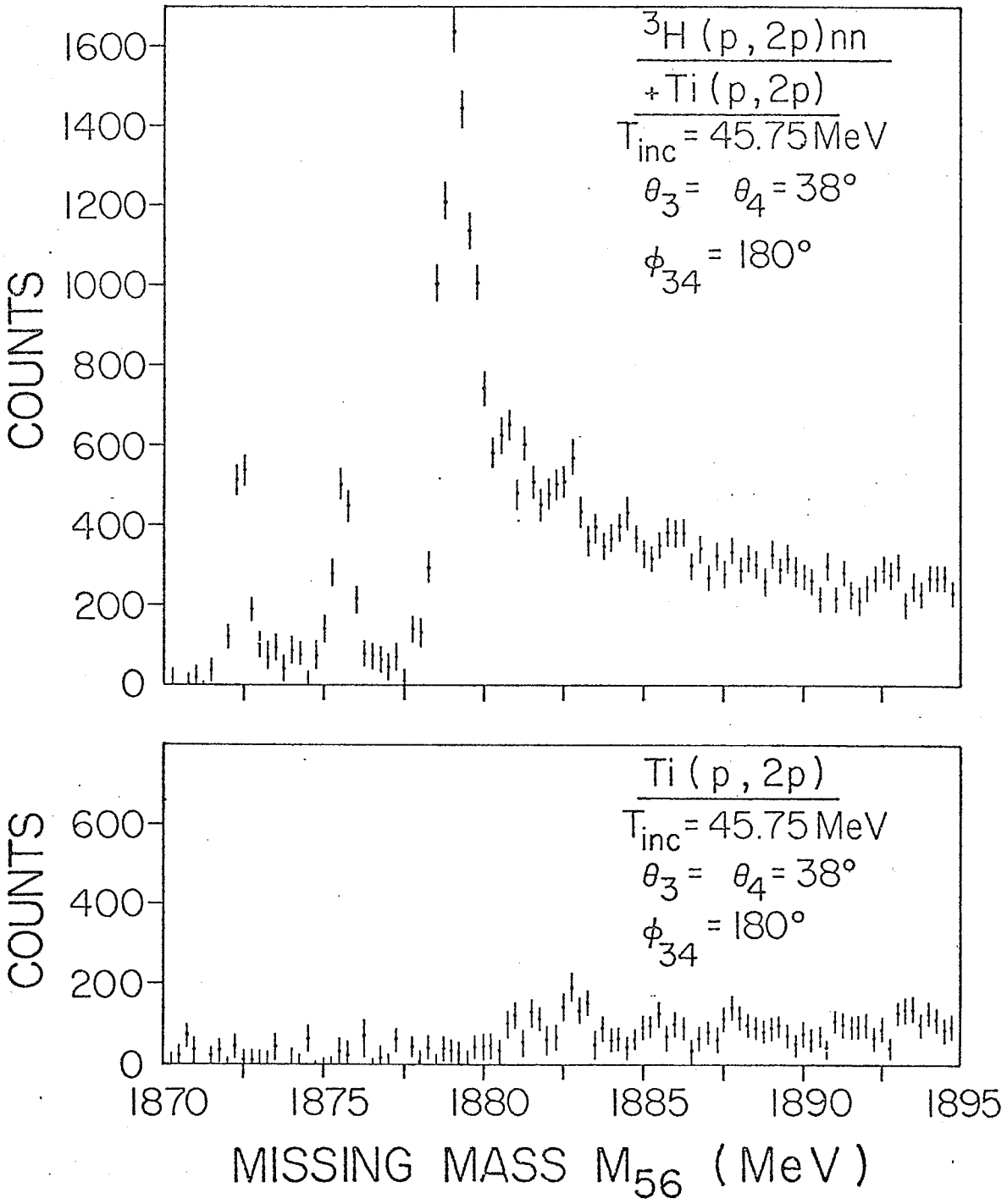

Fig.3.2.5: Missing mass spectra showing the relative contribution of the tritium target and the dummy target.

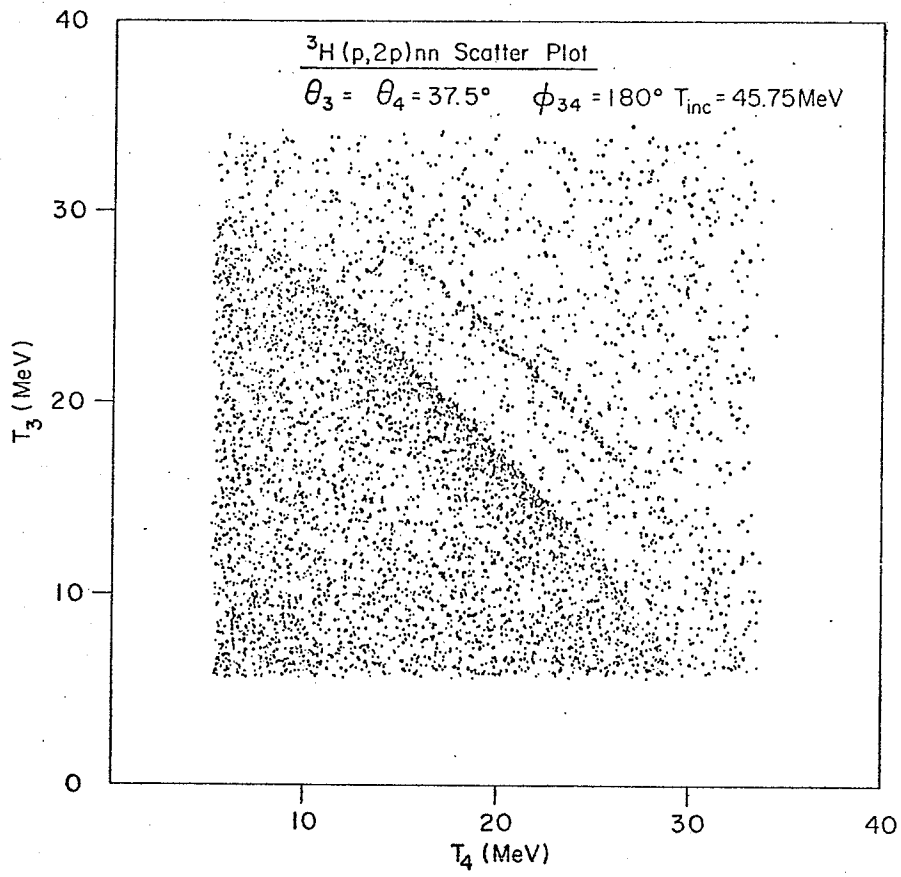

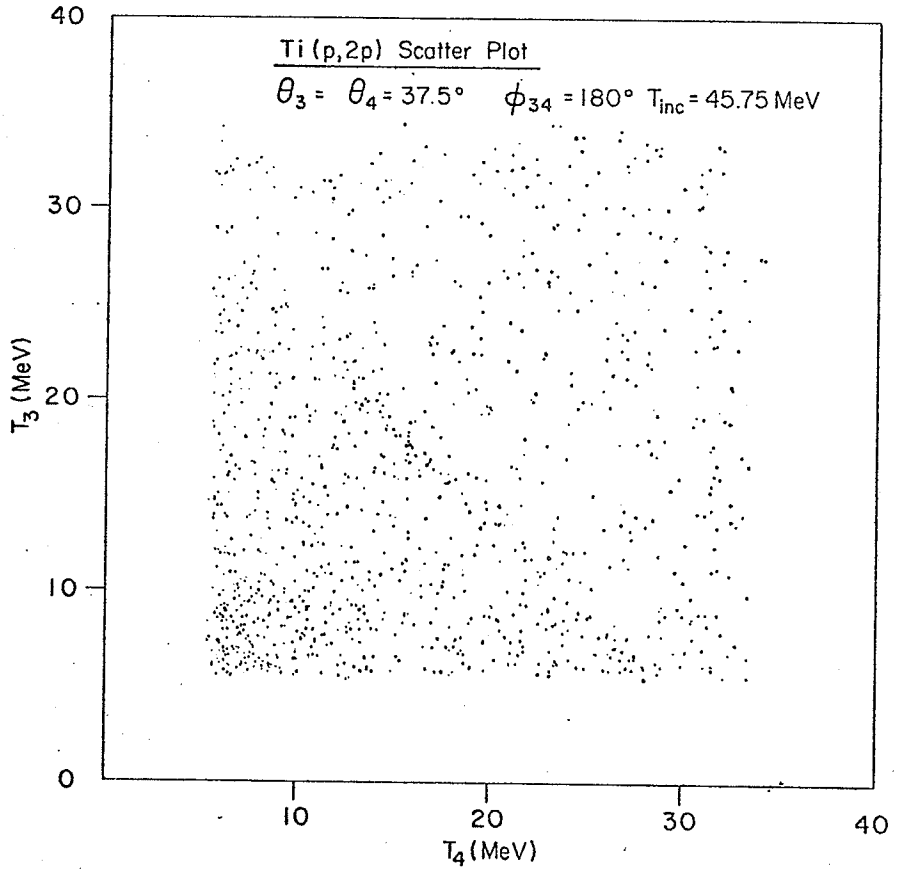

Fig.3.2.6: Scatter plots for the (p,2p) reaction on the Ti-^{3}H and the dummy targets.

3.2.3 Detectors and slit system

The detector and slit system used for both the first and second runs is shown in Fig.3.2.7. The detector system consisted of two identical particle telescopes, one on each side of the incident beam. Each particle telescope consisted of a ΔE ($\mathcal{E}$) detector (200μm thick, 200 mm^2 sensitive area surface barrier), a second ΔE detector (Δ) (1 mm thick, 200 mm^2 sensitive area surface barrier) and a E detector (5 mm thick, 200 mm^2 sensitive area lithium-drifted silicon detector). The V (veto) detector served only to reject the high energy elastically scattered protons. The detectors were mounted inside brass detector cubes by means of specially made perspex holders for electrical insulation. The electrical isolation again served to reduce noise pick-up arising from ground loops. The detector cubes were fixed on the platforms of the scattering chamber as described in section 3.2.1. The platforms were cooled by means of a freon refrigeration system which in turn cooled the detectors inside the detector cubes. It took typically 3 hours for the temperature to come to equilibrium ($\sim -20^{o}C$).

The $\mathcal{E}$ detector was chosen from a compromise between the highest energy protons that it would stop and the lowest energy of interest that would be deposited in it. A 200μm surface barrier detector stops 4.7 MeV protons and has an energy loss of $\sim$600 keV for 33 MeV protons passing through. The use of a 200μm $\mathcal{E}$ detector resulted in excellent proton and deuteron separation as can be seen in Fig.3.2.8. The use of a second ΔE (Δ) detector served two purposes. Firstly, it provided the additional thickness required to stop 33

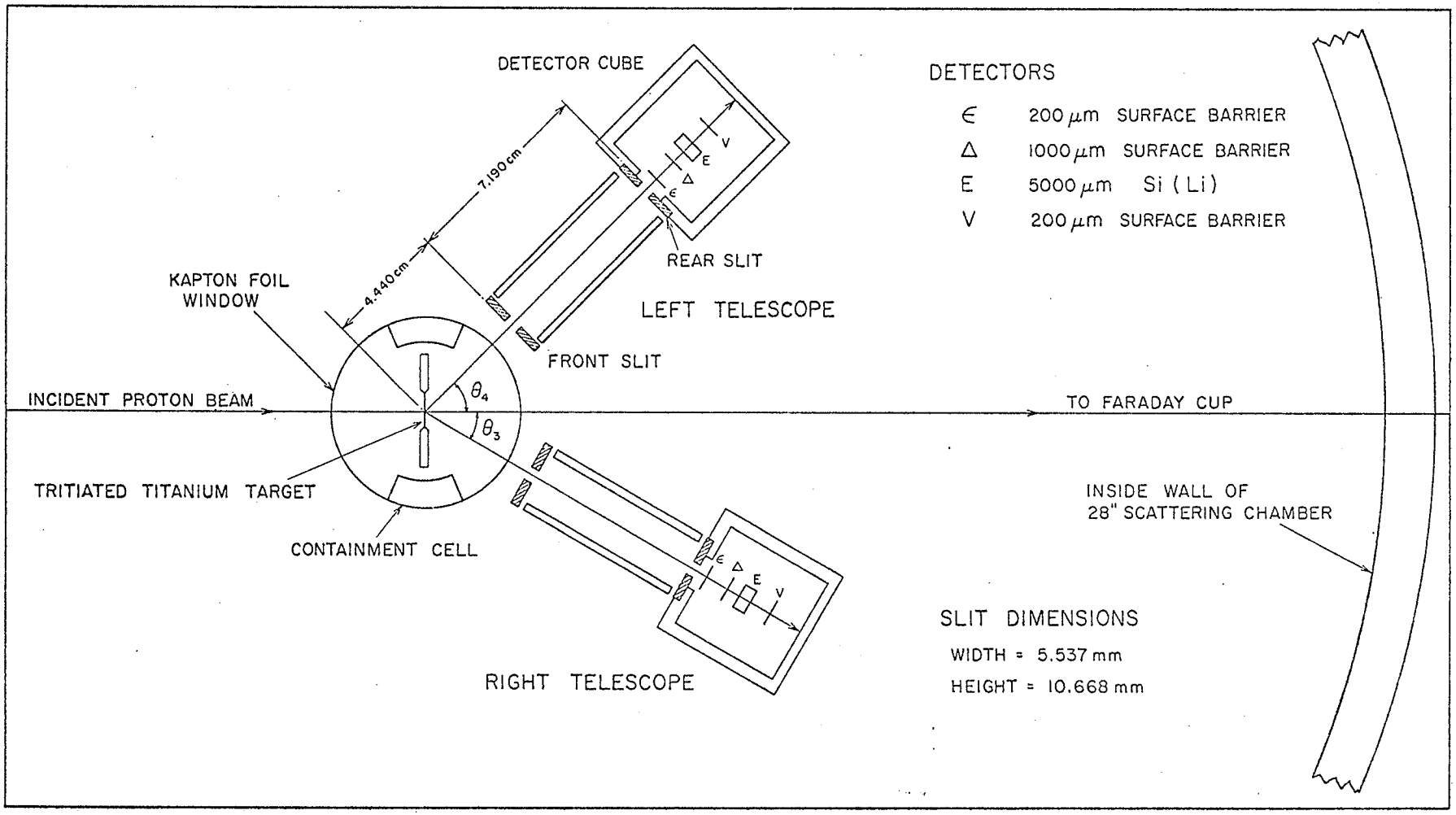

Fig. 3.2.7: A scale drawing of the inside of the 28" scattering chamber showing the tritium target, the containment cell, the detector telescopes and the slit system. Thicknesses of the detectors and slit dimensions are also indicated.

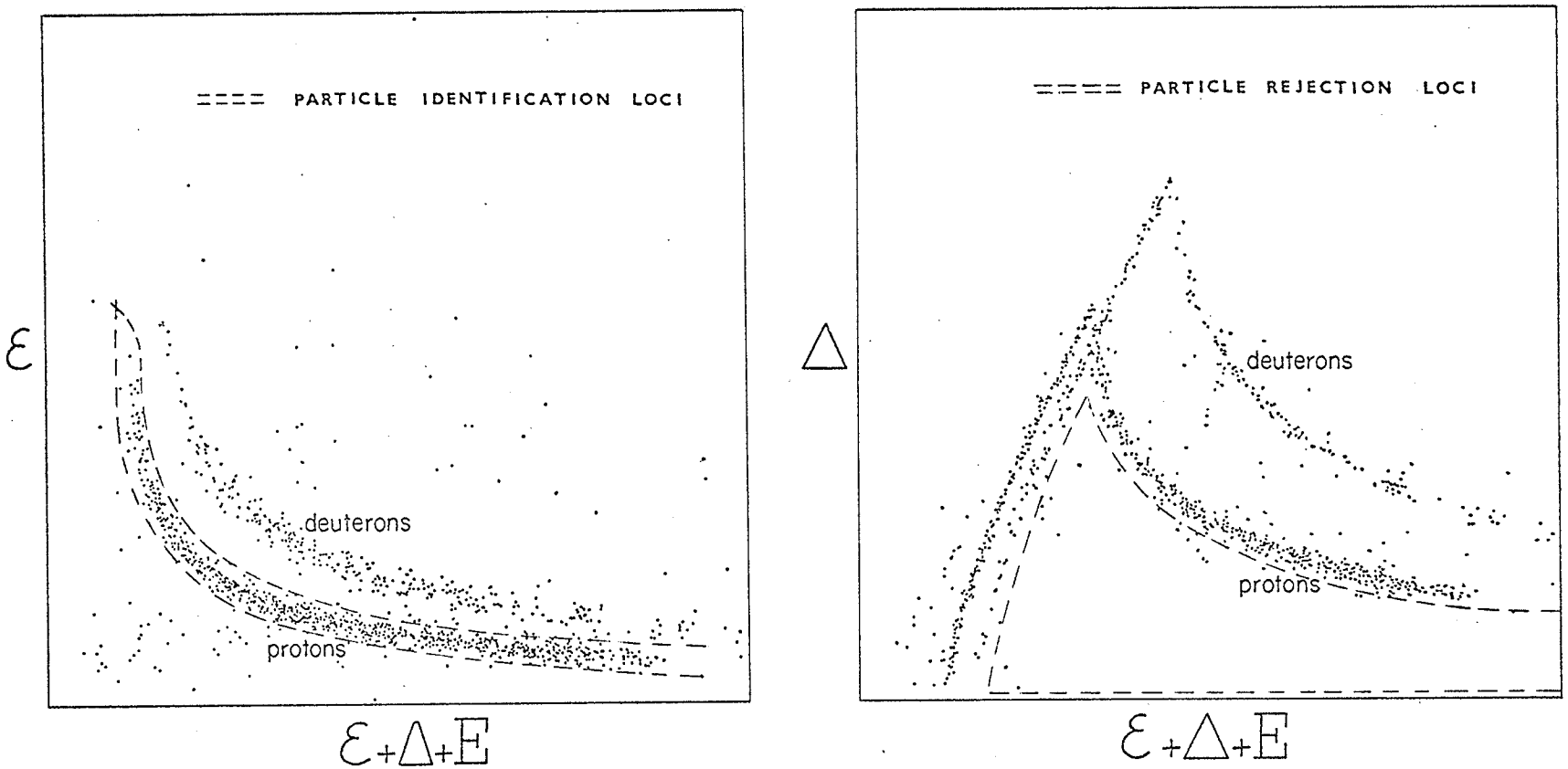

Fig. 3.2.8: Particle separation from a detector telescope consisting of a 200μm ε surface barrier detector, a 1 mm surface barrier Δ detector and a 5 mm Si(Li) E detector. The lines on the left of the Δ versus (ε+Δ+E) display are caused by the particles stopping in the Δ detector. No such lines are observed in the ε versus (ε+Δ+E) display as a threshold was set on $\Sigma (= (\varepsilon + \Delta + E))$ to reject particles below 4 MeV.

MeV protons (5.8 mm of silicon), the highest energy protons of interest. Secondly, it supplemented the rejection of the high energy (>33 MeV) elastically scattered protons. These protons passed through the telescope and hence appeared as a fold-back in the high energy end of the Δ versus ($\varepsilon+\Delta+E$) display. By drawing particle rejection loci appropriately, these events could be rejected by software (see section 4.1). Surface barrier detectors were chosen for the ε and Δ detectors because of their high resistance to neutron radiation damage and more importantly of their negligibly thin dead layers. A thick dead layer ($\sim 20\mu m$) in the Δ detector would give rise to a region of discontinuity in the locus of events in the T_3 versus T_4 spectrum, thus introducing an additional uncertainty in the projected spectrum. The thickness of the E detector was chosen so that the total thickness of the telescope was just sufficient to stop the highest energy protons of interest. All protons with a higher energy passed through the telescope and entered the veto detector which then provided a vetoing signal to inhibit the acceptance of this event.

Two slit systems were required, one for the solid Ti-^{3}H target and one for the gaseous ^{3}He target. For the tritium target, only the solid angle defining collimators (rear slits) were essential but to block out the events resulting from the proton beam interacting with the Kapton-H foil windows, baffles were introduced. These were simply brass plates mounted in front of the collimator to form a shield for events not originating from the tritium target (see Fig.3.2.7). The use of these baffles was found to reduce the

background significantly. The collimators were made of tantalum whose thickness was just sufficient (2.5 mm) to stop the incident proton beam. The use of such high density material allowed the use of thin collimators and hence resulted in a reduction in slit edge scattering. The solid angle defining collimators had apertures of rectangular dimension (5.537 mm wide by 10.668 mm high) and were placed at 11.630 cm from the centre of the chamber. This corresponded to an angular acceptance of $\Delta\theta = \pm 1.375^{\circ}$ and $\Delta\phi = \pm 2.65^{\circ}$. The choice of these values was determined primarily by the cross section of the reaction and the beam time available.

For the ^{3}He gas target, a double slit system had to be used to define the gas target thickness uniquely. Since the aperture of the rear slit is finite, the effective solid angle of an element of detector area varies from point to point on the rear aperture. This variation is commonly represented by a G-factor which may be defined in the following way. Let the target be divided into thin sections perpendicular to the incident beam direction. From an element of thickness Δt, the number of counts in a channel ΔT corresponding to an energy T_3 is

$$\Delta Y(T_3) = \frac{d^3\sigma}{d\Omega_3\, d\Omega_4\, dT_3}\, \Delta T \cdot \Delta\Omega_3 \cdot \Delta\Omega_4 \cdot \Delta t \cdot I \qquad (2)$$

The geometrical (G) factor may be defined as

$$Y(T_3) = \frac{d^3\sigma}{d\Omega_3\, d\Omega_4\, dT_3}\, \Delta T \cdot G \cdot \rho \cdot I \qquad (3)$$

where I is the total number of protons incident on the target, ρ is the density of the gas. It is clear that G represents a five-fold integral over the two rear aperture areas and over the target thickness in the direction of the beam, the Z-axis, i.e.

$$G = \int d\Omega_3\, d\Omega_4\, dz \qquad (4)$$

The integral has generally been evaluated numerically. Different programs exist for this G-factor calculation all of which give the same result although different mathematical approaches were used (Ba68, Ro69,Fr72b). The program used for the present experiment was that due to Bar-Avraham and Lee (Ba68). Minor modifications to the program were made to make it applicable to a rectangular rear aperture. The collimators, being identical for both detector telescopes, had identical front and rear aperture dimensions of 5.537 mm wide by 10.668 mm high. The front and rear slits were respectively 4.40 cm and 11.63 cm from the centre of the chamber. With this configuration the G-factor distribution for the case of $\theta_3 = \theta_4 = 38.7^\circ$, $\phi_{34} = 180^\circ$ has been calculated and is shown in Fig.3.2.9. The area under the curve represent the total G-factor as defined in equations (3) and (4). A general feature worth noting from the graph is that the highest transmission occurs at an angle pair setting higher than the central one viz. 38.7°-38.7°.

The finite angular acceptance leads to kinematic broadening. Fig.3.2.10 shows the kinematic loci for the central and the two extreme angle pairs. For the ^{3}He case, the extremes were taken as the values at FWHM of the curve shown in Fig.3.2.9 rather than the geometrically allowed extremes. An important feature to be noted is that for these two angle pair settings, both being spectator angle pairs for the respective reactions, the broadening is negligible for the region between about 10 to 26 MeV which are also the regions where the QFS enhancement occurs. It should be mentioned that $\Delta\phi$ effects have not been included in the plots. The program MOMRATH

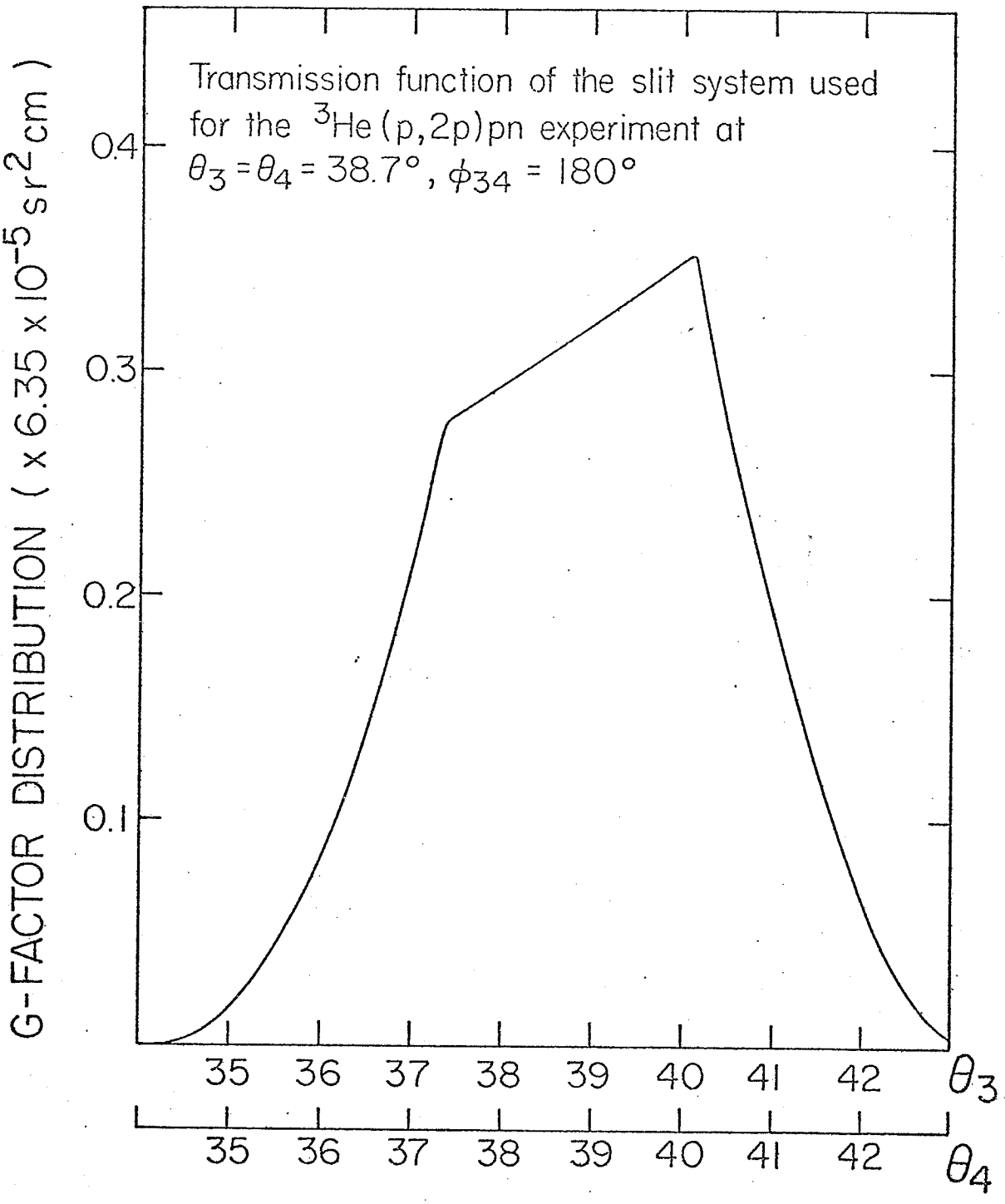

Fig.3.2.9: Transmission characteristics of the slit system used for the ^{3}He(p,2p)pn experiment at $\theta_3 = \theta_4 = 38.7°$, $\phi_{34} = 180°$. (see text for details of the dimensions)

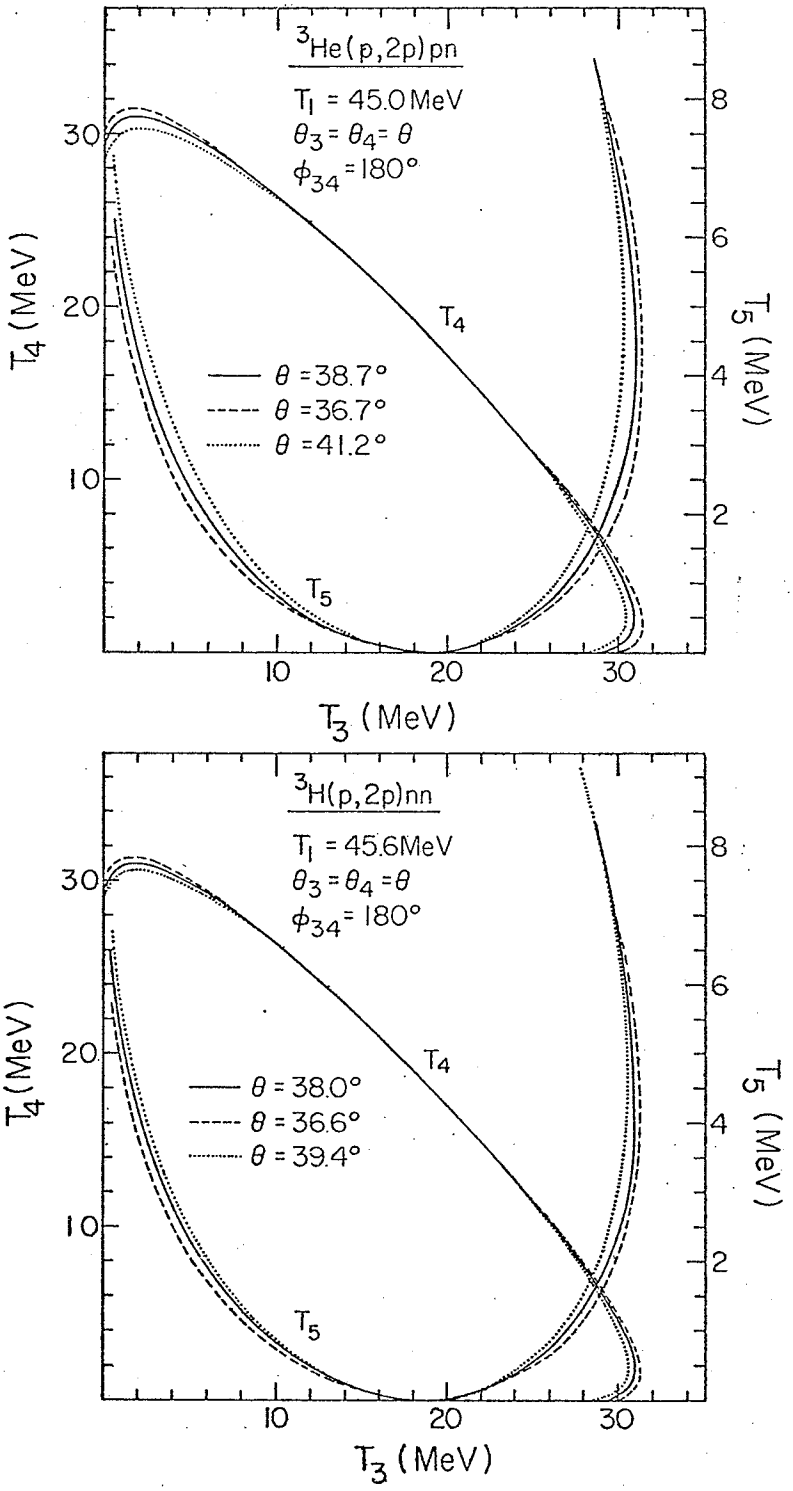

Fig.3.2.10: Kinematic broadening resulting from the finite angular acceptance of the collimators.

(Wa69) has been used to investigate the $\Delta\theta$ and $\Delta\phi$ effects simultaneously. The results indicated that the broadening remained insignificant.

3.2.4 Electronics and computer software

The electronic circuitry, shown in Fig.3.2.11 was composed entirely of commercial modules in standard NIM bins. The use of software particle identification considerably simplified the circuitry which consisted of a fast timing circuit to separate the real and random coincidence events and six energy signals to be processed. The signals from the detectors were first amplified by Ortec 109A preampliers which were placed next to the scattering chamber to reduce the cable length to an absolute minimum. Outputs from these preamplifiers were patched from the experimental area to the cyclotron control room where the major electronics racks and the PDP 15/40 computer were located. The signals were all amplified using Canbera 1416 amplifiers. Timing signals were derived from the two $\mathcal{E}$ signals, using Ortec 463 constant fraction discriminators. Due to the small amplitude of the $\mathcal{E}$ signals, the signal to noise ratio was generally very poor with cyclotron radio frequency (RF) pick-up being the dominant noise source. To eliminate this RF noise, each $\mathcal{E}$ signal was first fed into a fast amplifier (LeCroy 133) whose output was connected to the input of a timing filter amplifier. At this connection, the use of a T-connector allowed a clipping stub to be connected as shown in Fig.3.2.11. The clipping stub was a thick-shield 50 ohm cable shorted at one end, whose length was exactly 3/2 times the wave length of the signal from the main cyclotron oscillator. Reflected signals from this clipping stub would therefore

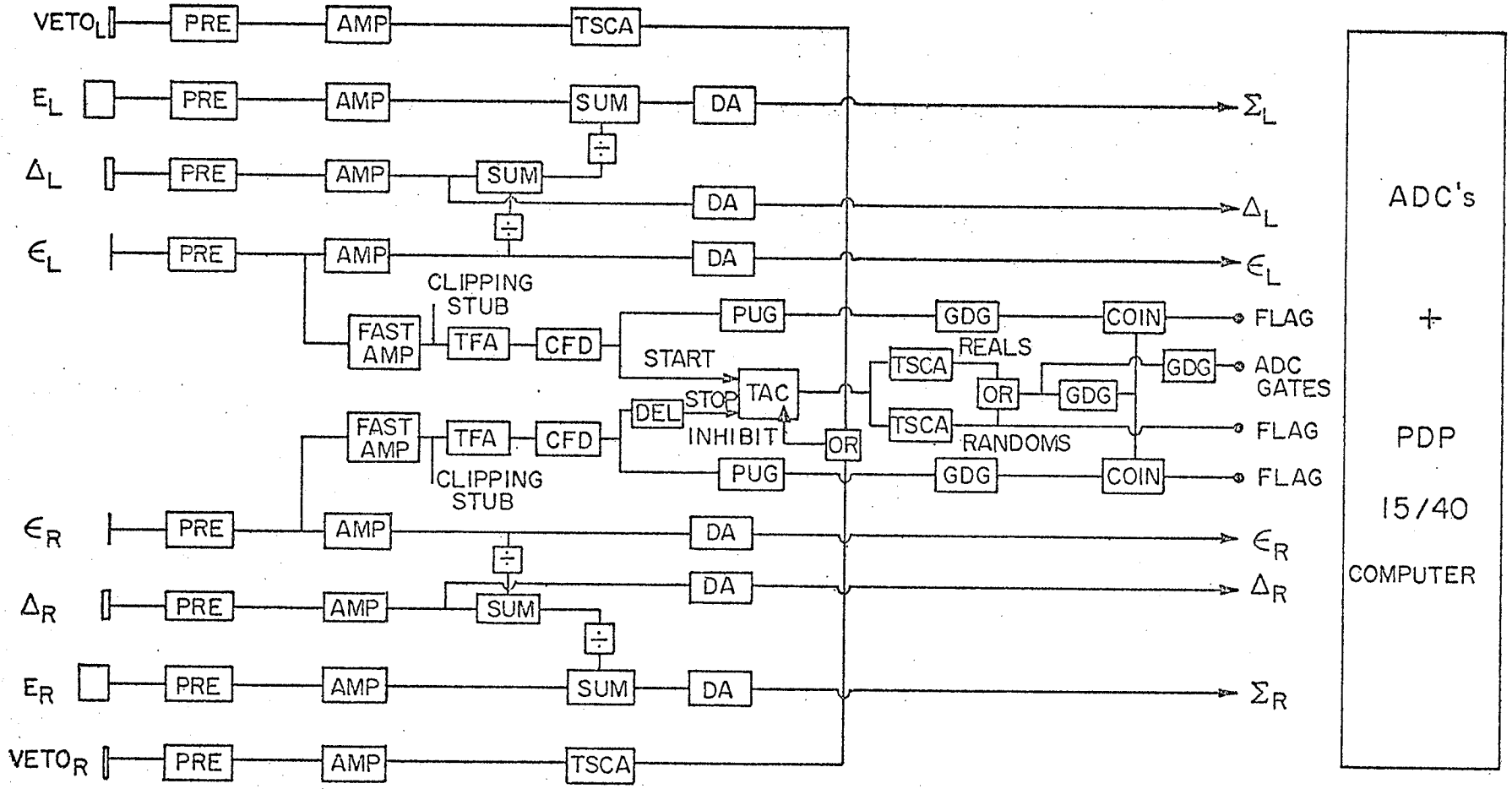

Fig. 3.2.11: Schematic block diagram of the electronic circuitry used for data collection.

PRE:	preamplifier	AMP:	amplifier
TFA:	timing-filter amplifier	SUM:	summing amplifier
CFD:	constant fraction discriminator	DEL:	delay unit
TSCA:	timing single-channel analyzer	DA :	delay amplifier
PUG:	pile-up gate	TAC:	time to amplitude converter
OR :	logical OR unit	GDG:	gate and delay generator
COIN:	coincidence unit		

cancel the incoming RF noise at the T-connector. This method of suppressing the RF noise was found to be highly satisfactory. Moreover, it would not change the timing characteristic of the ϵ signals as would be the case if RF suppressors (a simple R-C high-pass filter)had been used. The improved ϵ signals were than amplified by the timing filter amplifiers before entering the constant fraction discriminators which had a timing method superior to that of both the leading edge and cross-over techniques. These two timing signals triggered a Nuclear Enterprises time to amplitude converter (TAC). A timing resolution within the 35 nano second separation of cyclotron beam bursts was obtained, thus allowing clean separation of the 'reals' and 'randoms' peak. Two TSCA's were used to put windows on the 'reals' and 'randoms' peaks. The 'randoms' signals were fed into the computer as flag bits. The 'reals' signals were used to gate signals from the pile-up gates which were set to produce a pulse for events occuring within 4 micro seconds of each other. The pile-up rejection signals were also recorded as flag bits. Veto pulses arising from high energy protons reaching the veto detector after passing the telescope were used to inhibit the TAC. The ϵ,Δ, and E signals were summed to give the total energy signal. Appropriate attenuations had to be made to the ϵ and Δ signals before being summed since these signals already had amplitudes of about +7 volts. A final timing adjustment was made to all the six linear signals so that they all arrived at the ADC's simultaneously. Each one of these signals was gated at the ADC by the 'ADC Gates' signals which might be the 'reals' or 'randoms' signals. The ADC's used were three

Northern Scientic (Model 625) Dual ADC units**. Scalers were connected to all linear and logic outputs. In addition, the TAC spectrum was stored by a 4000 channel Nuclear Data analyser and was displayed for continous monitoring.

Data acquisition was performed using the program MULPAR (Mi72). In the first and second run, the unprocessed data were stored as 18 bit computer words on DEC magnetic tapes. The analysis was subsequently done off-line. For on-line display and monitoring purposes, an external (application-dependent) processing routine is used in conjunction with MULPAR. This routine is capable of performing particle identification and storing the processed words into regions of computer memory.

Provision is made by the program to display live on a CRT screen either a 64x64 differential contour display or a 512x512 twinkle display. The variables on the axes may be chosen to be any of the six energy inputs and for either protons or deuterons. The selection commands are usually issued through the teletype at the beginning of the run although they can be changed at any time. If required, a Moseley plotter may be made to produce scatter plots of the currently displayed 2-D spectrum on-line. Figure 3.2.12 shows samples of such scatter plots. The X-axis (T_4) and Y-axis (T_3) correspond to the Σ inputs of the left and right detector telescopes respectively. Each point plotted represents one recorded event. The on-line scatter plots shown contain both 'reals' and

** The computer interfaces were designed by C.A.Miller and built in the electronic shop of the physics department.

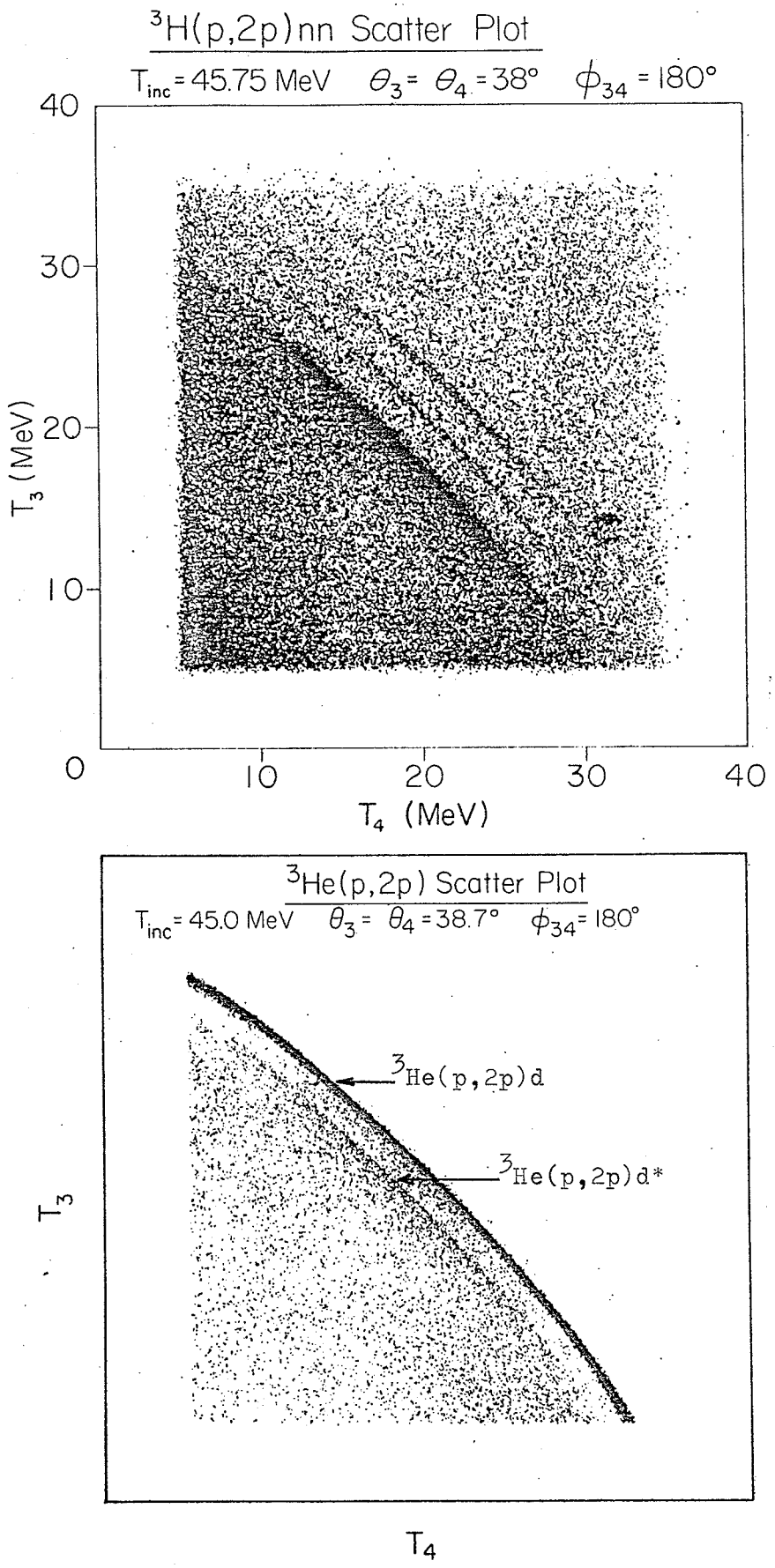

Fig.3.2.12: On-line scatter plots of the (p,2p) reaction on ^{3}He and ^{3}H. Randoms events have not been subtracted. The pronounced band in the ^{3}He scatter plot corresponds to the ^{3}He(p,2p)d reaction. In the ^{3}H scatter plot, bands arising from the contaminant reactions D(p,2p)n and ^{3}He(p,2p)d are clearly visible.

'randoms' events which can only be separated off-line. A light pen, used together with the switches of the computer, allows particle identification loci to be drawn on the display screen. To prevent logging irrelevant events, sample ε versus Σ spectra (Fig.3.2.8) are obtained before data accummulation. Crude particle identification loci are then drawn around the particles of interest. Events outside these loci will not be recorded during data-taking. Data written on the magnetic tapes are identified by their file names, recorded at the beginning of each tape. Typically, if both proton and deuteron events are recorded, each angle will take from 5 to 30 DEC magnetic tapes.

The computer also provides a scaler-enable signal to stop the scalers when the program is stopped e.g. when a stop command is issued by the experimenter, or to start the scalers when the program is started. To correct for the ADC dead times, the current integrator's digitized output is fed into the external live clock inputs of the ADC's. The program then writes a real time F-cup counts on magnetic tape along with the other information. It is this number which will be used for calculating the cross sections.

3.3 Experimental procedure

Before data collection could commence, a typical experimental run would involve the following:

1. Beam optics adjustment: With the scintillator screen in place, the beam spot was adjusted until it was properly centred and had a size less than 1/8" wide by 1/4" high by suitably changing the beam optics.

2. Gain matching: A crude matching of the gains of the $\mathcal{E}$, Δ and E amplifiers was first obtained by means of a pulser. Subsequently, accurate matching of the gains was obtained from the groups of elastically scattered protons and deuterons when using the CH_2 and CD_2 targets respectively. The energies of the protons and deuterons followed from kinematics, correcting for energy loss.

3. Energy calibration for both energy axes: This was done by detecting p-p elastic scattering events in coincidence at many angle pairs to cover the energy range of interest.

During data taking, the tritium content of the Ti-^{3}H target was monitored between runs by means of p-^{3}H elastic scattering. A NaI scintillation detector, mounted on the outside of the scattering chamber at an angle of 67.5°, was used to accumulate singles spectra (see Fig.3.2.13) from the tritium target. The peaks not labelled in the figure correspond to elastic and inelastic scattering from titanium and gold. Although no changes in the tritium content were observed during data taking periods (typically seven days) monitor runs indicated that the tritium content decreased by $\sim 5.0\%$ three months later when it was used in the second run. Loss of tritium due to its radioactive decay accounts for 1.5%. However, it is not certain what causes the loss of the remaining 3.5%.

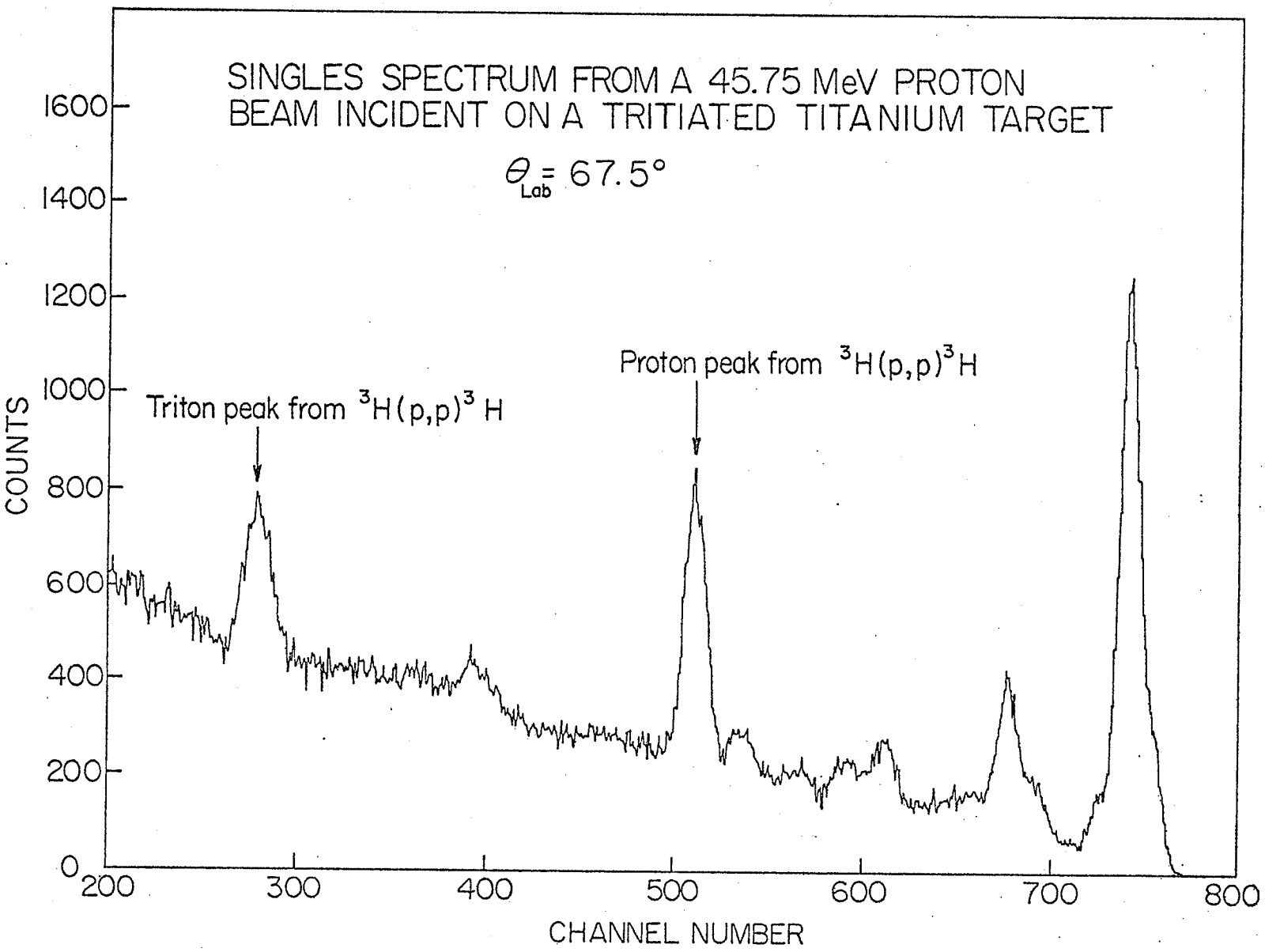

Fig. 3.2.13: 'Singles' spectrum from a 45.75 MeV proton beam incident on a tritiated titanium target at $\theta_{lab} = 67.5^{o}$.

4. DATA REDUCTION

4.1 Software particle identification

As mentioned in section 3.2.4, the program MULPAR logs unprocessed data on magnetic tape in the form of 18-bit words. Each event consists of six digitized energy signals ($\mathcal{E}_L, \Delta_L, \Sigma_L, \mathcal{E}_R, \Delta_R, \Sigma_R$) which are ADC data and three flag bits (randoms flag and pile-up rejection flags for left and right telescopes) which are states of binary digits. The function of the analysis program, PETE, is to particle identify all the events. In an analysis run, precise particle identification (rejection) loci are first defined from sample $\mathcal{E}$ versus Σ (Δ versus Σ) spectra by means of the light pen facility (see Fig.3.2.8). Two parameters are then selected (Σ_L versus Σ_R) and a set of criteria specified (e.g. protons on left telescope and deuterons on right telescope). The program scans the tape for events for which both parameters satisfy the respective criteria. An eligible point results if all the imposed constraints are satisfied. These points may be added to a list of previously discovered eligible points and form a particle identified Σ_L versus Σ_R array which may be displayed on the screen. Since the 'randoms' signals have been fed in as flag-bits, an analysis scan will result in two Σ_L versus Σ_R arrays, one for the reals+randoms and the other for the randoms alone. Provision is made in PETE to subtract the randoms from the reals + randoms spectrum and have the resultant 'reals alone' spectrum displayed. Except at the most forward angles viz. $\theta_3 = \theta_4 = 25^\circ$, the reals to randoms ratios are always better than 4 to 1.

One disadvantage of this analysis program is that it is only capable of analysing one particle at a time on each of the two

chosen parameters. A fresh scan has to be done for each different particle thus requiring three separate scans to extract the (p,2p), (p,pd) and (p,dp) data.

4.2 Projection of data onto the T_3-axis

In an analysis run, projected spectra can be made and stored of events defined within a set of loci in the Σ_R versus Σ_L (T_3- T_4) array. This set of loci (projection loci) is defined at the beginning of an analysis run in the same way as that for defining the particle identification loci except that the loci now enclose the events of interest. The projection is equivalent to summing in columns (to project on the X-axis) or in rows (to project on the Y-axis) of the two dimensional array excluding the events off the loci. The total number of channels in the spectrum may be selected to make the best compromise between statistics and channel resolution. In the present experiment, a full scale of 64 channels has been selected and the results of these projections are to be calibrated in energy and converted to differential cross section in the manner discribed in section 4.4.

4.3 Special treatment of the four-body events

The analysis procedure mentioned so far has been performed on the PDP 15/40 computer. However, the light-pen facility is only adequate for drawing projection loci (in 64x512 resolution) for three-body events which are well defined in a T_3 versus T_4 display (see Fig.3.2.12). For the four-body events (^{3}H(p,2p)nn and ^{3}H(p,2p) pn), the light-pen facility cannot define a locus of constant relative energy T_{56} of the unobserved pair of particles accurately.

For this reason, for the (p,2p) data, new T_3 versus T_4 arrays are generated in 128 x 128 channel resolution. Particle identification was performed at the time of generation of the new arrays. These arrays are first stored on DEC magnetic tape and later transferred via the data link to the IBM 360/65 computer which in turn writes the data onto 9-track magnetic tape.

Once the energy calibration is specified, each event in the T_3 versus T_4 array has a unique (T_3, T_4) value and hence a unique value of T_{56}. Curves of constant T_{56} are shown in Fig.2.1.3(a). It is clear that by scanning all points in the T_3 versus T_4 array and requiring that the values of the calculated T_{56} be within a certain range, one can make projections onto either one of the energy axes for events lying between a given interval of T_{56}. For both the ^{3}H(p,2p)nn and ^{3}He(p,2p)pn arrays, an interval has been chosen to include events corresponding to the n-n and n-p pair having T_{56} between 0 and 1.8 MeV, denoted respectively, as the [nn] and d* systems.

Moreover, missing mass spectra can be obtained from these (128 x 128) arrays in a similar manner. For each point in the (T_3, T_4) array, the corresponding value of the missing mass M_{56} can be calculated from kinematics. The expression is

$$M_{56}^2 = q_{56} \cdot q_{56}$$

$$= (q_1 + q_2 - q_3 - q_4) \cdot (q_1 + q_2 - q_3 - q_4) \qquad (1)$$

where q_i is the four-momentum for particle i. Evaluating the dot product explicitly in terms of T_3, T_4 and other known quantities

yields

$$M_{56}^2 = (m_1+m_2-m_3-m_4)^2 + 2T_1(m_2-m_3-m_4) + 2T_3(m_4-m_2-m_1) + 2T_4(m_3-m_2-m_1) + 2(T_3T_4-T_1T_3-T_1T_4) + 2(p_1p_3\cos\theta_3 + p_1p_4\cos\theta_4 - p_3p_4\cos\theta_{34}) \quad . \qquad (2)$$

Thus, by scanning a complete array, one can sum the events for constant bins of M_{56} to produce the so-called missing mass spectra. No attempt has been made to convert the number of counts to cross sections for these spectra since the number of counts depends on the cut-off of each energy axis. The cut-off arises from protons stopping in the E detector.

It should be mentioned that the (128 x 128) arrays generated consist of 'reals+randoms' and 'randoms' arrays so that appropriate subtraction has to be carried out before projections can be made. In addition, subtraction of the titanium-gold events, normalized to the same number of integrated charge counts has also to be done before final spectra can be obtained. These reduced (128 x 128) arrays have been plotted in a three-dimensional representation and are shown in Figs.4.3.1, 4.3.2, 4.3.3. Except for the angle pairs $\theta_3 = \theta_4 = 50^\circ$ and $\theta_3 = \theta_4 = 60^\circ$, peaks are clearly seen in regions corresponding to the spectator having minimum momentum. The ^{3}He (p,2p) three-dimensional plot should be compared with the scatter plot shown in Fig.3.2.12. It is evident that the three-body events (^{3}He(p,2p)d) are much more prominent than the four body events (^{3}He(p,2p)pn) although QFS peaks are clearly seen for both reactions.

The (128 x 128) dimension was chosen as the best compromise

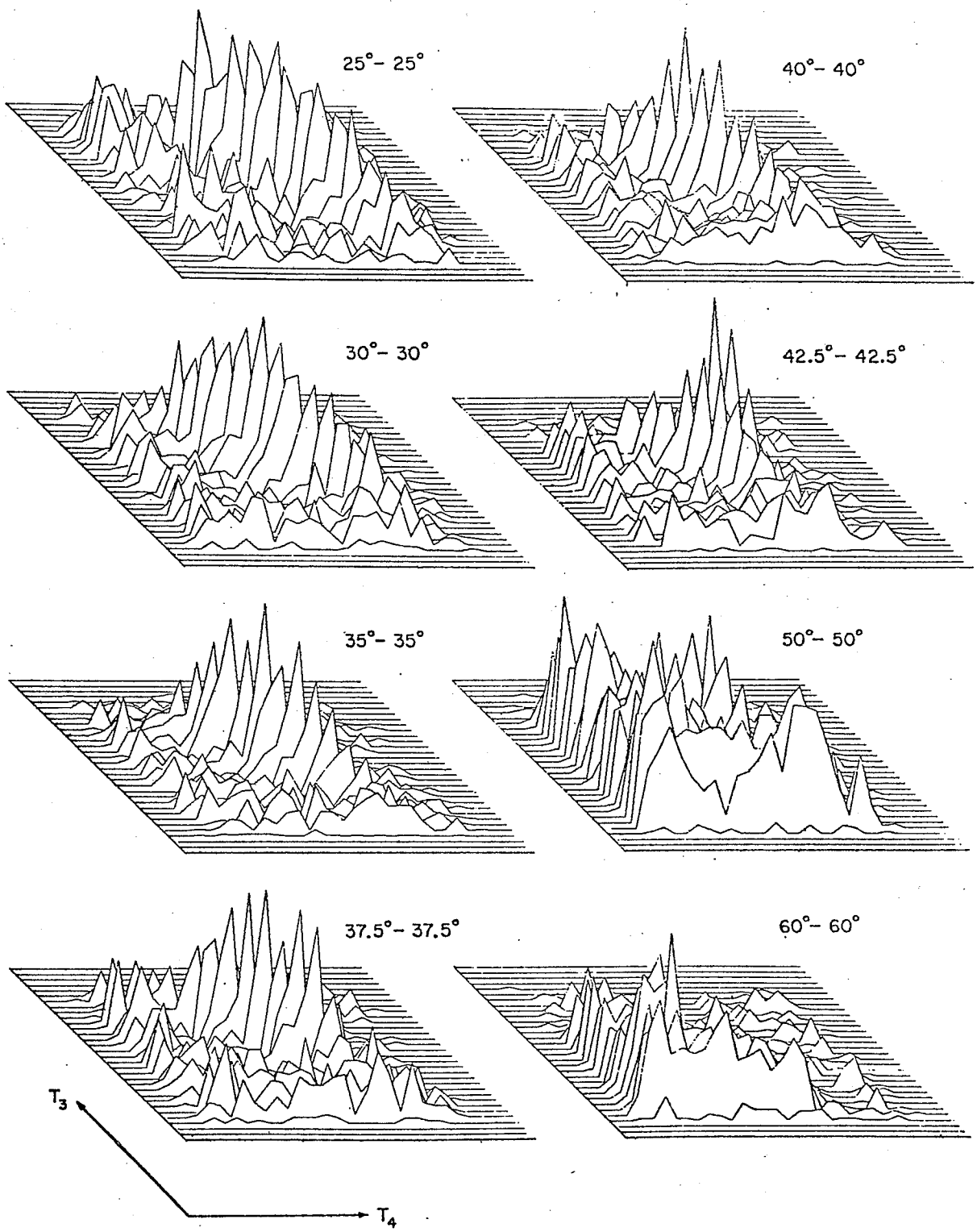

Fig.4.3.1: Three-dimensional spectra for the $^{3}H(p,2p)nn$ reaction at symmetric angle pairs. Except for angle pairs 50^{o}-50^{o} and 60^{o}-60^{o}, peaks are clearly seen in regions where the spectator [nn] momentum is a minimum.

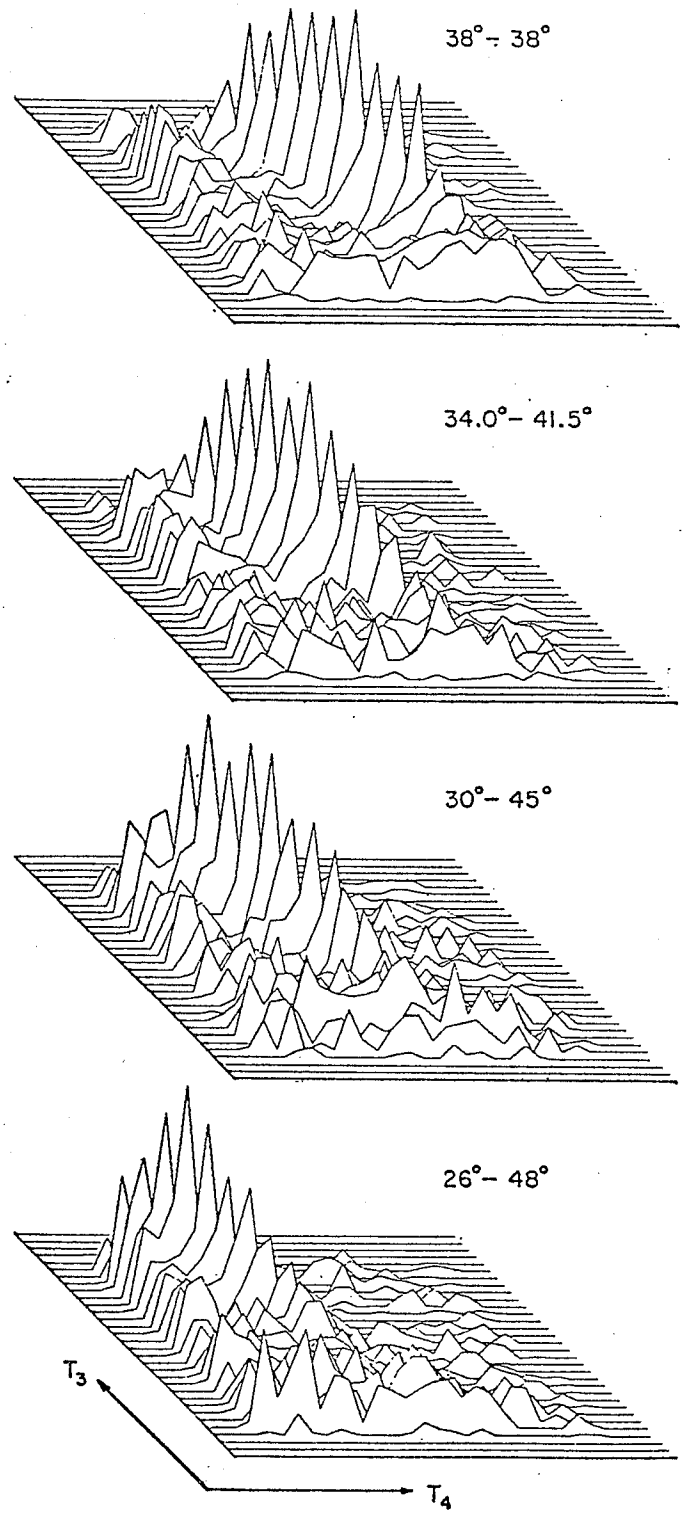

Fig.4.3.2: Three-dimensional spectra for the $^{3}H(p,2p)nn$ reaction. Angles depicted are symmetric and asymmetric quasi-free scattering angle pairs.

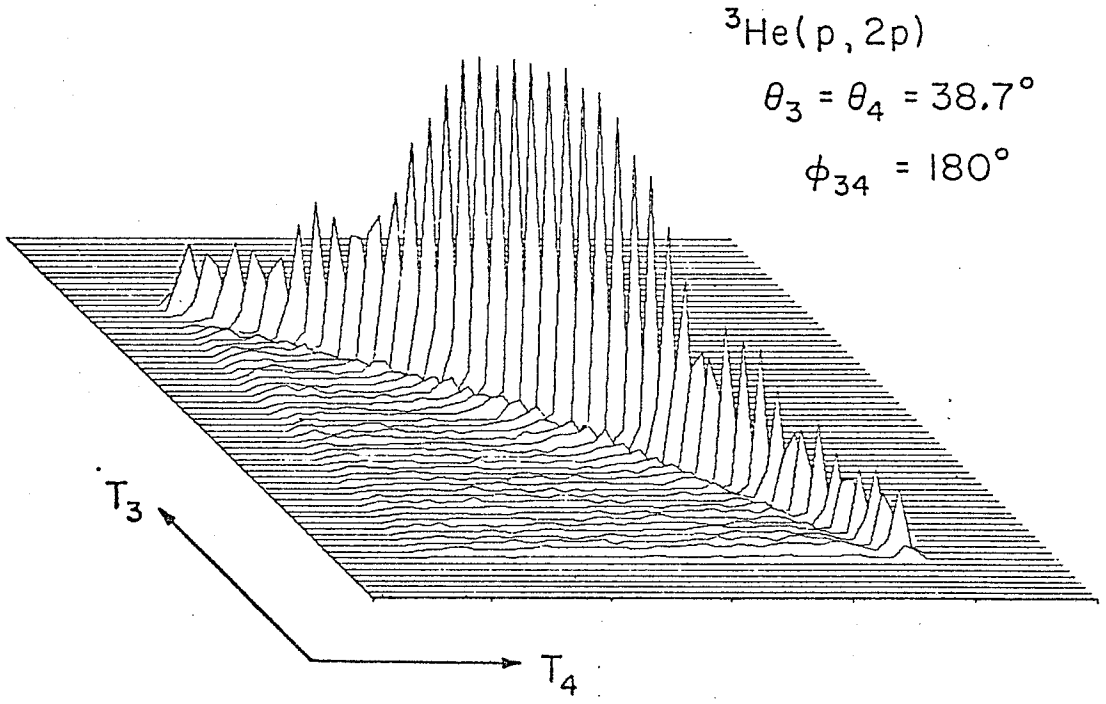

Fig.4.3.3: Three-dimensional spectrum for the ^{3}He(p,2p) reaction. The pronounced kinematic locus corresponds to the ^{3}He(p,2p)d reaction. The quasi-free scattering enhancement for the ^{3}He(p,2p)d* reaction is also evident.

between channel resolution and computer time required. To produce from these (128 x 128) arrays the projected cross sections and missing mass spectra for all the angle pairs required approximately one hour of CPU time of the IBM 360/65 computer.

4.4 Analysis of the Projections

The conversion of the projected spectra from counts versus channel number to cross sections versus energy is relatively straight forward except for a number of corrections. The following procedure was adopted:

1. Energy calibration for the T_3 and T_4 axes:

The energy calibration was obtained by measuring p-p coincidence spectra from ^1H at a number of complementary angle pairs. The spectra appear as blobs of events at positions determined by the angle pair settings. Projections of these spectra onto either axis yield peaks of a Gaussian shape. The energies of these peaks were determined from simple two-body kinematics, with corrections made for the energy lost in getting out of the target. The peak channels were chosen to be the mid-points at half maximum. In both runs, the energy calibration curves for both energy axes followed a straight line with less than 4 channels (out of 1024) offset at the origin. Calibrations before and after each experimental run (separated by seven days) also agreed closely indicating good long term stability of the electronics and the ADC's. A least squares fit is used to obtain the equation of the straight line for each energy calibration. The uncertainty in T is $\lesssim \pm$ 200 keV. This set of calibrations was used in the generation of the projections

and the missing mass spectra.

2. Energy loss correction:

Due to the finite thickness of the target, energy loss corrections had to be made for both the incident beam and the detected particles. For the tritium target, the degrading materials include half the thickness of the titanium, half the thickness of the tritium and the Kapton-H foil window of the containment cell. The first two degraders will have a varying thickness depending upon the angle at which the particles are detected. For the ^{3}He gas target, the interaction is assumed to occur at the centre of the gas cell so the total degrading materials include ^{3}He gas of a thickness equal to the radius of the gas cell and the Kapton-H foil window. The thicknesses of these degraders are clearly independent of the angle of detection. (In reality, the path of interaction extends over a length of 2 cm but the approximation does not lead to any significant discrepancy). Although dE/dx is energy dependent, use was made of the linear relationship of ln (dE/dx) versus lnE:

$$\ln(dE/dx) = c_1 \ln(E) + c_2 \quad . \qquad (3)$$

The constants c_1 and c_2 for each material are found from the ln(dE/dx) versus ln(E) curves over the energy range 5 MeV to 40 MeV, which were obtained using Janni's tabulations (Ja66). Since the stopping power of protons in Kapton-H foil has not been tabulated, it was determined from the equation

$$(dE/dx) = \sum_i F_i (dE/dx)_i \qquad (4)$$

where F_i are the fraction by weight of the ith constituent with stopping power $(dE/dx)_i$. The energy loss is typically 300 keV for proton energies between 5 and 10 MeV and becomes negligible at around 40 MeV.

3. Pile-up corrections:

As mentioned earlier, events occurring within 4 μs of each other were rejected. A correction factor must therefore be introduced which is simply given as

$$\left(\frac{S_L}{S_L - PU_L}\right) \times \left(\frac{S_R}{S_R - PU_R}\right) \qquad (5)$$

where S represents the number of events collected in the ΔE ($\mathcal{E}$) detector and PU represents the corresponding number of pile-up events. The subscripts L and R refer to left and right detector telescopes respectively.

4. Conversion of counts to cross sections:

For the tritium solid target, the differential cross section has been calculated from the equation

$$\frac{d^3\sigma}{d\Omega_3 d\Omega_4 dT_3} = \frac{Y(T_3)}{\Delta\Omega_3 \Delta\Omega_4 \Delta T(T_3) N I} \qquad (6)$$

where $Y(T_3)$ represents the number of counts accumulated in the channel with mean energy T_3, $\Delta\Omega_3$ and $\Delta\Omega_4$ are the solid angles for the two detector systems, ΔT is the width of the channel in energy, N is the number of target nuclei per unit area and I is the total number of protons incident on the target. The value of N was calculated using the manufacturer's specifications while the value of I followed from the real-time integrated charge counts (which is a

number already corrected for ADC dead time losses).

For the ^{3}He gaseous target, the equation has the form

$$\frac{d^3\sigma}{d\Omega_3 d\Omega_4 dT_3} = \frac{Y(T_3)}{G \cdot I \cdot \rho \cdot \Delta T} \qquad (7)$$

where G is the G-factor as described in section 3.2.3, ρ, the density of ^{3}He, is given to a high accuracy by the Ideal Gas Law:

$$\rho = \frac{P}{k_o \theta} \qquad (8)$$

where k_o is Boltzmann's constant and P and θ are respectively, the average pressure and temperature. (Correction for the van der Waal forces amounts to $\lesssim$0.05%). It has been assumed that the number of counts $Y(T_3)$ has already been corrected for pile-up rejections.

Using the above procedure, projected cross sections were obtained for the ^{3}H(p,2p)[nn] , the ^{3}H(p,pd)n, the ^{3}He(p,2p)d and the ^{3}He(p,2p)d* reactions. Figures 4.4.1 and 4.4.2 show projections for symmetric coplanar angle pairs of the ^{3}H(p,2p)[nn] loci. It is evident that a QFS enhancement persists to as high an angle pair as 50°-50°. The peak in each of these spectra occurs at the region where p_5 is a minimum. For the angle pair 38°-38°, p_5 reaches zero while for the other angle pairs, p_5 has a non-zero value. The behaviour of the peak cross sections versus the corresponding momentum transfer is shown in the next chapter. Peak cross sections were obtained from these spectra using a Gaussian peak fitting routine. All points in the peak to be fitted were weighted by their corresponding statistical error. The peak fitting procedure yielded results essentially the same as those obtained when a smooth curve is drawn by eye through the data points around the peak. For the 55°-55° and

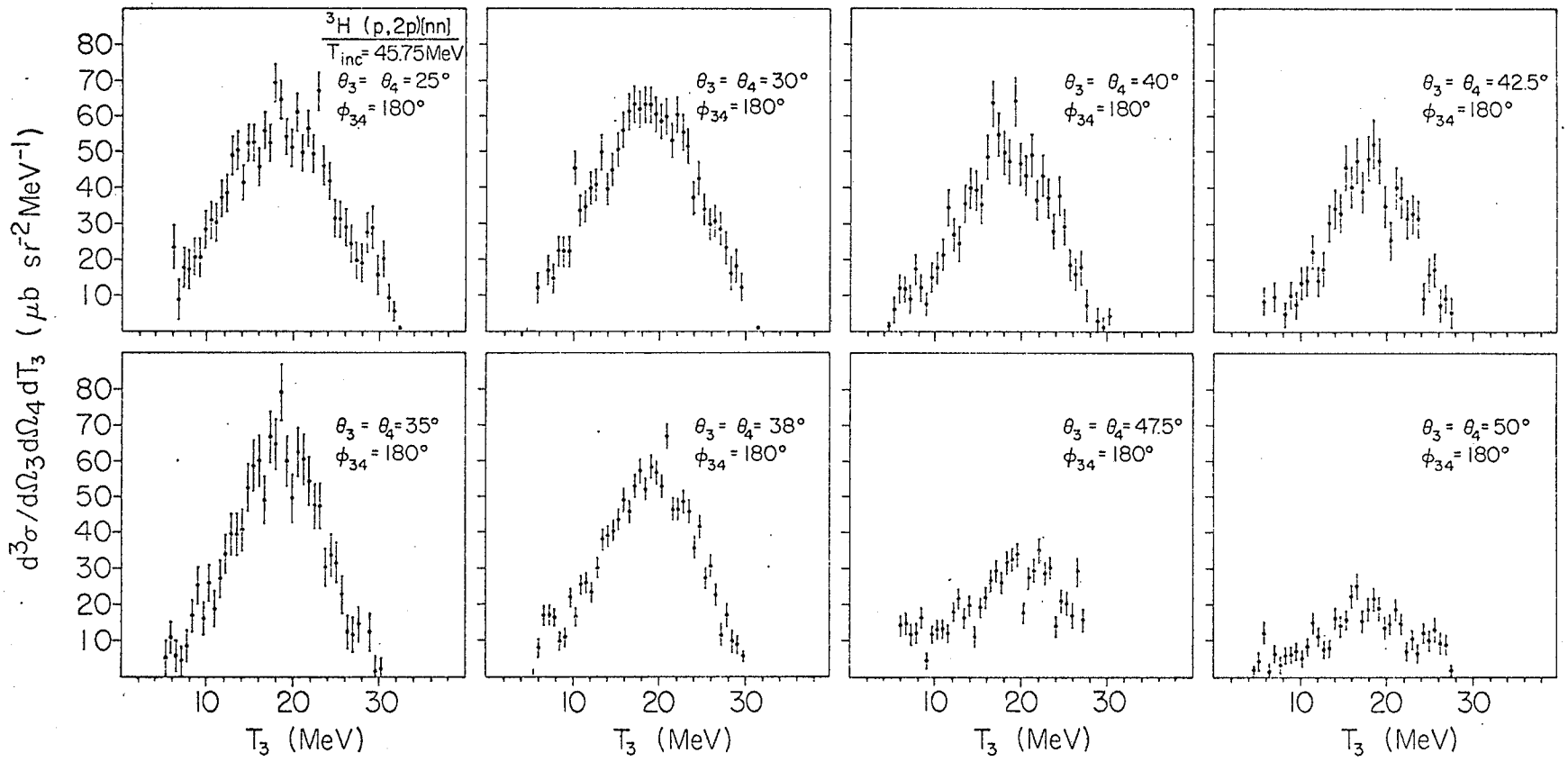

Fig. 4.4.1: Projected cross sections for the ^{3}H(p,2p)[nn] reaction at symmetric coplanar angle pairs. In each spectrum, the peak occurs at an energy where p_s is a minimum.

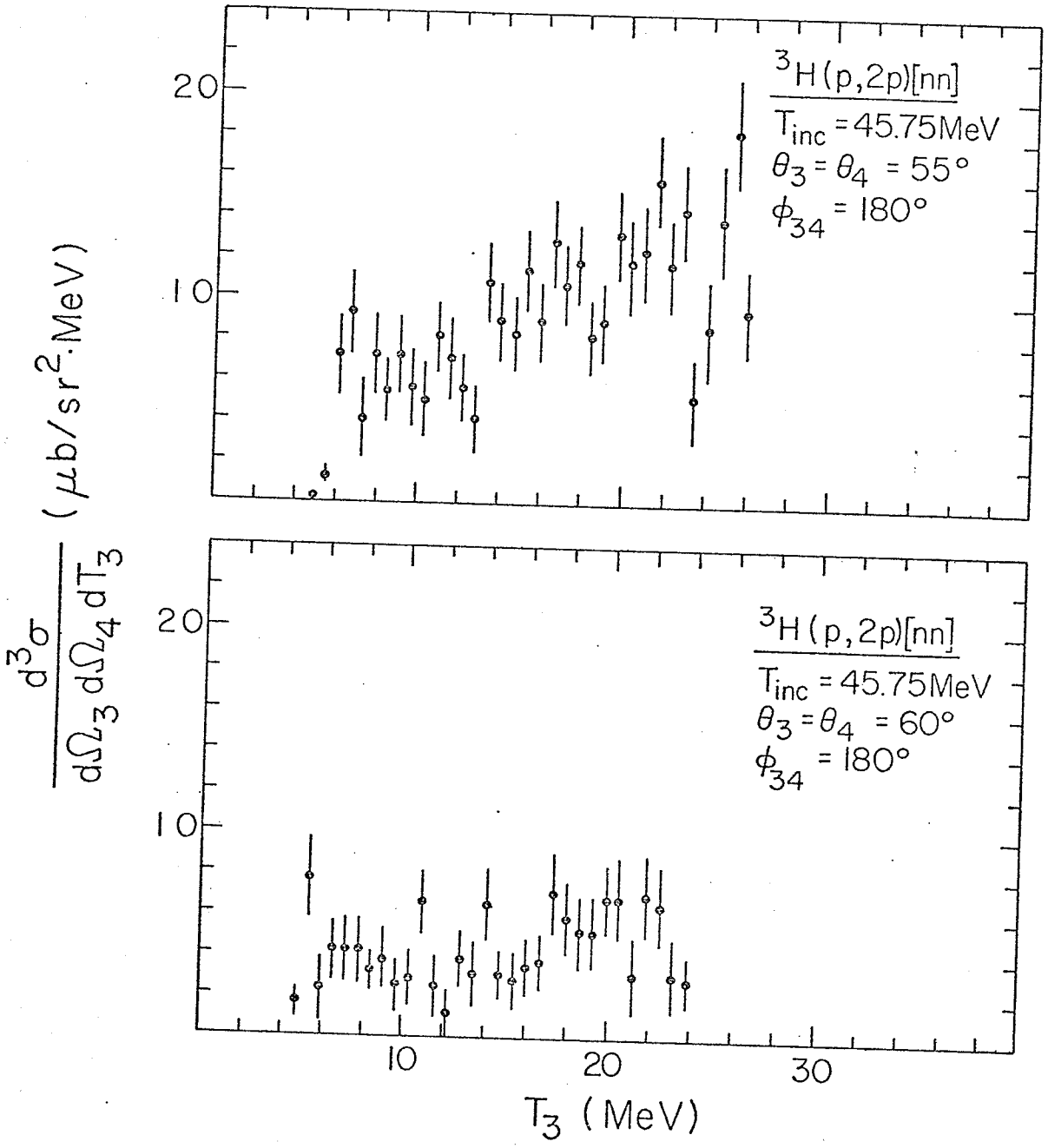

Fig.4.4.2: Projected cross sections for the ^{3}H(p,2p)[nn] reaction at large angles. The QFS peak is no longer observable.

60°-60° spectra where the QFS enhancements are no longer visible, the 'peak' cross section is obtained by averaging the cross section values over a few channels at the region where p_5 is a minimum. Table 4.1 summarises the peak cross sections for the various symmetric coplanar angle pairs. Fig.4.4.3 shows the projections for the asymmetric QFS angle pairs. The QFS peak again occurs at a region where p_5 is a minimum (equal zero in these cases). No attempt has been made to determine the peak cross section from these spectra. However, a momentum distribution has been extracted for each of the spectra (see chapter 6).

Figures 4.4.4, 4.4.5, and 4.4.6 show projections of the ^{3}H(p,pd)n loci onto the proton energy axis. The arrows indicate the proton energy corresponding to a minimum value of p_n ($=p_5$). This value of p_n is also shown in each spectrum. The proton axis was chosen for the projection because a smaller energy loss correction was required for protons compared to deuterons. One interesting feature to be noted from these projections is that except in the two cases ($\theta_p = 47.5^{\circ}, \theta_d = 47.5^{\circ}$; $\theta_p = 60^{\circ}, \theta_d = 41.6^{\circ}$) where the QFS condition is met, the enhancements do not peak at the position where p_n has a minimum value. Similar shifts in the peak positons have also been observed previously by Slaus et al.(Sl71) for the ^{3}He(p,pd)p reaction at 35 MeV. These authors interpreted the shifts as the result of a neutron pick-up process. The peaks appearing on the extreme right of some of the spectra (e.g. $\theta_p = 48^{\circ}, \theta_d = 26^{\circ}$) are only a kinematic effect resulting from the fact that a projection is made of the region of a locus which is starting to curve inwards. Observation of the projection for $\theta_p = 60^{\circ}, \theta_d = 41.6^{\circ}$ (see Fig.4.4.6) shows that the

Table 4.1 Summary of the peak differential cross sections for the $^{3}H(p,2p)[nn]$ reaction at symmetric coplanar angle-pairs.

Gaussian fitted values

θ_3	θ_4	q_{min} (MeV)	Peak $d^3\sigma/d\Omega_3 d\Omega_4 dT_3$ (μb/ sr^2. MeV)	FWHM (MeV)	T_3 at peak (MeV)
25°	25°	-0.210	64.0 ± 3.0**	5.3	18.6
30°	30°	-0.140	67.0 ± 3.0	5.4	18.6
35°	35°	-0.055	64.0 ± 4.0	5.3	18.1
37.5°	37.5°	-0.008	59.0 ± 4.0	5.9	18.2
38°	38°	0.0	58.0 ± 3.0	5.7	18.4
40°	40°	0.045	53.0 ± 3.0	5.5	18.1
42.5°	42.5°	0.100	46.0 ± 3.0	4.9	18.1
47.5°	47.5°	0.225	29.0 ± 2.0	7.0	18.7
			Averaged values		
50°	50°	0.294	21.5 ± 1.5	-	-
55°	55°	0.435	10.0 ± 1.5	-	-
60°	60°	0.6000	3.5 ± 1.0	-	-

** This quoted value corresponds to the standard deviation between the observed values and the fitted values for a group of ten channels around the peak (five channels on each side of the peak).

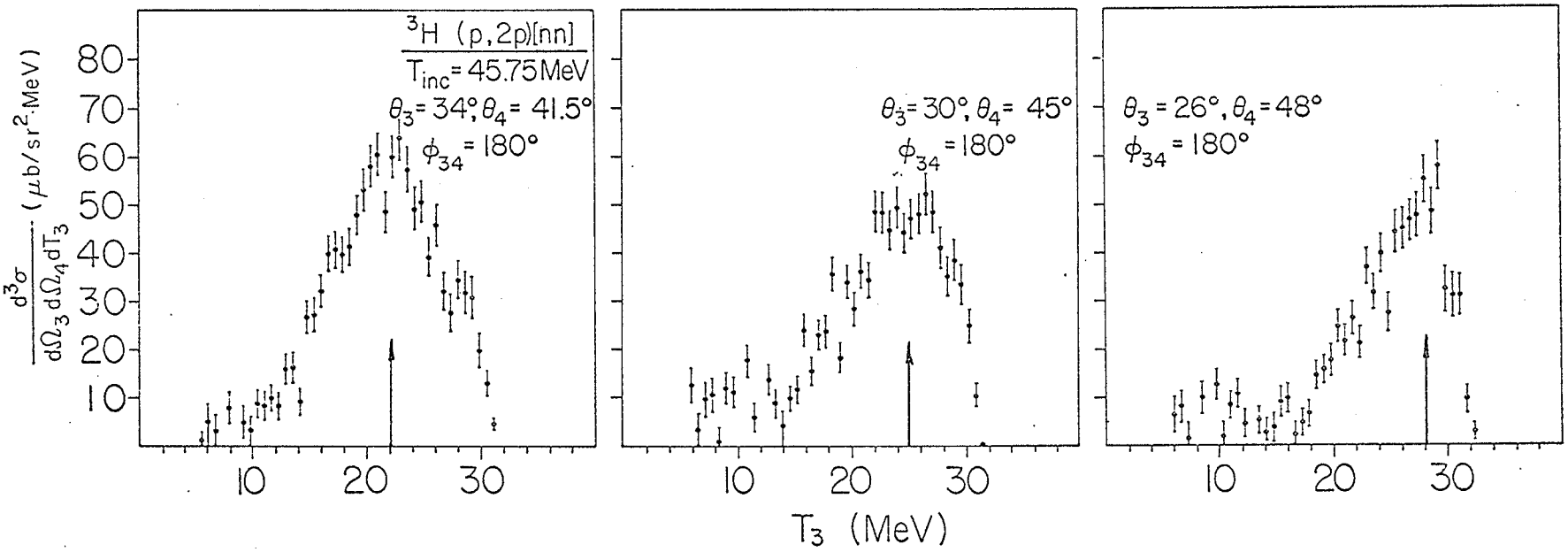

Fig. 4.4.3: Projected cross sections for the ^{3}H(p,2p)[nn] reaction at asymmetric QFS angle pairs. In each case, the QFS peak occurs at an energy where p_5 is a minimum.

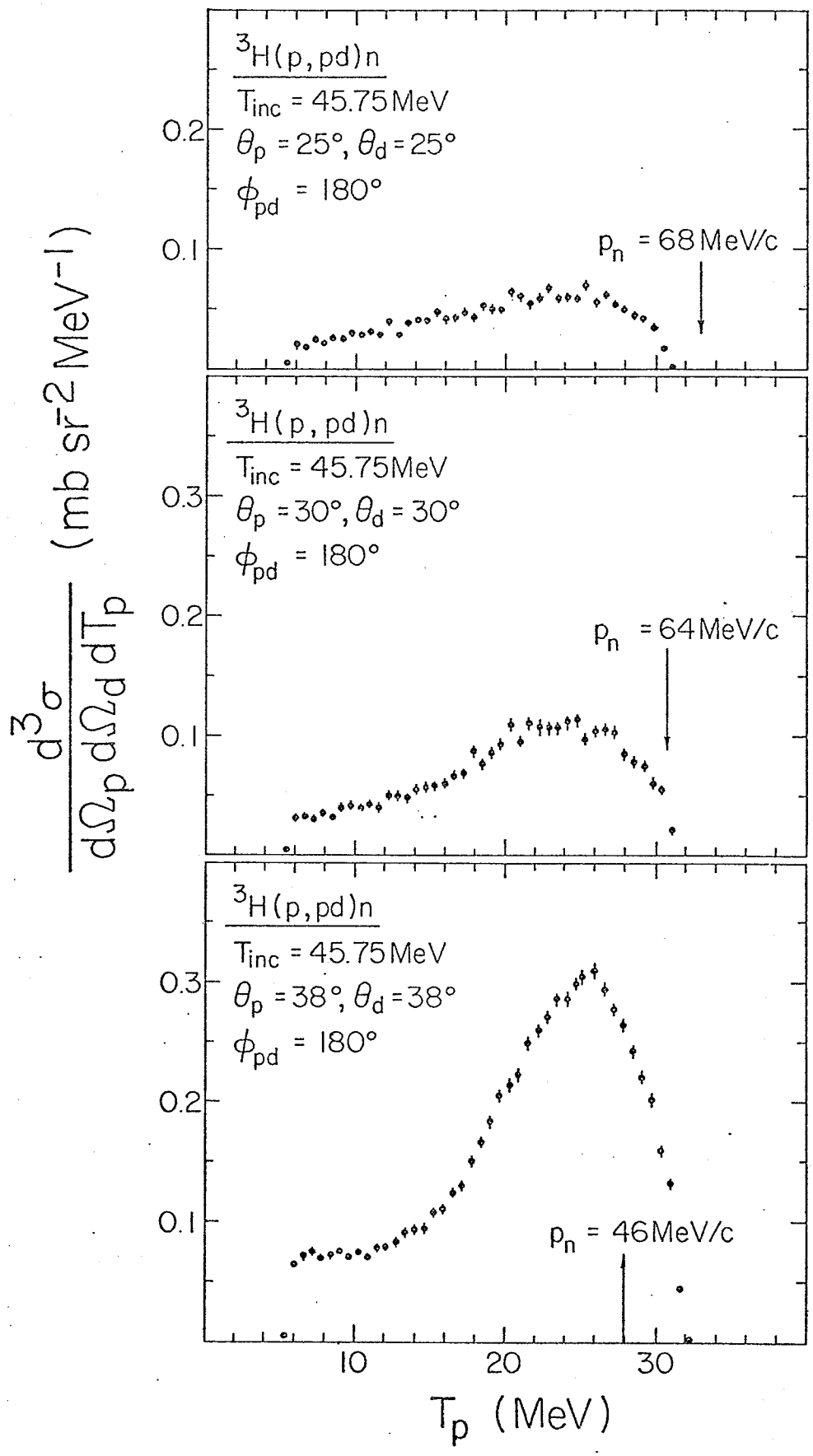

Fig.4.4.4: Projected proton energy spectra for the reaction ^{3}H(p,pd)n at symmetric coplanar angle pairs. In each spectrum, the arrow indicates the energy where p_n has a minimum value.

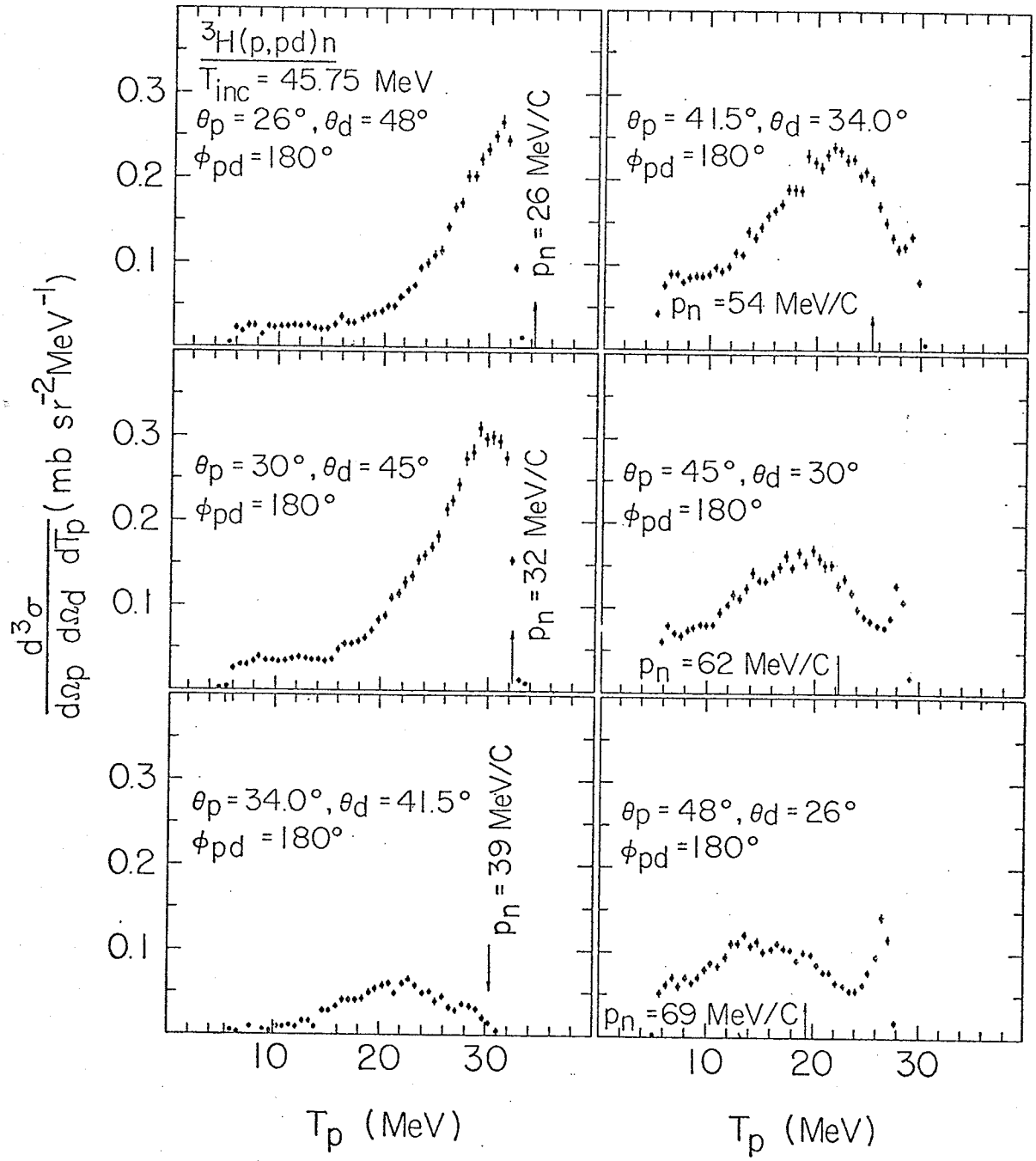

Fig.4.4.5: Projected proton energy spectra for the reaction ^{3}H(p,pd)n at asymmetric coplanar angle pairs. Arrows indicate the energy where p_n has a minimum value.

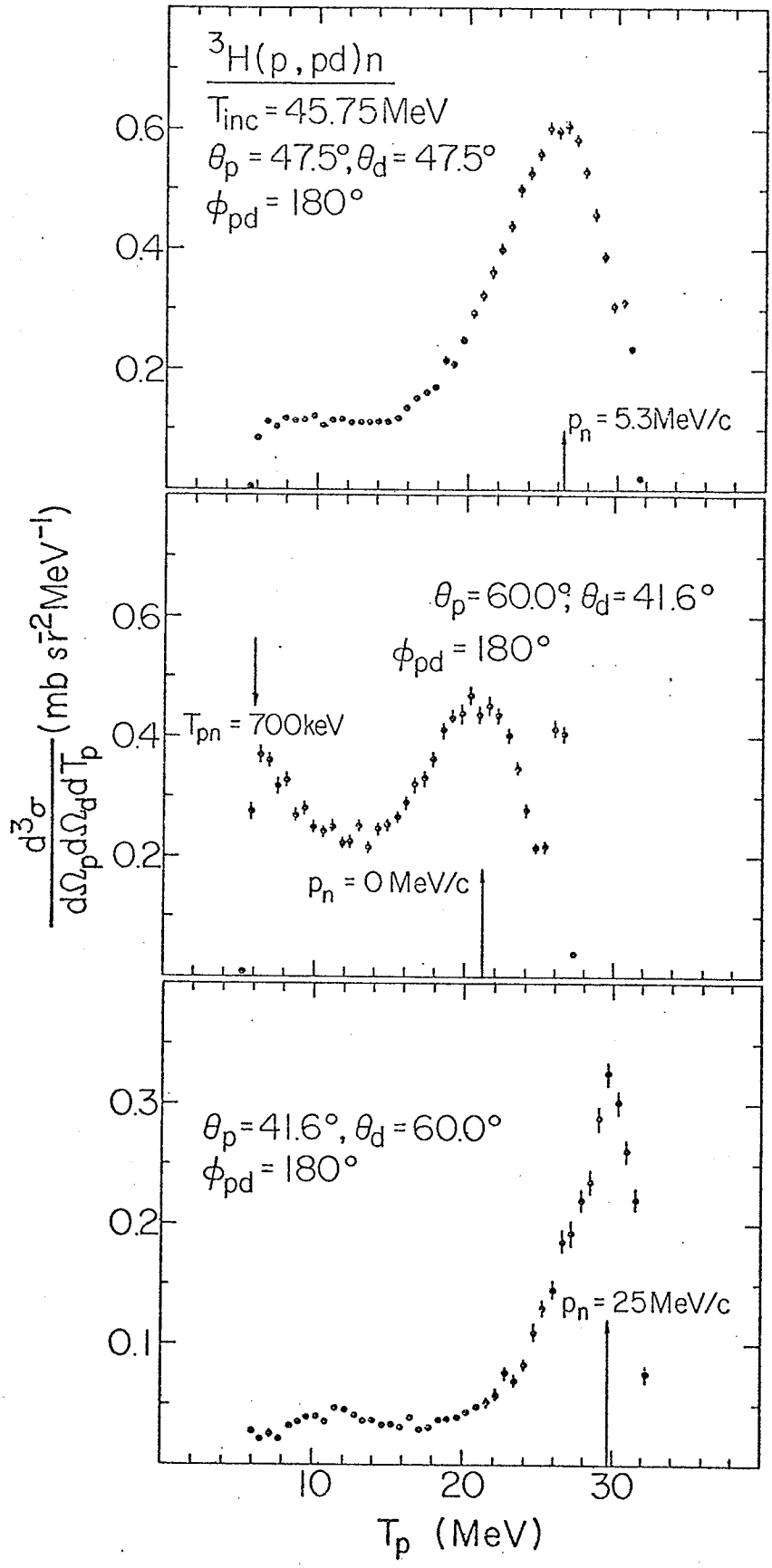

Fig.4.4.6: Projected proton energy spectra for the reaction ^{3}H(p,pd)n. The upper two spectra have kinematics which satisfy the QFS condition. Arrows indicate the energy where p_n has a minimum value.

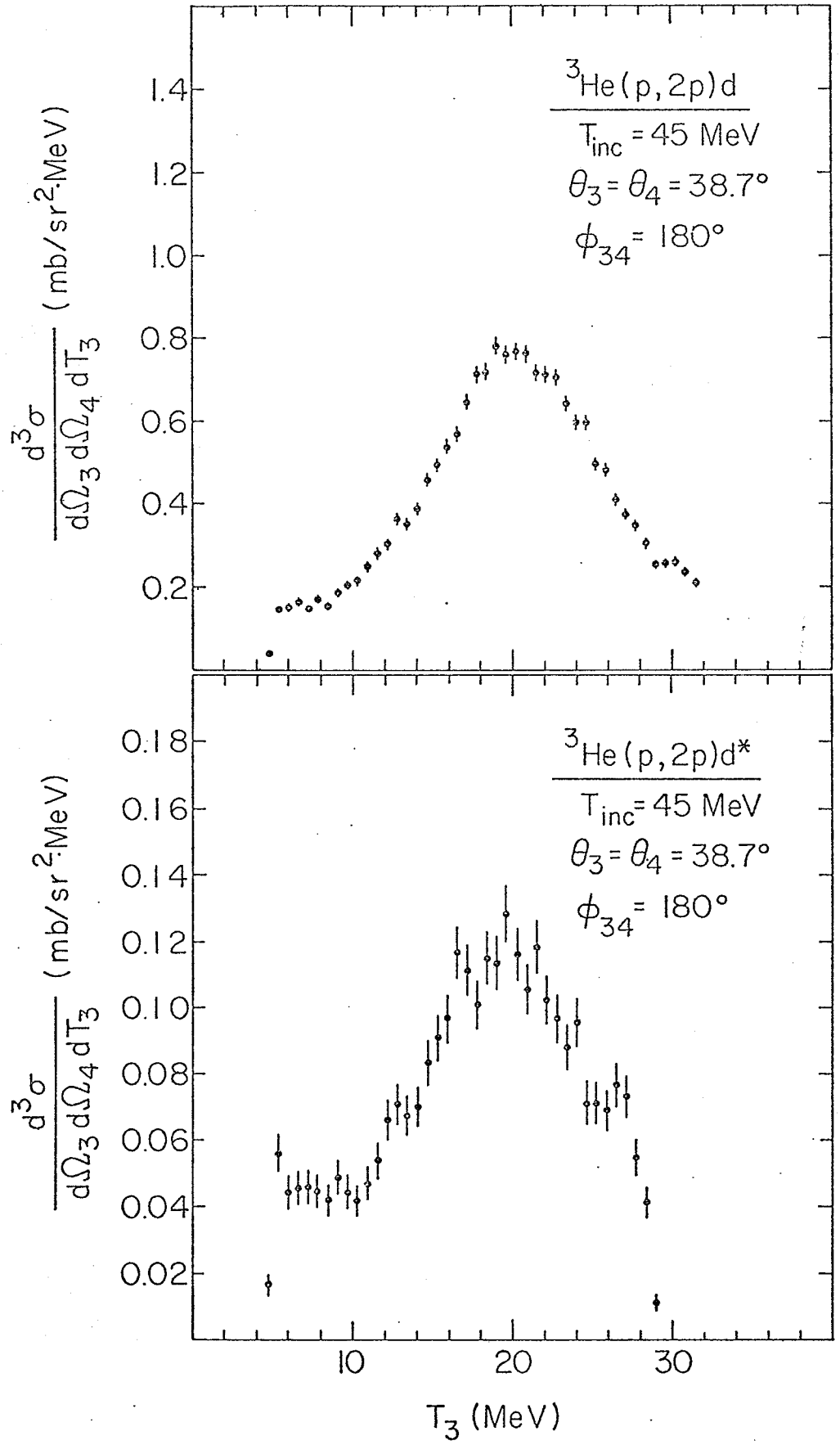

Fig.4.4.7: Projected spectra for the ^{3}He(p,2p)d and ^{3}He(p,2p)d* reactions.

presence of a final state interaction enhancement , indicated by the arrow marked T_{pn} = 700 keV, significantly alters the shape of the QFS peak in its neigborhood. This means that to extract the momentum distribution of the deuteron in ^3H, the spectrum to be used must not contain dominant two-body processes other than QFS. The projection for $\theta_p = \theta_d = 47.5^\circ$ (see Fig.4.4.6) seems to satisfy this condition and will be used for the above purpose. The peak in the spectrum for $\theta_p = 41.6^\circ, \theta_d = 60^\circ$ occurs at the minimum value for p_n although the QFS condition is not satisfied. The reason for the absence of a shift in the peak position in this case is not understood.

Fig.4.4.7 shows the projected spectra for the $^3He(p,2p)d$ and $^3He(p,2p)d^*$ reactions. These spectra have shapes similar to one another and also to those of the tritium spectra. However, an obvious difference exists at the tails of the peak. Specifically, the p-p quasi-free peak from tritium falls monotonically at both ends while the one from ^3He flattens out at around 8 MeV in the low energy end and around 28 MeV at the high energy end. A more detailed comparison will be made in section 6.4.

4.5 Comparison between runs

Fig.4.5.1 shows projected spectra from the $^3H(p,2p)$ [nn] reaction at 30°-30°; taken in the first and second runs respectively. The close agreement in magnitude of the two spectra indicates good reproducibility while the slight shift in energy is well within experimental uncertainties. It should be mentioned that a correction has been made to the yield calculation in the second run for the loss of tritium

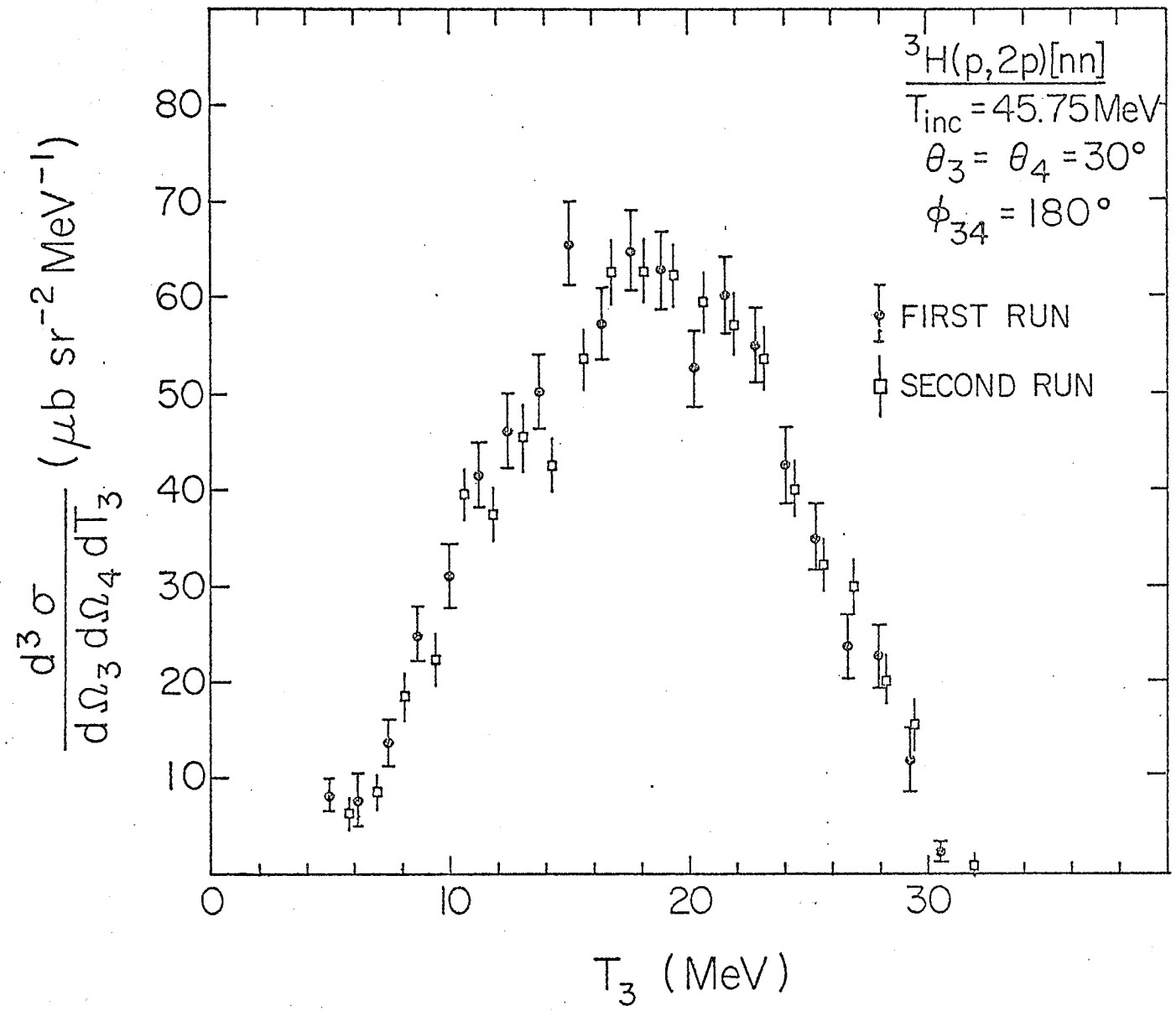

Fig. 4.5.1: Projected spectra of the ^{3}H(p,2p)[nn] reaction at $\theta_3 = \theta_4 = 30^\circ$ for the first and second runs.

due to its decay (1.5%) and an additional loss of 3.5% as indicated by the monitor runs. The cause of this additional loss may be local heating of the target due to the incident proton beam, which tends to diffuse the tritium to the edge of the target. However, calculations indicate that the heat generated by the incident beam in the target is quite small.

5. ERRORS

In this section, a discussion will be given of the errors (relative and absolute) associated with the experimental coincidence cross sections.

Relative errors

The relative error is essentially the statistical uncertainty of the yield and depends on the channel resolution chosen for a given projection. The yield for a given reaction (e.g. ^{3}H(p,2p) nn) was obtained by subtracting the dummy target spectrum from the Ti-^{3}H target spectrum after normalization to the same number of charge integrator counts. (No such subtraction was required for the ^{3}He spectra) The source of error was taken to be counting statistics in the 'reals + randoms' and 'randoms' spectra. Errors were added in quadruture in every subtraction operation to give the final statistical uncertainty. The error bars shown in all the projected cross sections in the previous chapter represent this statistical uncertainty. It can be seen that the uncertainty for the four-body break-up reactions (^{3}H(p,2p)[nn] and ^{3}He(p,2p) d*) is ~10 % while the uncertainty is ~5% for the three-body break-up reactions (^{3}H(p,pd)n and ^{3}He(p,2p)d). This is due to the much lower cross section for the four-body reactions than for the three-body ones.

Absolute errors

Table 5.1 summarizes the major sources of absolute error

associated with the coincidence cross sections for the $^{3}H(p,2p)$ [nn] and $^{3}H(p,pd)n$ reactions

Table 5.1 Major sources of error contributing to the absolute uncertainty of the tritium cross sections

Source	Percentage error
Tritium target thickness determination	~ 5
Solid angle determination	~ 2
Dead time correction	$\lesssim 1$
Pile-up correction	$\lesssim 1$
Loss of incident beam	$\lesssim 1$

The error in the solid angle determination is small since the collimator geometry was measured with high precision using a travelling microscope and precision calipers. The dead times varied from $\sim$0.2% at the high angles to $\sim$2% at the forward angles. These dead times were obtained by comparing the number of Real-time charge integrator counts with the number of Live-time charge integrator counts. The former correspond to charge integrator counts recorded by the computer when the ADC's are not busy. In general, however, there also exists dead times in the electronic modules such as the TSCA and the TAC. These are expected to be small in view of the small dead times indicated by the number of Real-time charge integrator counts. Calculations showed that the divergence of the outgoing proton

beam caused by multiple Coulomb scattering in the titanium-gold backing resulted in 0.02% of the protons not reaching the Faraday cup. Moreover, the proton beam generally had a 'halo' structure of an undetermined dimension. Past experiences have shown that the 'halo' represents $<1\%$ of the total proton beam intensity and should give rise to an uncertainty in the cross section of the same magnitude or less. Taking into account the precision of the target ladder, the target angle could be set to an accuracy of $\sim 0.5^{\circ}$. This corresponds to a negligible error in the target thickness however.

Since the completion of this work in which the tritium content was taken to be the manufacturer's quoted value of 7.6 ± 0.4 curies, Allas et al.(Al73) reported on a measurement of the tritium contents of their Ti-^{3}H target (similar to the one used in the present experiment and made by the same manufacturer) and found it to be 60% below the manufacturer's quoted value. To check the tritium contents of the Ti-^{3}H target used in the present experiment, a measurement of ^{3}H(p,t)p elastic scattering was performed at 19.48 MeV. The data were then normalized against the ^{3}H(p,p)^{3}H differential cross sections of Detch et al.(De71) which have an absolute uncertainty of ~1%. Tritons were detected instead of protons since the latter form a continuous spectrum due to the presence of protons from various reactions in the titanium-gold backing. The (p,t) reaction on the other hand is insignificantly small for both titanium and gold. The experiment was relatively

straightforward and involved the use of a ΔE (100 micron thick 200 mm^2 sensitive area surface barrier) - E (1 mm thick 200 mm^2 sensitive area surface barrier) detector telescope. The collimator geometry defined an angular acceptance of $\Delta\theta = \pm 0.5^{\circ}$. Particle identification was performed on-line by software. The integrated triton peak had counting statistics of approximately 1% for each angle. (p,t) events from the titanium-gold backing were typically less than 1%.

Fig.5.1 shows a comparison of the present data with the data of Detch et al. The error bars are less than the size of the symbols for all data points. In the present data, the triton centre-of-mass angle θ was replaced by $180^{\circ} - \theta$ to correspond to the centre-of-mass angle of the scattered proton. By neglecting the data point at a proton centre-of-mass angle of 98°, the present data agree closely in shape with the data of Detch et al. A nomalization constant was obtained by fitting the present data to the data of Detch et al. With this normalization procedure, the tritium content was found to be 8.05 curies with an estimated error of 3%. It should be mentioned that a correction had been made for the loss of tritium as the result of its radioactive decay (~6%) and as the result of local heating by the incident proton beam (3.5%). The value of 8.05 $\pm$ 0.24 curies agrees with the manufacturer's specified value of 7.6 $\pm$ 0.4 curies within the limits of the respective errors. The slight difference may be accounted for by the fact that the Ti-^{3}H target foil had a

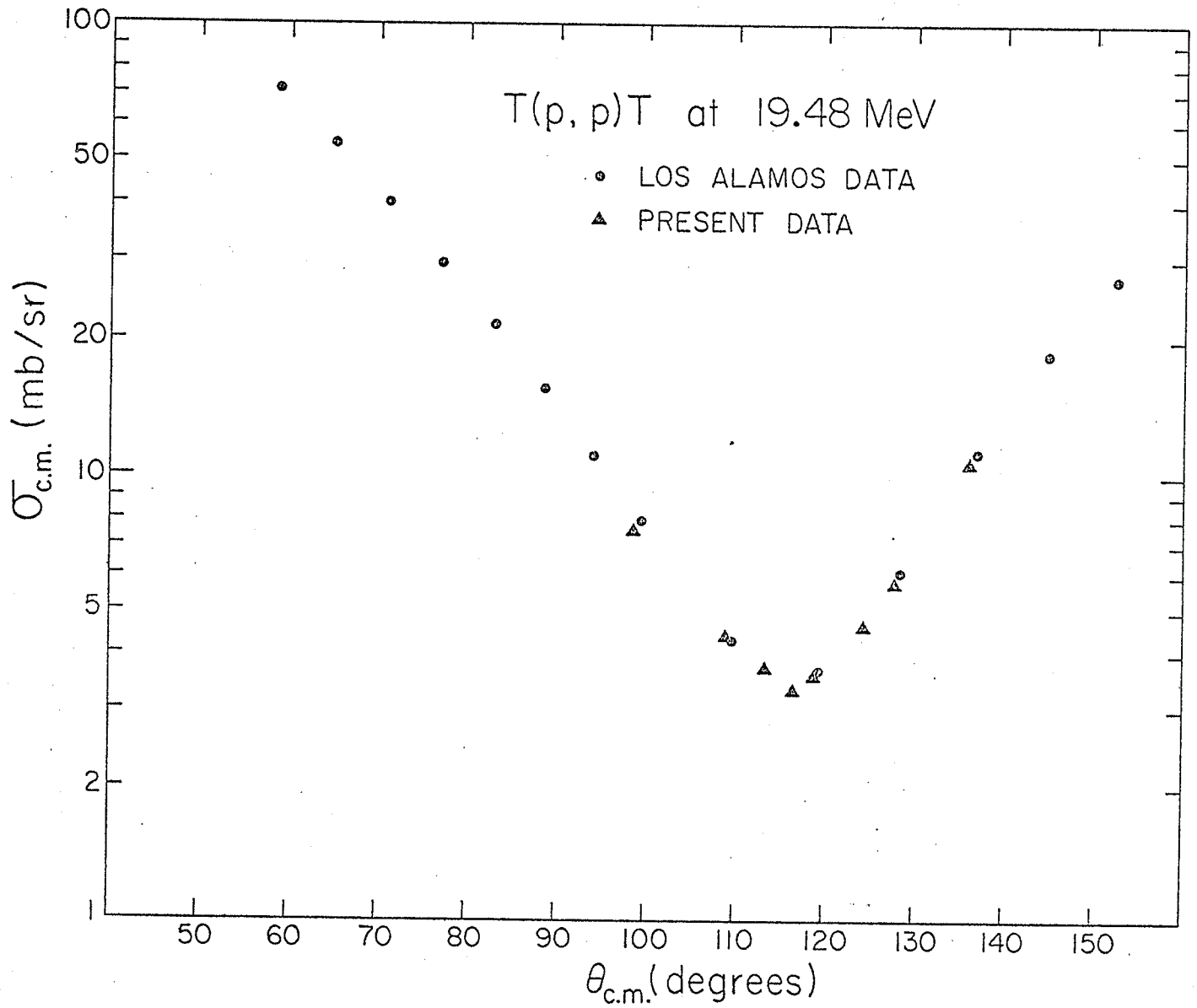

Fig. 5.1: Angular distributions for the T(p,p)T reaction. The present data (triangles) is normalized to the data of Detch et al.(circles)

somewhat uneven surface near the centre where the proton beam passed. If the tritium content is taken to be 8.05 curies, all the tritium coincidence cross sections presented in this thesis should be multiplied by a factor 7.60/8.05.

Table 5.2 summarizes the major sources of error contributing to the absolute uncertainty of the ^{3}He cross sections.

Table 5.2 Major sources of error contributing to the absolute uncertainty of the Helium-3 cross sections

Source	Percentage error
Pressure	~ 0.2
Temperature	~ 0.2
Impurities of the ^{3}He gas	~ 0.2
G-factor	~ 3.0
Dead time correction	$\lesssim 1.0$
Pile-up rejection correction	$\lesssim 1.0$
Loss of incident beam	$\lesssim 1.0$

The negligibly small errors associated with the pressure and temperature of the ^{3}He target gas resulted from the precision with which these quantities were measured. The purity of the ^{3}He gas quoted by the supplier had an uncertainty of $\sim 0.02\%$. Moreover, since the ^{3}He gas cell and feed lines were flushed many times before use and the gas pressure was maintained at slightly above one atmosphere, air contamination of the target was small. Three factors contribute to the error in the value of the G-factor. The first is inherent in the mathematical approach for the G-factor calculation. This error is small since results obtained by different approaches agree to better than 1% with one another (Ro69). No correction was made for the finite lateral extent of the beam but a detailed

calculation (Ro69) for a similar slit arrangement and beam profile showed that this correction was typically 0.5%. The second factor is associated with the error in the measurement of the collimator geometry and the uncertainty in the detector angles. With the present collimator geometry, a small change (0.1^{o}) in θ_3 and/or θ_4 produces a 0.5% change in the G-factor. The third and most significant factor arises from the drift in the lateral direction of the incident beam. A small drift in the beam from its central position can produce an appreciable change in the G-factor value; the effect being more severe at forward angle. However, periodic monitoring of the beam position showed no noticeable drift. It is estimated that this effect produces an uncertainty in the G-factor value of ~2%.

Although the major sources of absolute error have been described separately for the tritium and ^{3}He data, there remains one systematic error which is common to both. When monoenergetic protons, or other charged particles, are incident on a Si detector, the observed pulse height spectrum consists not only of a main peak but also of a 'tail' of reduced pulse height (Ma70b). The latter are due principally to events in which the incident particle undergoes a nuclear reaction (e.g. (p,p'), (p,α)) before it is stopped in the detector by ionization processes. For protons incident on Si detectors, the 'tail' represents ~0.2% of the total events at 13 MeV and ~1.4% at 28 MeV incident energies. The percentage 'tail' pulses increases as the energy of the incident particle increases. No correction has been made in the present data since correction of this kind in correlation spectra are rather difficult. However, even taking into account the Si detector response, the absolute cross section scales are better than 10% for the tritium data while they are better than 6% for the ^{3}He data. In both sets of data, the relative error is well represented by the statistical uncertainties.

6. RESULTS AND ANALYSIS

6.1 Quasifree scattering

Using the Plane Wave Impulse Approximation, the differential cross section for the (p,2p) and (p,pd) reactions under quasi-free scattering conditions can be written:

$$\frac{d^3\sigma}{d\Omega_3 d\Omega_4 dT_3} = KF \times \left(\frac{d\sigma}{d\Omega}\right)^{3-4}_{c.m.} \times N_F \times |\phi(\vec{q})|^2 \qquad (1)$$

The meaning of each of these quantities in this expression has been indicated in chapter 2. In the following sections, results will be presented of a comparison between the experimentally extracted momentum distributions and theoretical ones based upon simple wave functions. The experimental momentum distribution is given by

$$\frac{d^3\sigma}{d\Omega_3 d\Omega_4 dT_3} \Big/ KF \times \left(\frac{d\sigma}{d\Omega}\right)^{3-4}_{c.m.} \qquad (2)$$

where $\left(\frac{d\sigma}{d\Omega}\right)^{3-4}_{c.m.}$, strictly the square of an off-the-energy-shell scattering amplitude, is approximated by the on-the-energy-shell cross section. The latter being the experimental elastic scattering cross sections at the appropriate energy and scattering angle. For the (p,2p) reactions, values of $\left(\frac{d\sigma}{d\Omega}\right)^{pp}_{cm}(T)$ were found from a polynomial fit to MacGregor's tabulation (Ma66) of p-p elastic scattering differential cross sections data. The experimental data and the polynomial fit are shown in Fig.6.1.1 for $\Theta_{cm} = 90^{\circ}$.

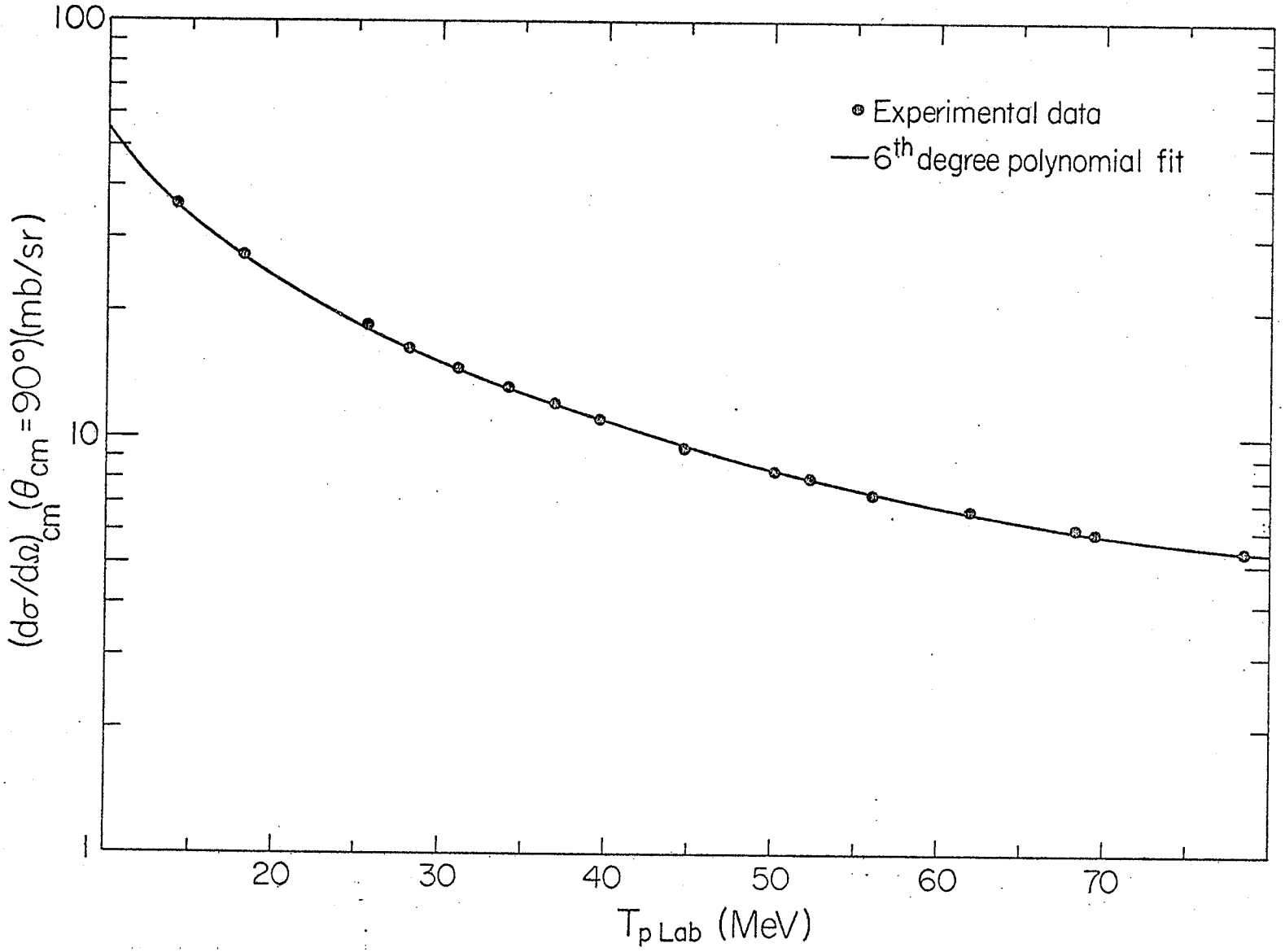

Fig. 6.1.1: Experimental p-p elastic scattering data from 10 to 80 MeV for $\theta_{cm} = 90^{o}$. Values are taken from reference (Ma66). Also shown is a sixth degree polynomial fit.

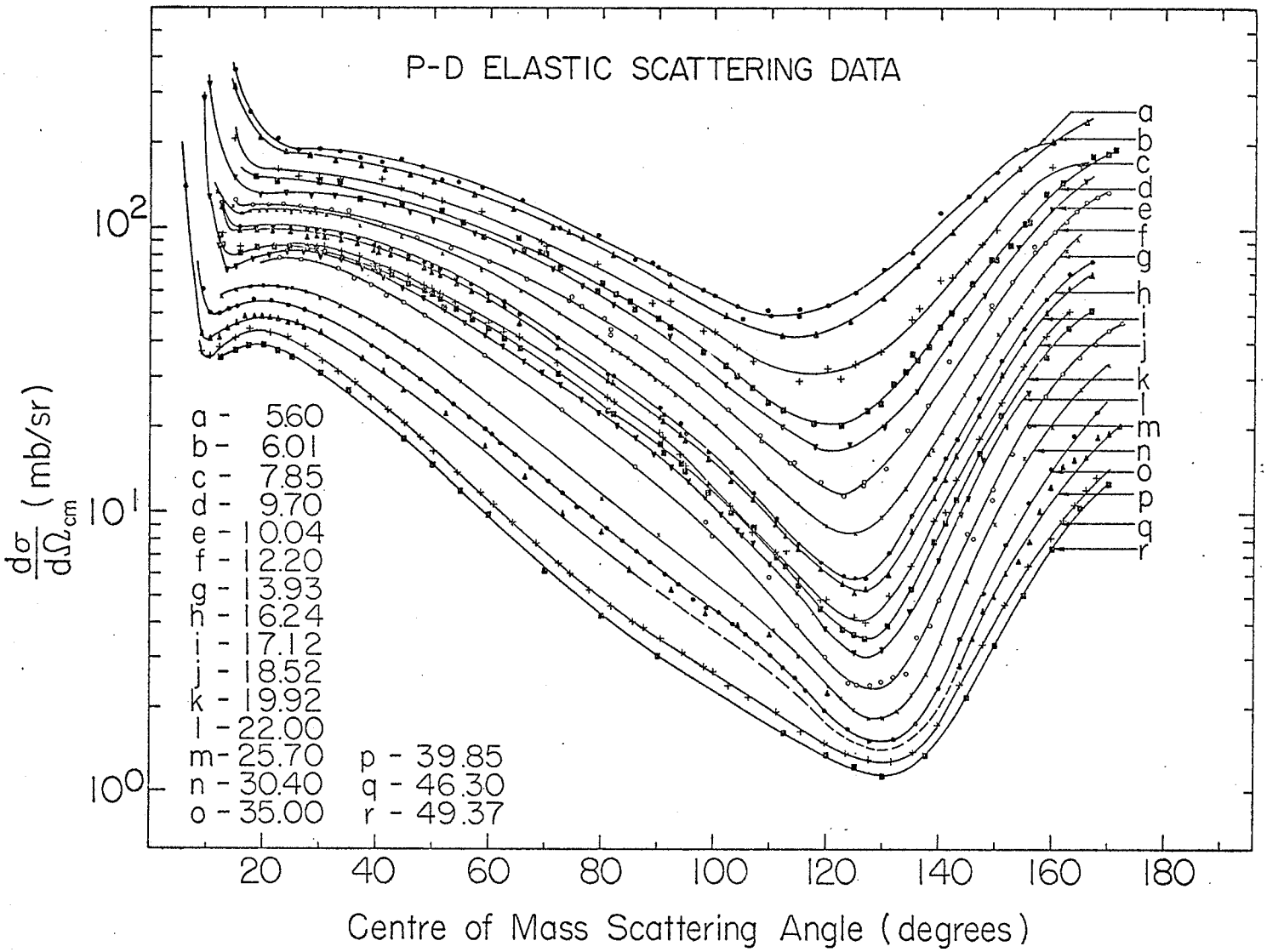

Fig. 6.1.2: Experimental p-d elastic scattering data for proton incident energies in the laboratory of 5.6 to 49.37 MeV. Values are taken from reference (Se70).

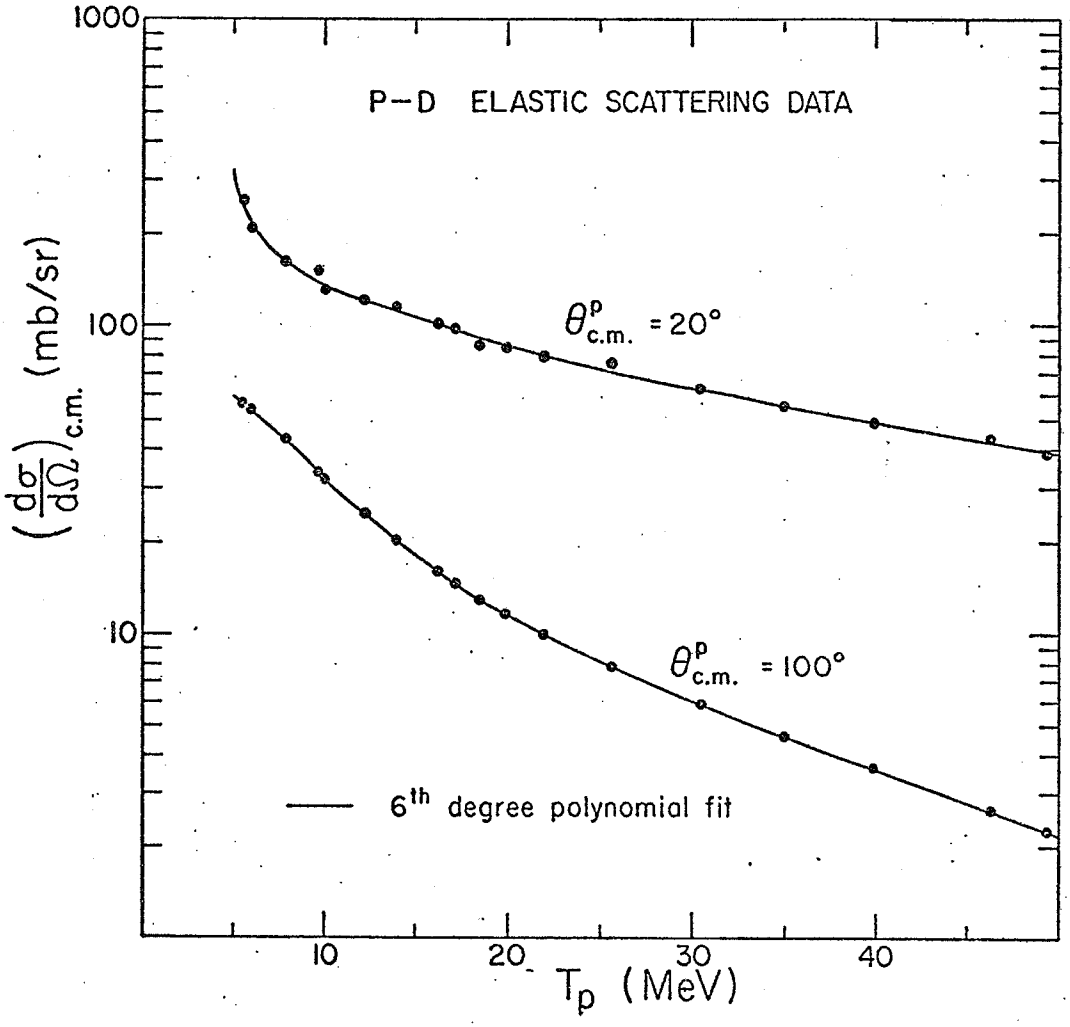

Fig.6.1.3: Polynomial fits to the experimental p-d elastic scattering differential cross sections in the energy range 5-50 MeV for proton centre of mass scattering angle 20° and 100°.

Since $\left(\frac{d\sigma}{d\Omega}\right)^{pp}_{cm}$ remains unchanged for centre of mass scattering angles between 50^{o} and 90^{o} at each particular energy, the polynomial fit to the 90^{o} differential cross section has been used throughout. For the (p,pd) reactions, values of $\left(\frac{d\sigma}{d\Omega}\right)^{pd}_{cm}(T,\theta)$ were obtained by interpolation of published differential cross section angular distributions. Fig.6.1.2 shows the p-d elastic scattering differential cross sections for proton incident energies (lab) between 5.6 MeV and 49.37 MeV and for centre of mass scattering angles between 10^{o} and 170^{o}. The data were taken from reference (Se70). Polynomial fits to $\left(\frac{d\sigma}{d\Omega}\right)^{pd}_{cm}(T)$ were obtained for different θ_{cm} (in steps of 5^{o} from 10^{o} to 170^{o}). Fig.6.1.3 shows samples of such fits. A linear interpolation could then be made to give $\left(\frac{d\sigma}{d\Omega}\right)^{pd}_{cm}(\theta_{cm})$ for any given energy.

For a given approximation, e.g. the final state energy prescription approximation, the relative energy and the centre of mass scattering angle of the two detected particles were calculated from the kinematics for each point on the projection. Cross sections appropriate to the particular values of T_{lab} and θ_{cm} were then calculated using the interpolation method described above.

6.1.1 Momentum distribution of [nn] in ^{3}H

Fig.6.1.4 shows the extracted [nn] momentum distributions in ^{3}H for the four approximations used for the off-the-energy-shell p-p scattering amplitude. It is evident that there are

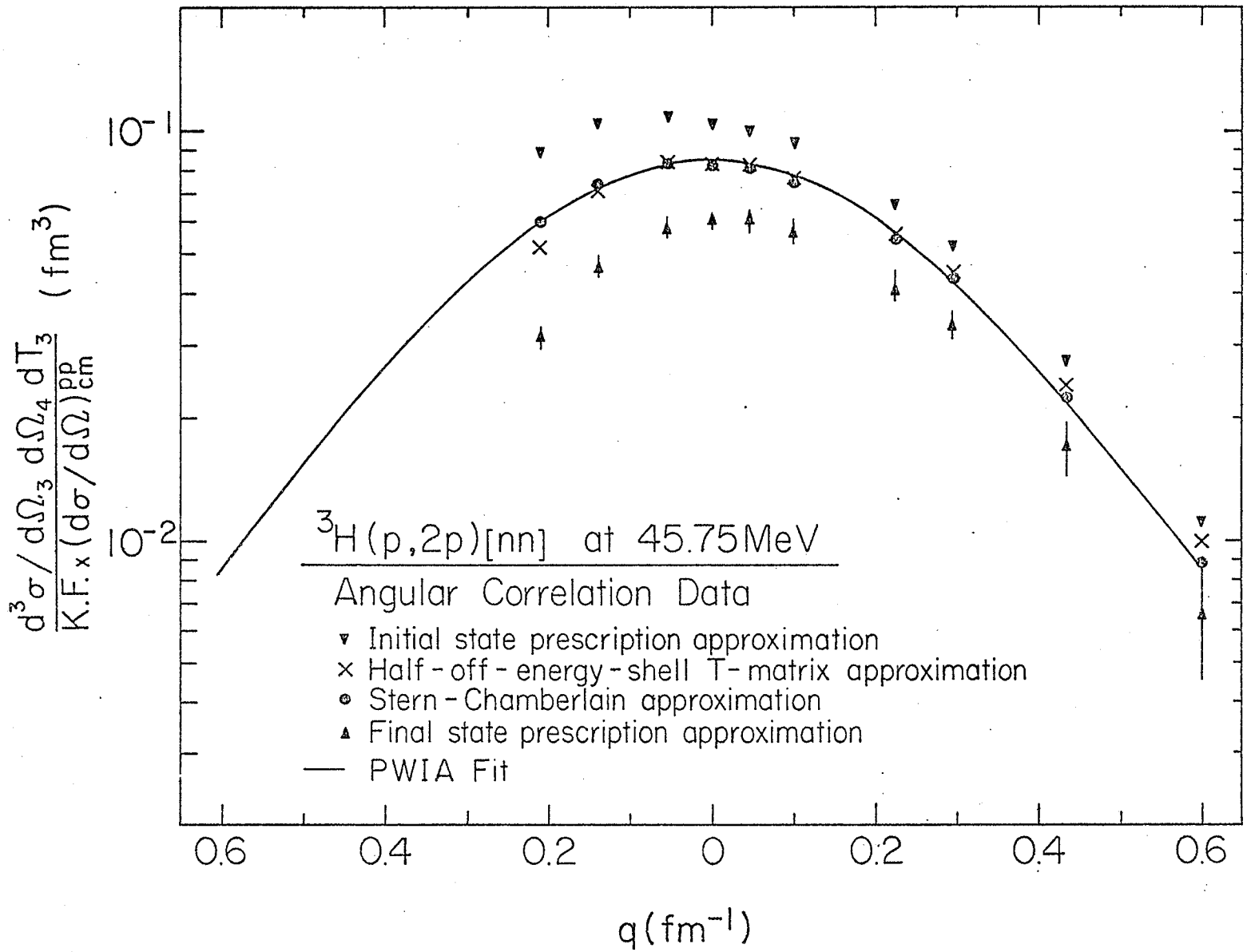

Fig. 6.1.4: Extracted momentum distributions for different approximations used for the off-the-energy-shell p-p interaction in the ^{3}H(p,2p)[nn] reaction.

significant differences in both the shape and magnitude. In particular, the initial state energy approximation gives results considerably different from those given by the final state energy approximation in regions of negative q. This is caused by the fact that in the final state energy approximation, $\left(\frac{d\sigma}{d\Omega}\right)^{pp}_{cm}$ is evaluated at a lower energy where the p-p cross section varies more rapidly with decreasing energy thus bringing down the distribution faster than the initial state energy approximation would. Closer examination reveals that the momentum distribution given by the final state energy approximation does not peak at q = 0 but is shifted by ~ 0.05 fm^{-1}. The Stern-Chamberlain approximation and the half-off-the-energy-shell T-matrix approximation produce closely similar momentum distributions which are symmetric about q = 0. The error bars on these data points have been omitted for clarity. They are typically of the same magnitude as those indicated for the final state energy approximation data.

The curve represents a theoretical momentum distribution, $|\Phi(\vec{q})|^2$, where $\Phi(\vec{q})$ is the Fourier transform of the overlap integral between the ^{3}H spatial wave function and the [nn] spatial wave function. The forms of the ^{3}H and [nn] spatial wave functions have been given in Table 2.1. No cut-off has been introduced in evaluating the Fourier transform. The theoretical momentum distribution has been normalized to the experimental data, extracted using the half-off-the-energy-shell T-matrix approximation for the p-p off-the-energy-shell scattering amplitude. It is clear that good fits can be obtained to the shapes of the experimental momentum distributions calculated using the Stern-

Chamberlain and half-off-the-energy-shell T-matrix approximations. An equally good fit may also be obtained to the final state energy approximation results if the theoretical distribution is shifted by ~ 0.05 fm^{-1} to positive q. The above results suggest the importance of the manner in which the p-p off-the-energy-shell interaction is taken into account.

Of all the approximations examined, the half-off-the-energy-shell T-matrix approximation is theoretically the most sound although the Stern-Chamberlain approximation produces similar results. In the latter approximation, $(d\sigma/d\Omega)^{pp}_{cm}$ is evaluated at an energy halfway between those defined by the initial state and final state energy approximations. Perhaps the most important result to be noted from these distributions is that they are consistent with an S-state for the relative motion of the proton and the [nn] system inside the ^3H nucleus.

Figures 6.1.5 and 6.1.6 show comparison between the angular correlation and the energy sharing data for each of the four approximations studied. Energy sharing data refer to data of a single angle pair while angular correlation data refer to data taken from many angle pairs (see Table 6.1). The energy sharing data under consideration is deduced from the QFS angle pair viz. 38^o- 38^o where q = 0 is kinematically allowed. Two interesting results are evident: 1) the shapes of the energy sharing distributions are very similar for all four approximations while those of the angular correlation differ significantly, 2) the angular correlation distributions are wider than the corresponding energy sharing distributions. In particular, in regions of large momentum transfers ($q > 0.4$ fm^{-1} to the right of 0), the angular

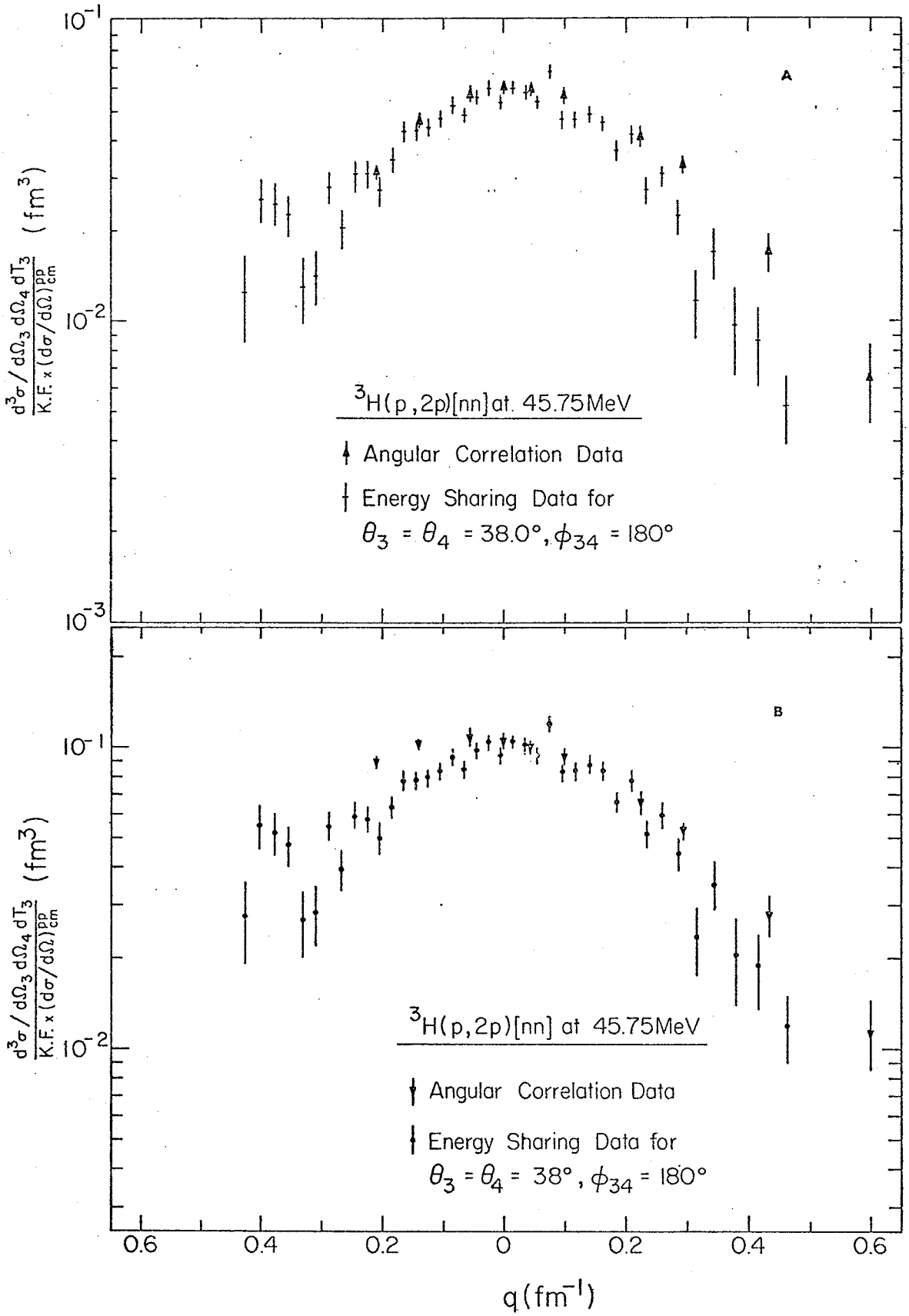

Fig.6.1.5: Comparison between angular correlation and energy sharing data for the ^{3}H(p,2p)[nn] reaction. Distributions A and B are obtained using the final and initial state energy approximations, respectively.

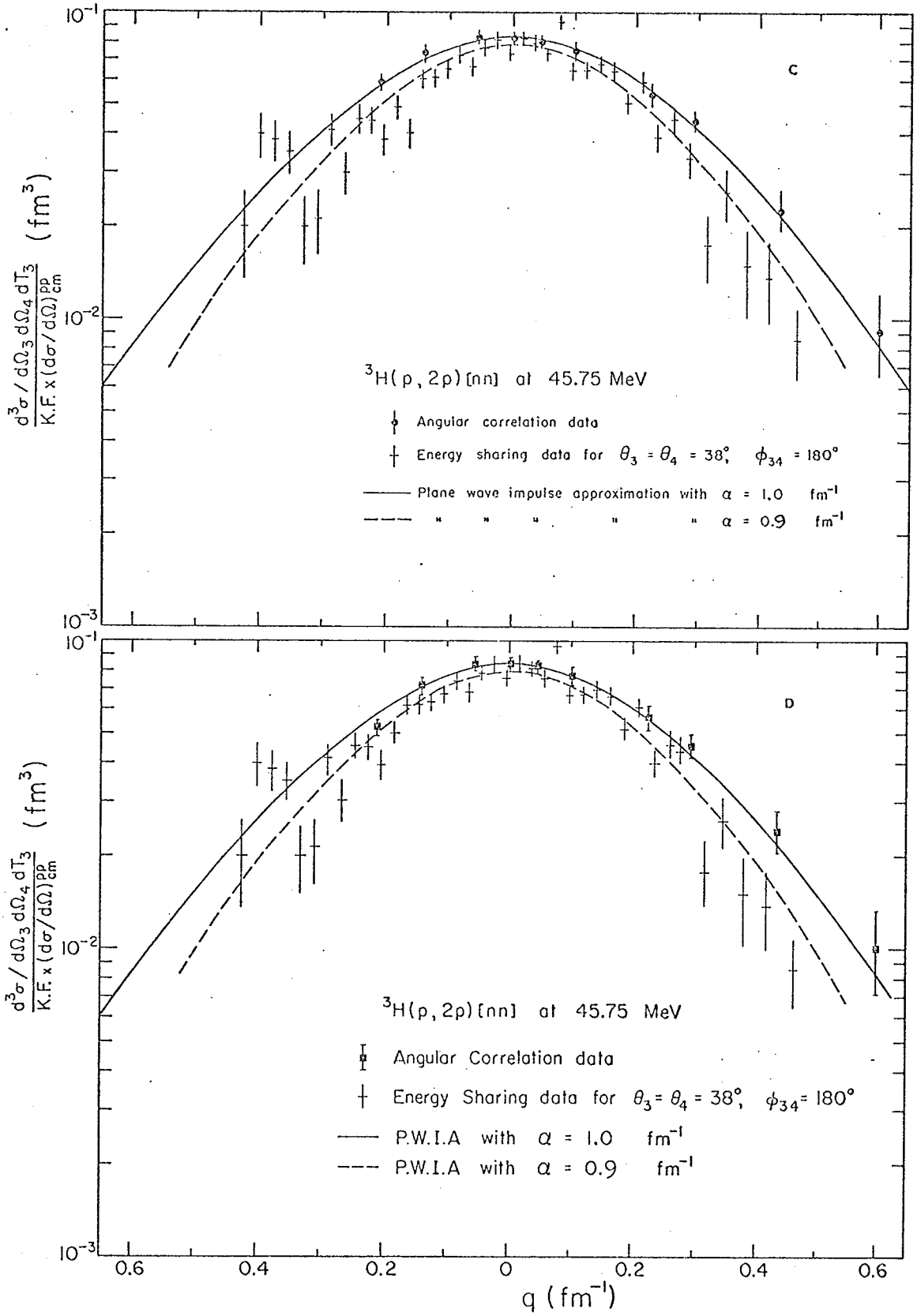

Fig.6.1.6: Comparison between angular correlation and energy sharing data for the ^{3}H(p,2p)[nn] reaction. Distributions C and D are obtained using the Stern-Chamberlain and half-off-the-energy-shell T-matrix approximations respectively.

correlations have values of $|\Phi(\vec{q})|^2$ consistently higher than those of the energy sharing data. This apparent break-down of the PWIA is not unexpected since in regions of large momentum transfers, the spectator pole is no longer dominant. Moreover, the kinematical situations corresponding to the same momentum transfer are vastly different for the angular correlation and energy sharing spectra (see Fig.6.1.7). Although it is not certain how these differences will manifest themselves in the two spectra, it is likely that distortion effects are more important in the energy sharing spectrum where one of the outgoing particles can have low energy. This suggests that the angular correlation spectrum provides a more reliable determination of the shape of the momentum distribution.

The energy sharing momentum distribution for each approximation can be fitted by the theoretical $|\Phi(\vec{q})|^2$ if $\alpha = 0.9$ fm^{-1} is used in the Irving-Gunn wave function. The two theoretical curves (solid and dashed) in Fig.6.1.6 do not coincide at q = 0 since the angular correlation data points were obtained by fitting the projected cross section (rather than the momentum distribution) of each angle pair with a Gaussian fitting routine. It is worthwhile noting from figures 6.1.6 and 6.1.8 that the shape of $|\Phi(\vec{q})|^2$ is sensitive to changes of the parameter α of the ^{3}H wave function but not to changes in the values of a_{nn} in the [nn] spatial wave function.

To investigate the angular dependence of p-p quasi-free scattering in the ^{3}H(p,2p)[nn] reaction, measurements were made

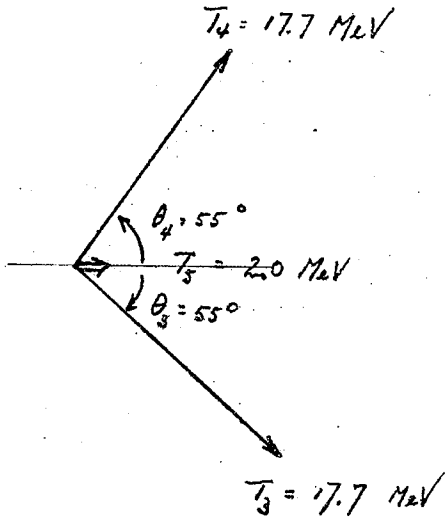

Angular Correlation Kinematics

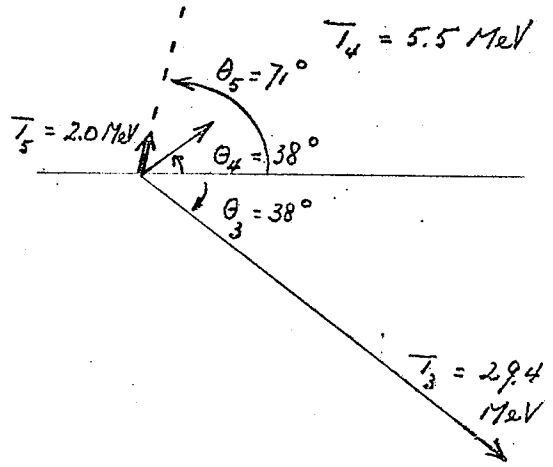

Energy Sharing Kinematics

Fig.6.1.7: Kinematical situations in the final state corresponding to q = 0.434 fm^{-1} for both the angular correlations and energy sharing spectra.

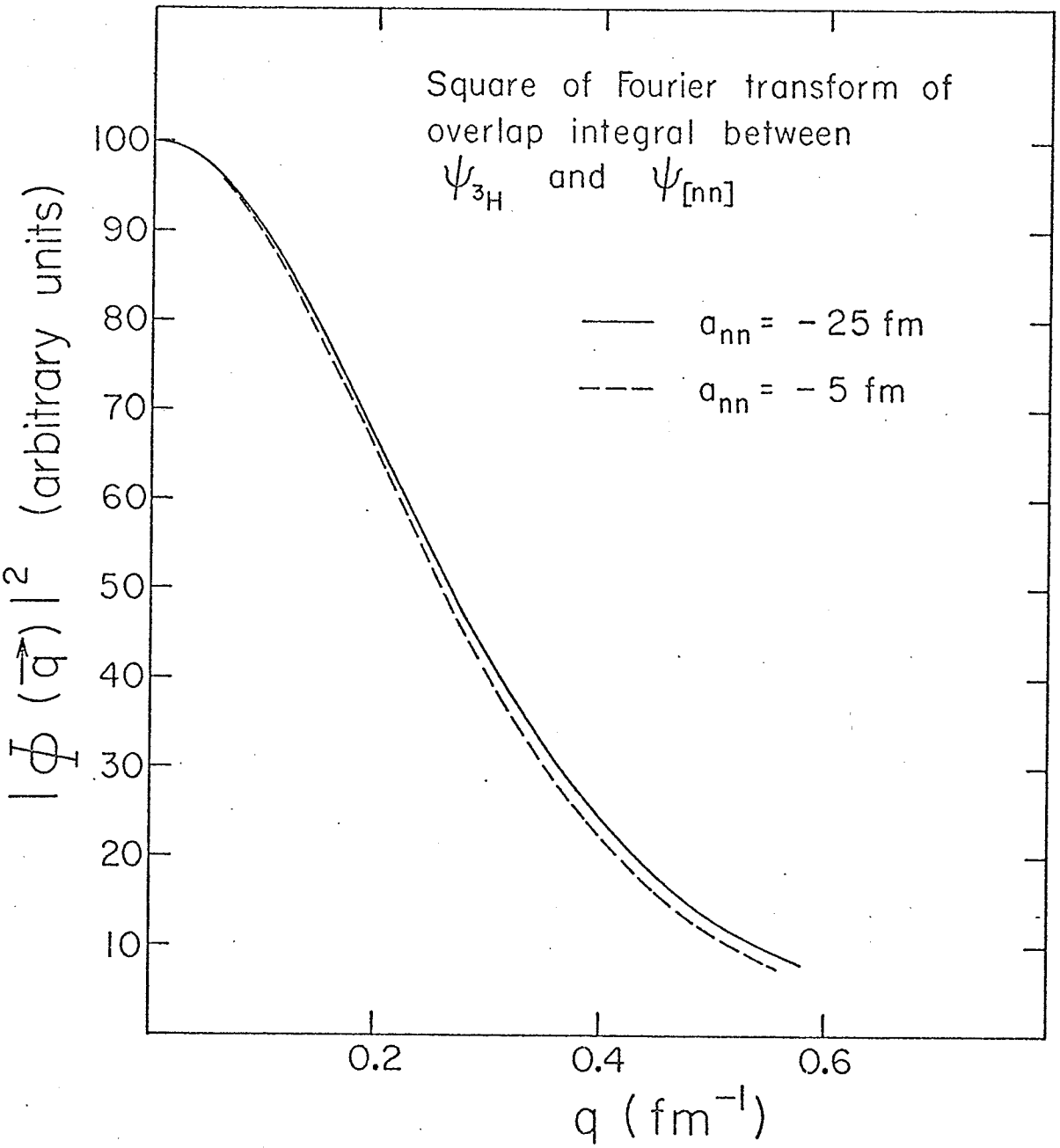

Fig.6.1.8: Graph showing the insensitivity of the shape of the theoretical $|\Phi(\vec{q})|^2$ to variations in the value of a_{nn} in the [nn] scattering wave function.

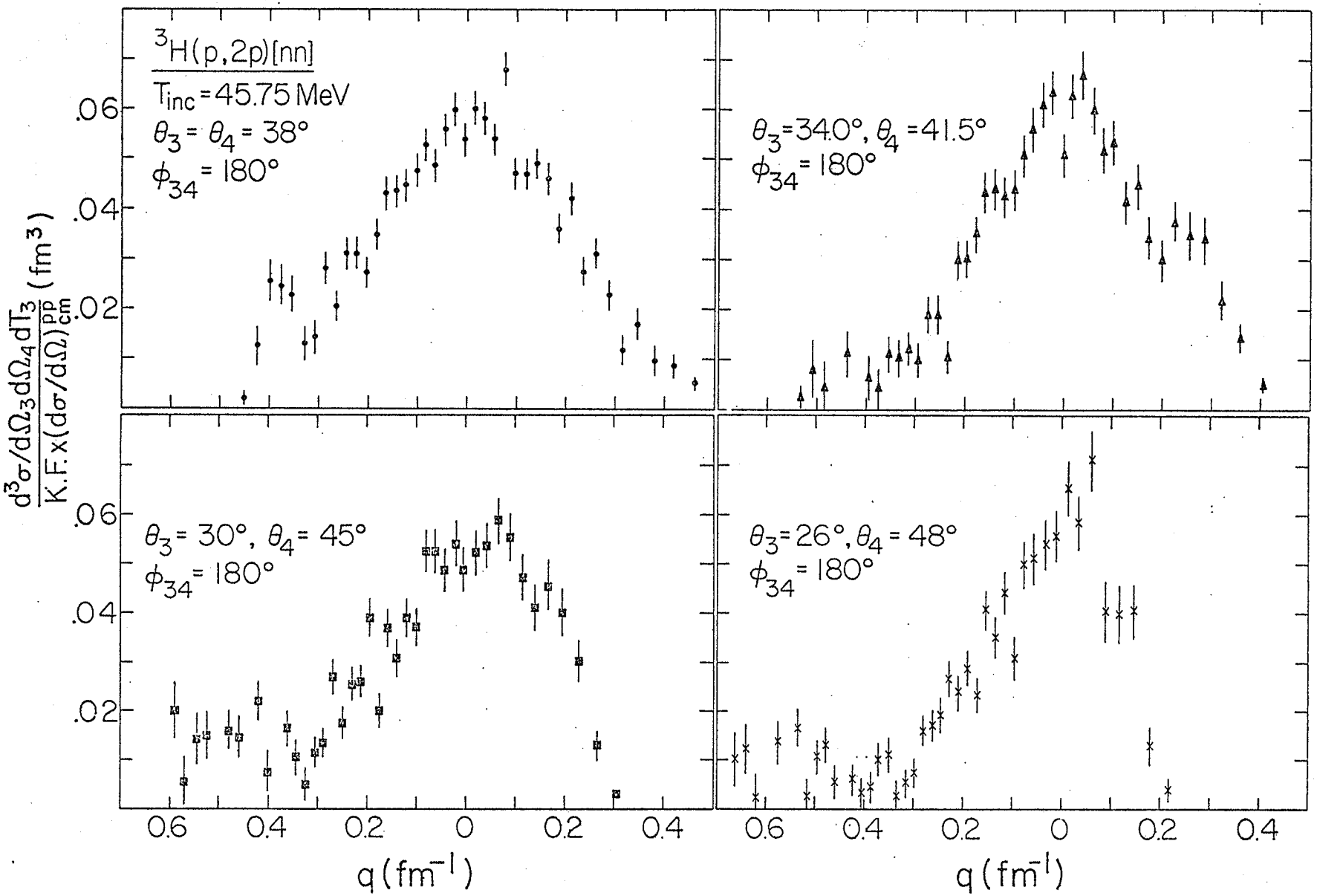

Fig. 6.1.9: Energy sharing momentum distributions for the ^{3}H(p,2p)[nn] reaction for different QFS angle pairs. The final state energy prescription has been used for evaluating $\left(\frac{d\sigma}{d\Omega}\right)^{pp}_{cm}$.

at four QFS angle pairs. These were 38°-38°, 34°-41.5°, 30°-45°, and 26°-48°. Fig.6.1.9 shows the extracted momentum distributions for these angle pairs using the final state energy approximation. It is evident that in each of the spectra, the QFS peak occurs at $q = 0$ and has a peak value of approximately 0.055 fm^3. The angle pairs chosen correspond respectively to centre of mass scattering angles of 90°, 80°, 70°, and 60.4° for the two outgoing protons in the final state. The results indicate that the peak cross section for QFS is only a function of the recoil momentum q and not of its direction $\hat{q}$. This is in accordance with the behavior predicted by the PWIA. However, recent studies of the (p,pn) knock out reaction on light nuclei (Ch73,Wa74) reveals that the p-n QFS is angle dependent for a fixed value of q. Cheng (Ch73), in a study of the D(p,pn)p reaction, attributed this anisotropy to the presence of the spectator particle and the difference in the p-p and n-p interactions. It will be interesting to see if the ^{3}H(p,pn)d reaction exhibits such an anisotropy.

6.1.2 Momentum distribution of d in ^{3}H

As already indicated, the projected energy spectra for the ^{3}H(p,pd)n reaction exhibit enhancements with peak positions shifted from those predicted by the PWIA. This effect is particularly noticeable for angle pairs away from the exact QFS condition. Figures 6.1.10 and 6.1.11 show the extracted momentum

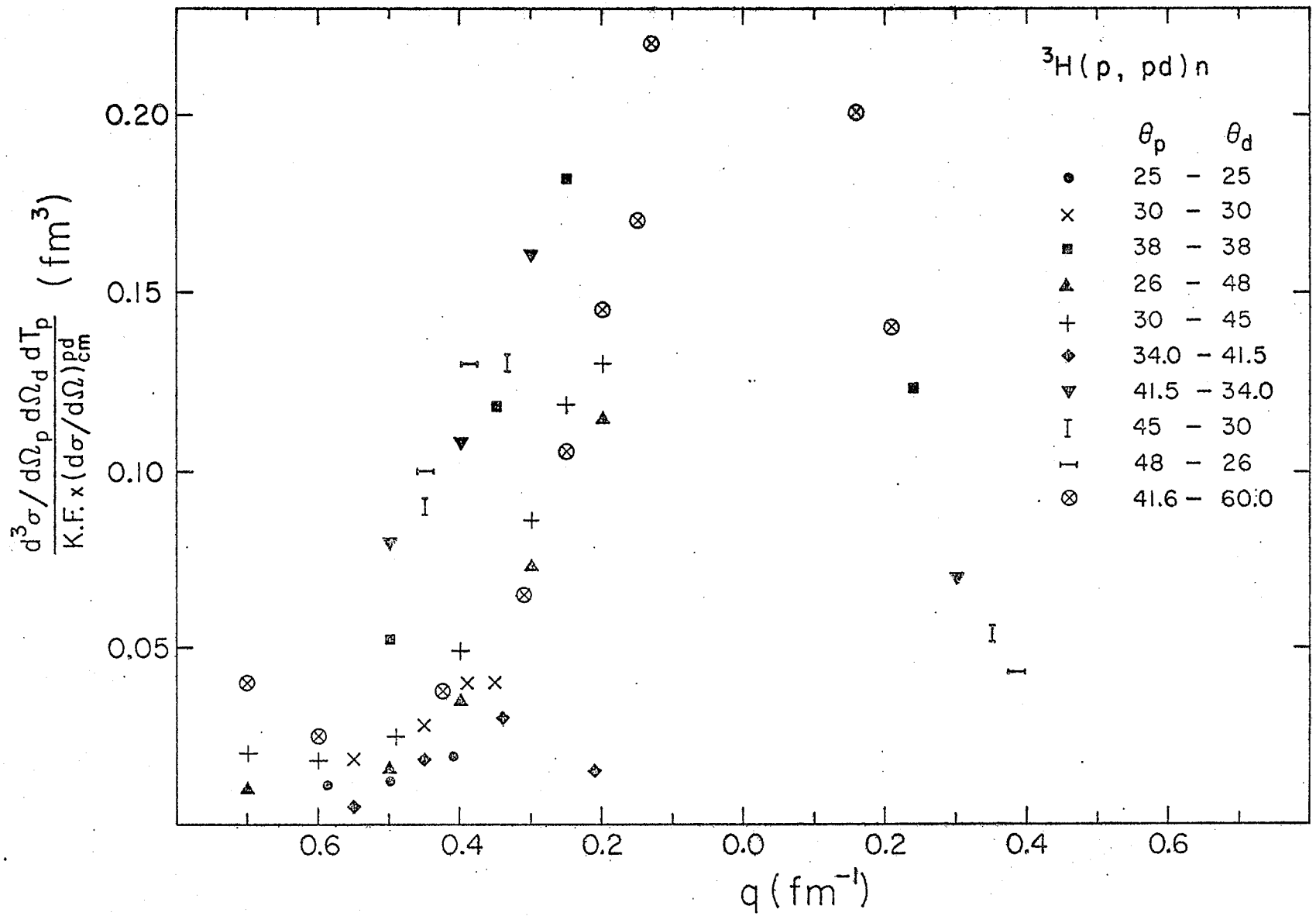

Fig. 6.1.10: Energy sharing momentum distributions for the ^{3}H(p,pd)n reaction at angle pairs which do not satisfy the QFS condition.

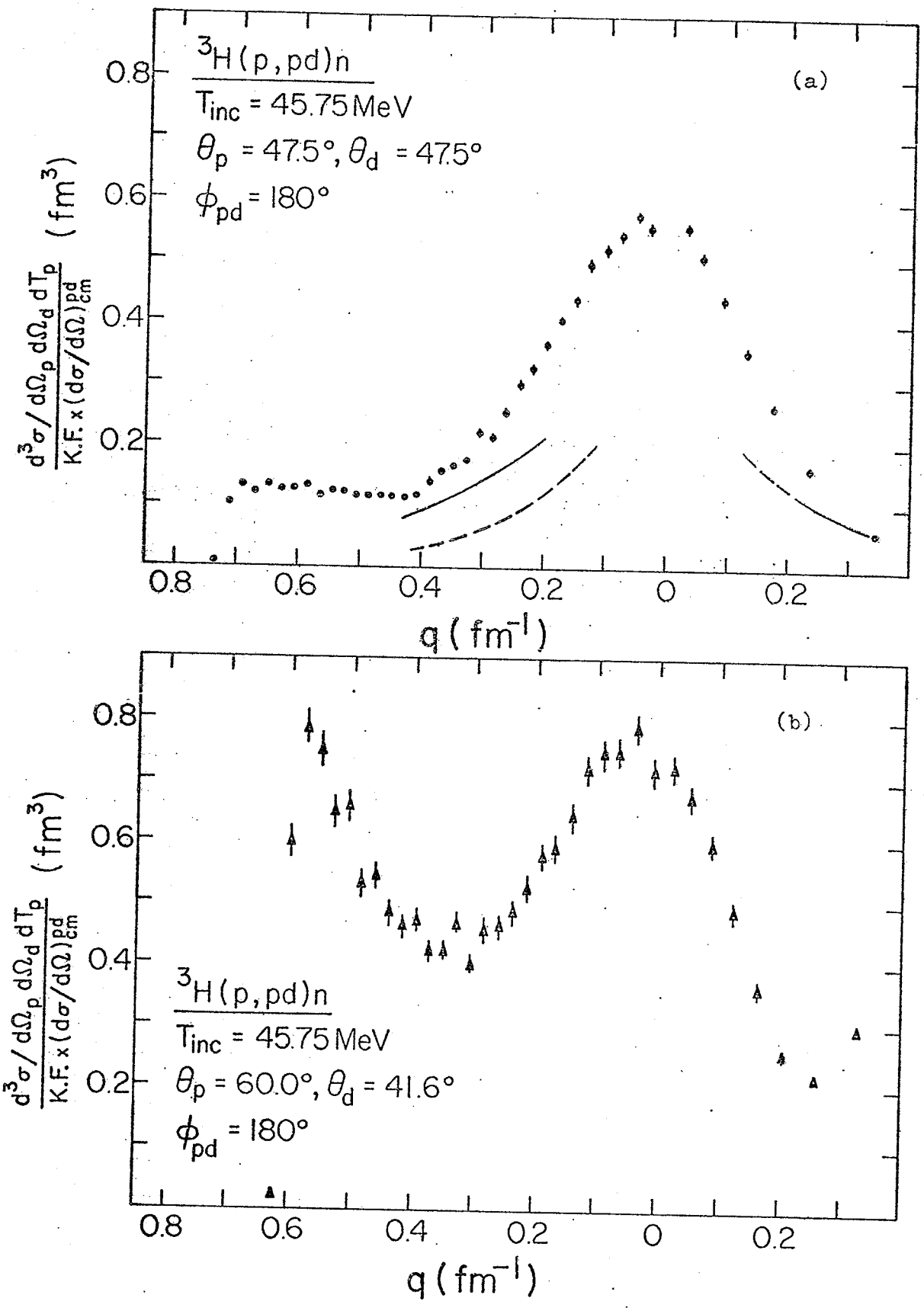

Fig.6.1.11: Energy sharing momentum distributions for the $^3H(p,pd)n$ reaction at symmetric (a) and asymmetric (b) quasi-free scattering angle pairs.

distributions for non-QFS angle pairs and QFS angle pairs, respectively. For clarity in Fig.6.1.10, only representative points are plotted for each angle pair. These points are further represented as lines in Fig.6.1.11(a). From those regions where a comparison can be made, it is apparent that the extracted momentum distributions for the non-QFS and QFS data differ significantly in both shape and magnitude. Moreover, for the non-QFS data, there appears a strong dependence on the angle at which the deuterons are detected. An examination based on kinematics shows that there is no simple correlation between this angular dependence and the angular distributions of the ^{3}He(p,d)pp reaction (assumed to be similar to ^{3}H(p,d)np) (see Fig.6.1.12). Nevertheless, Epstein et al.(Ep71) were able to show that the (l=0) neutron pick-up process indeed leads to a shift in the peak position.

Fig.6.1.11(b) shows the extracted momentum distribution for the angle pair $\theta_p = 60^\circ$, $\theta_d = 41.6^\circ$. It is obvious that the presence of a final state interaction between the proton and neutron, seen as an enhancement near q=0.6 fm^{-1}, appreciably alters the shape of the distribution. The only angle pair which seems to be free from competing processes is $\theta_p = \theta_d = 47.5^\circ$, although a slight shift ($\sim$ 0.03 fm^{-1} = 6 MeV/c) in the peak position is still apparent. This shift can be accounted for, however, by the experimental uncertainty in the energy calibration of the proton energy axis ($\sim$ $\pm$ 200 keV) and the fact that q_{min} at this angle pair goes only to 5.5 MeV/c and not zero.

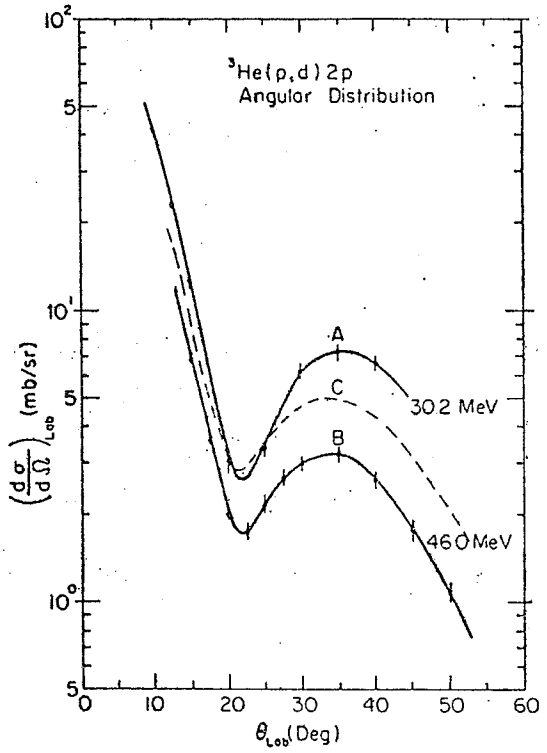

Fig.6.1.12: Angular distributions for the ^{3}He(p,d)2p reaction at proton incident energies 30.2 MeV and 46.0 MeV. Data are from reference (Ch69). The solid curves are obtained by integrating over a deuteron energy interval corresponding to T_{pp} = 0.4 MeV.

Similar shifts ($\sim$ 20 MeV/c) have also been observed at 65 MeV by the Maryland group (Co72) who investigated the ^{3}He(p,pd)p reaction at $\theta_p = 62.8^\circ$, $\theta_d = 41.8^\circ$, which satisfies the QFS condition. However, the shift in this case may be accounted for by a n-p final state interaction.

Fig.6.1.13 shows a comparison between the momentum distribution extracted from experiment and the normalized Fourier transform $|\Phi(\vec{q})|^2$, calculated using an Irving-Gunn wave function for ^{3}H and a Huthen wave function for the deuteron. The introduction of a cut-off radius of 4 fm is needed in order to be able to fit the shape of the data. Moreover, the curve for $|\Phi(\vec{q})|^2$ has been shifted by 0.03 fm^{-1} to positive q. Table 6.1 shows the ratio of the peak values.

Table 6.1

cut-off radius (fm)	$\left[\frac{d^3\sigma/d\Omega_p d\Omega_d dT_p}{KF \times (d\sigma/d\Omega)^{pd}_{cm}}\right] \Big/ \left(N_F^{**} \times \lvert\Phi(\vec{q})\rvert^2\right)$
0	0.166
4	0.725

** N_E is a factor due to spin and antisymmetrization

N_F = 1/2 for ^{3}He(p,2p)d*

= 1 for ^{3}H(p,2p)[nn]

= 3/2 for ^{3}H(p,pd)n and ^{3}He(p,2p)d

The quantity on the right of the table is generally known as the normalization constant.

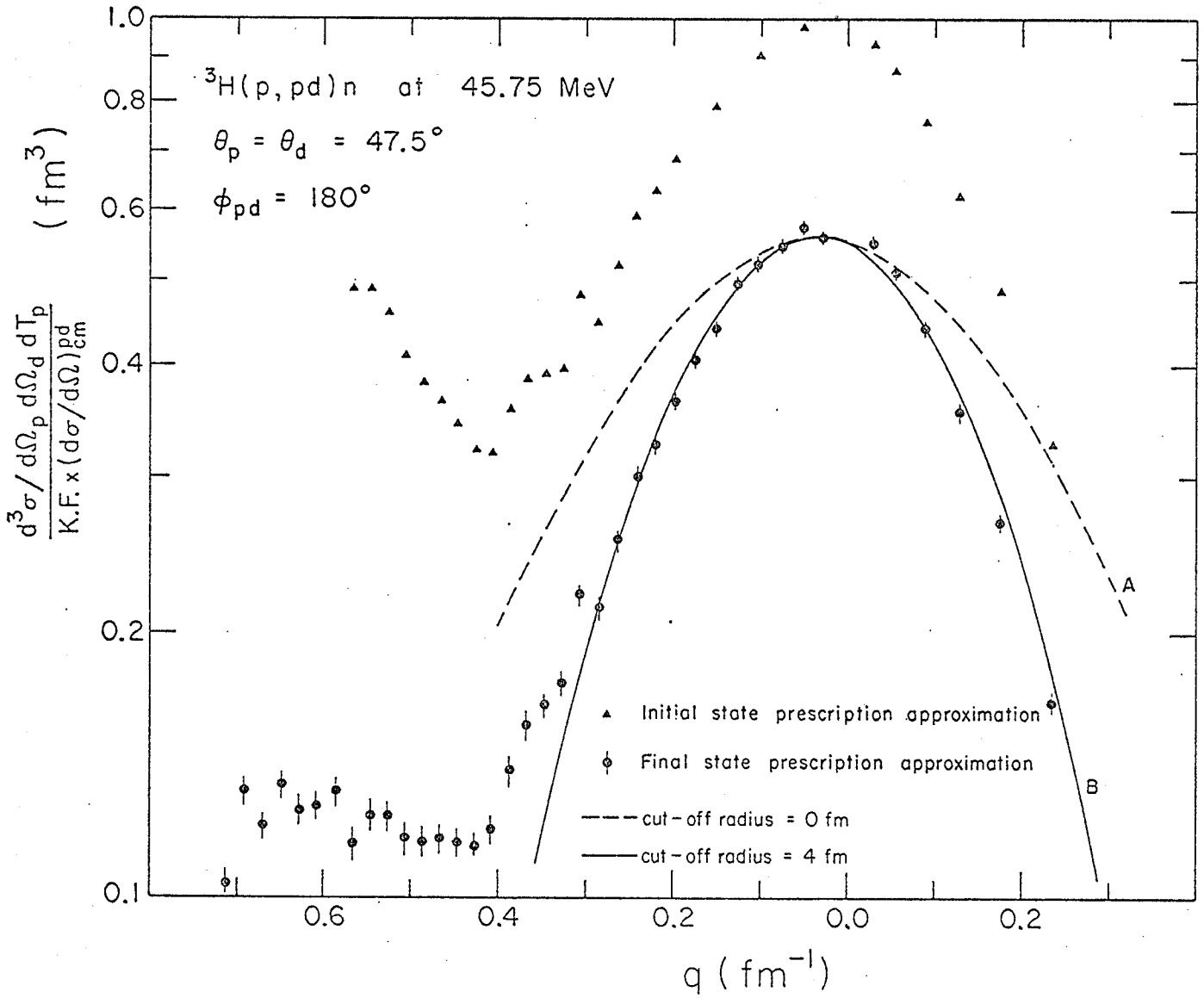

Fig. 6.1.13: Comparison between the experimental and theoretical momentum distributions for the ^{3}H(p,pd)n reaction at the symmetric QFS angle pair $\theta_p = \theta_d = 47.5°$, $\phi_{pd} = 180°$. Both theoretical curves are obtained using the Irving-Gunn wave function for ^{3}H with $\alpha = 1.0$ fm^{-1}.

It should be mentioned that the data presented in figures 6.1.10 and 6.1.11 were obtained using the final state energy approximation. A different set of normalization constants would have resulted if the initial state energy approximation had been used. However, it was evident from the ^{3}H(p,2p)[nn] reaction that the final state energy approximation gives a better fit to the angular correlation data and therefore should be the approximation to be used in the absence of a suitable half-off-the-energy-shell T-matrix for p-d scattering.

6.1.3 Momentum distribution of d and d* in ^{3}He

In a manner identical to the one described above, the momentum distributions of d and d* in ^{3}He have been extracted from the ^{3}He(p,2p)d and ^{3}He(p,2p)d* reactions respectively. The results for the deuteron momentum distribution are shown in Fig.6.1.14 for various approximations of the p-p off-the-energy-shell cross section and for different ^{3}He wave functions. Limiting the discussion to the momentum distribution extracted using the final state energy approximation, it is evident that the theoretical momentum distribution is somewhat broader than the experimental one. A cut-off radius of 2.5 fm is required in order to fit the experimental result. The corresponding normalization constant is 0.254. The small shift (< 5 MeV/c) seen in the data is well within the experimental uncertainties.

The ^{3}He(p,2p)d* results are presented in Fig.6.1.15. The theoretical momentum distribution has been obtained from the overlap of an Irving-Gunn wave function for ^{3}He ($\alpha = 0.77$ fm^{-1}) and a scattering wave function for d* (see Table 2.1). No cut-off was introduced. However, since the data flatten out at about the half-value, it is difficult to

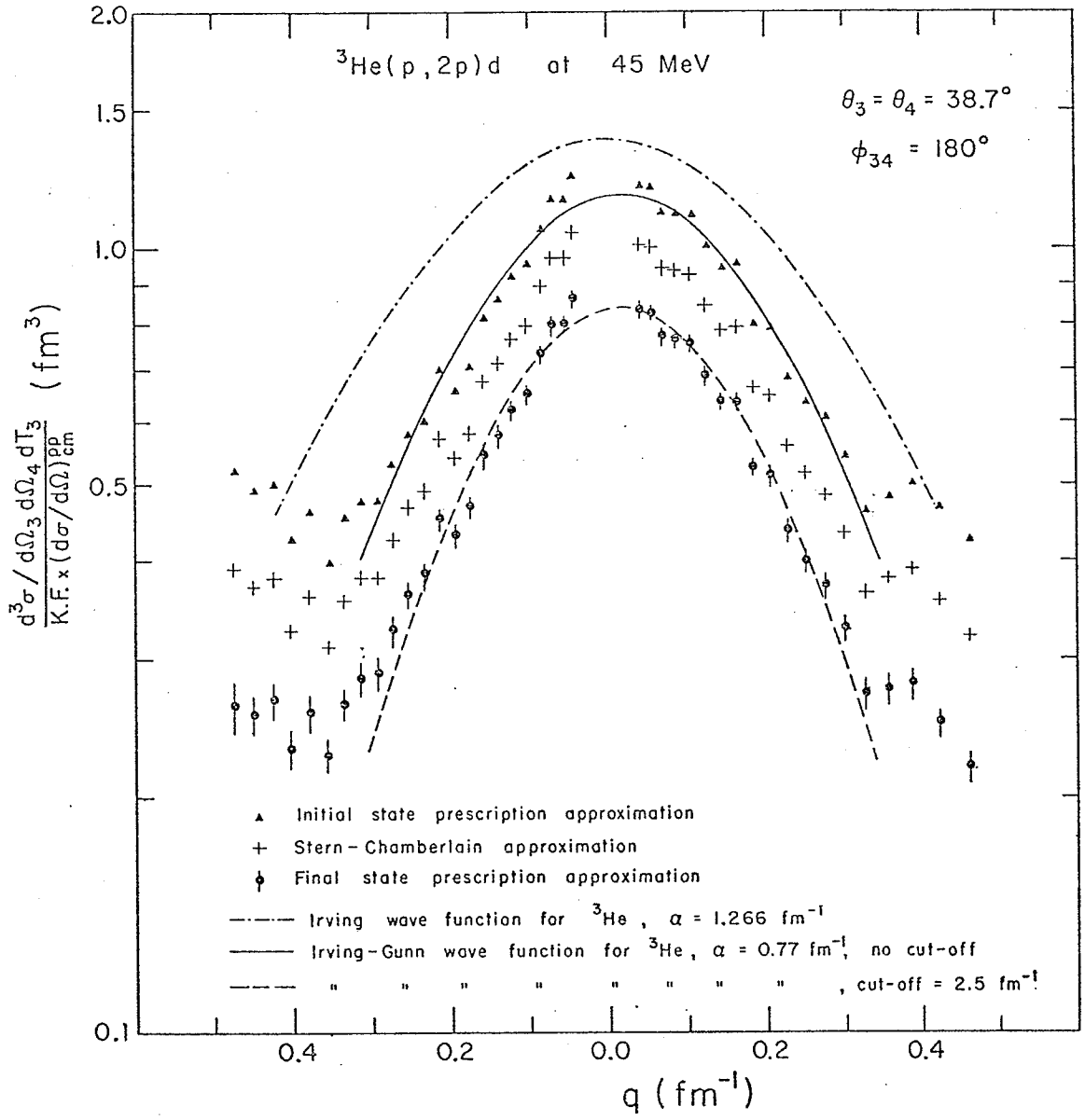

Fig.6.1.14: Comparison of the experimental and theoretical momentum distributions for the ^{3}He(p,2p)d reaction.

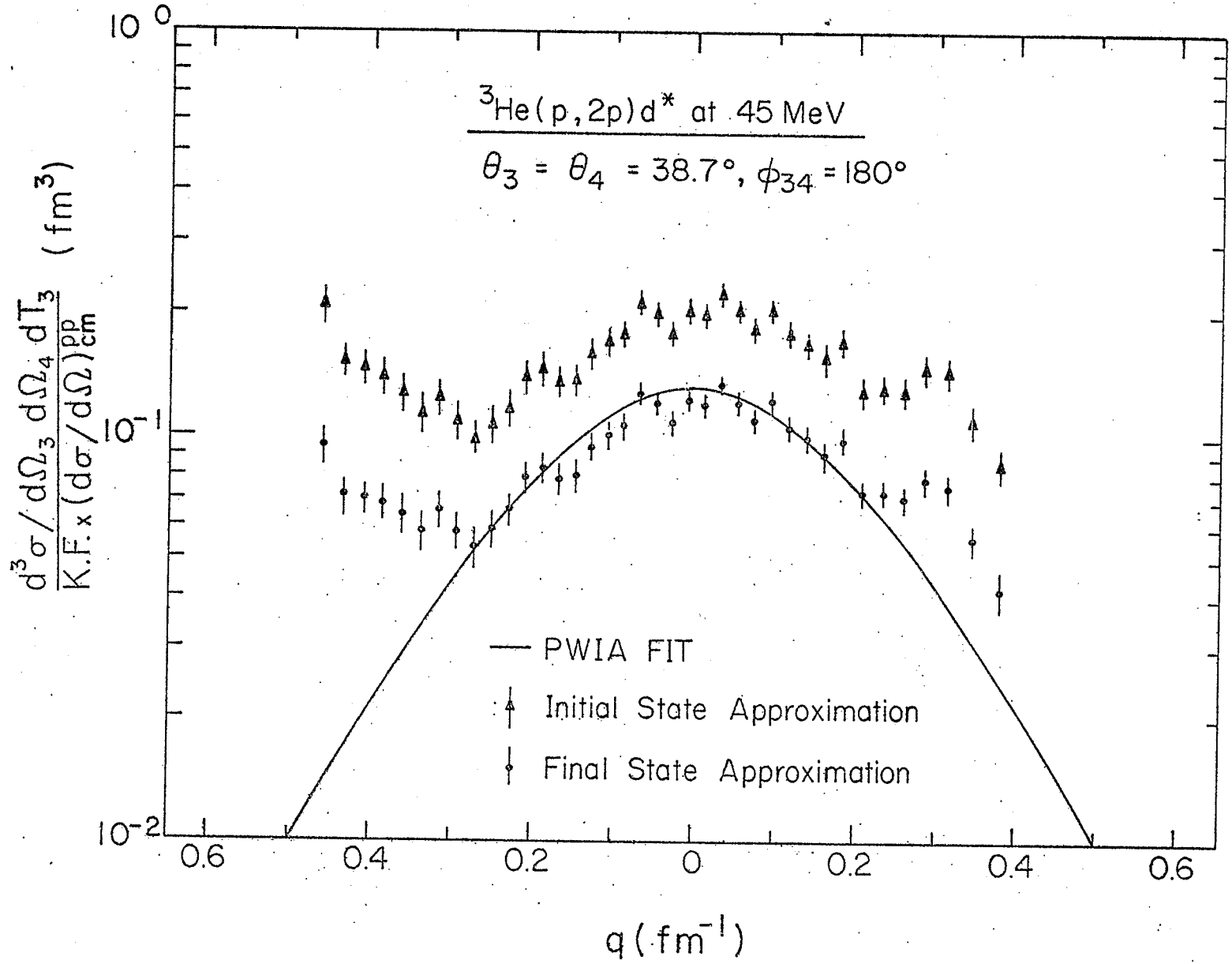

Fig. 6.1.15: Comparison of the experimental and theoretical momentum distributions for the ^{3}He(p,2p)d* reaction.

make meaningful comments about the width of the d* momentum distribution in ^{3}He and consequently about the theoretical fits.

A comparison of the ^{3}He(p,2p)d and ^{3}He(p,2p)d* data shows that the ratio of the peak cross section is ~7 in favor of the ^{3}He(p,2p)d reaction. This is in agreement with the data of Jain et al (Ja74). The same ratio was estimated to be ~ 10 at 35 MeV (S171) and ~6 at 155 MeV (Fr71). In all cases, the d* represents a n-p pair with relative energy from 0 to ~2 MeV (taking into account the experimental resolution). The results indicate that the observed ratio decreases with increasing incident energy. It will therefore be of interest to determine this ratio at a higher energy (e.g. 500 MeV) although the experimental resolution required to separate the three-body from the four-body events is considerably more difficult at this high energy.

A few conclusions can be reached from the above studies:

1) The shapes of the momentum distributions extracted from experiments are essentially the same (0.45 fm^{-1} FWHM) for the reactions ^{3}H(p,pd)n and ^{3}He(p,2p)d but the one for the ^{3}H(p,2p)[nn] reaction is significantly wider (0.55 fm^{-1} FWHM).

2) Theoretical distributions $|\phi(\vec{q})|^2$ derived from the overlap of an Irving-Gunn trion wave function with a two-nucleon wave function fit the shape of the experimental angular correlation distributions for the ^{3}H(p,2p)[nn] reaction but are too wide for the energy-sharing distributions for the ^{3}H(p,pd)n and ^{3}He(p,2p)d reactions. Although the introduction of a cut-off radius brings about agreement in the shape in the latter two cases (4.0 fm for ^{3}H(p,pd)n and 2.5 fm for

^{3}He(p,2p)d), the large values of the cut-off radius makes this procedure physically not too meaningful (the rms radius of the tri-nucleon is ~ 2 fm).

3) Where comparisons can be made on the magnitude of the cross sections , the PWIA calculations are a factor of a few larger than the experimental values. It is unlikely that discrepancies of the magnitude observed can be the result of inadequate wave functions particularly since the same wave functions were found to give reasonable agreement for the ^{3}He(p,2p)d reaction at 156 MeV. Thus, the failure of the PWIA indicates significant contributions from multiple scattering at 45 MeV and general inadequacy of the reaction theory.

6.2 Nucleon-nucleon final state interactions

The reactions ^{3}He(p,2p)pn, ^{3}H(p,2p)nn, and ^{3}H(p,pd)n can under proper kinematic conditions show enhancements due to a final state interaction between two nucleons. One possibility for the first two reactions is for the spectator pair to have a low energy for the relative motion. At the spectator angle pair, the spectator pair has zero total laboratory momentum and a zero energy for the relative motion (see Fig.2.1.3). This is evidently not the best condition for studying FSI because of the presence of the dominant QFS process. However, an anlysis by means of the Watson-Migdal model should indicate the relative importance of a final state interaction between the spectator pair of nucleons in the ^{3}He(p,2p)pn and ^{3}H(p,2p)nn reactions under quasifree scattering kinematical conditions.

For the ^{3}H(p,pd)n reaction, it is relatively easy to choose kinematic conditions such that the outgoing proton and neutron have a low relative energy. A FSI between this pair of particles will manifest itself as an enhancement along the locus of kinematically allowed events where T_{pn} is a minimum. The interest in applying the W-M model to this reaction is that recent studies (Ba66) of the reactions ^{2}H(^{3}He,t)2p and ^{1}H(^{3}He,d)2p show that the W-M model fails in both cases. The reason for the first reaction is that the emitted triton often carries off information on a np rather than a pp pair. The primary interaction mechanism in this case is unsuitable for direct application of the model because of

interference effects (He67b). The second reaction fails because of the diffuseness of the outgoing deuteron. As the deuteron has no sharp boundary, it is possible that a well-defined pole in momentum transfer does not exist and unambiguous application of the model becomes impossible. It is therefore of interest to test this model on the ^{3}H(p,pd)n reaction in which the deuteron is one of the outgoing detected particles.

6.2.1 Missing mass spectra for the ^{3}H(p,2p)nn and ^{3}He(p,2p)pn reactions

Since M_{56} is a direct measure of the relative energy of the spectator pair ($T_{56} = M_{56} - m_5 - m_6$), the Watson-Migdal model may be applied directly to the M_{56} spectra. Fig.6.2.1 shows the missing mass spectra for the ^{3}H(p,2p)nn and ^{3}He(p,2p)pn reactions at their respective spectator angle pairs.

In the tritium spectrum, the two peaks to the left correspond to the ^{2}H(p,2p)n and ^{3}He(p,2p)d contaminant reactions. In the ^{3}He spectrum, the pronounced peak on the left corresponds to the ^{3}He(p,2p)d reaction. The relatively poor separation between the ^{3}He(p,2p)d three-body locus and the boundary of the four-body continuum is still not fully understood. This in unlikely to be due to deuteron leak-through since particle identification for this angle pair was excellent. One possible explanation for the filling-in of this valley is that of slit-edge scattering from protons belonging to the ^{3}He(p,2p)d reaction. These protons,

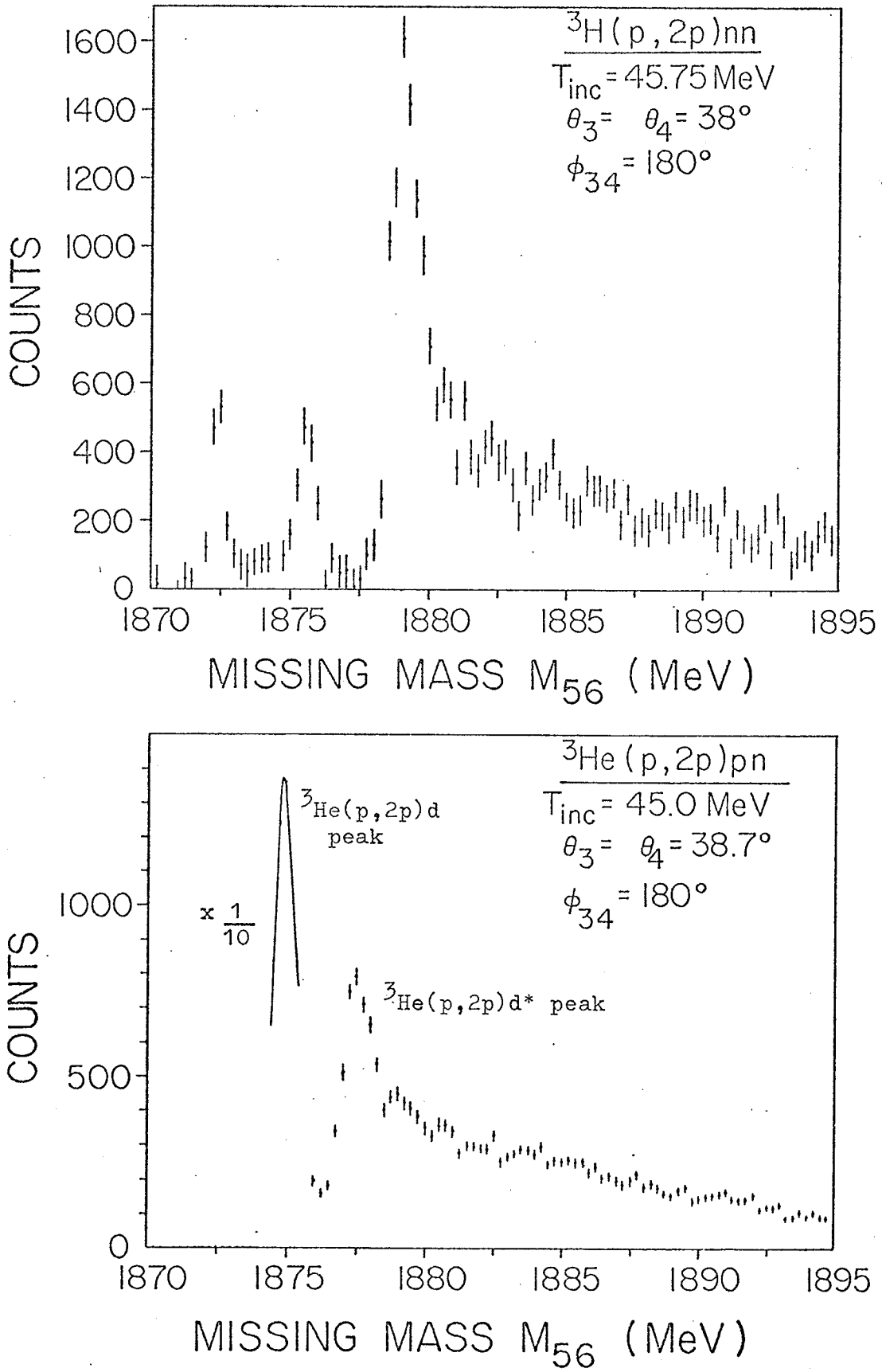

Fig.6.2.1: Missing mass spectra for the ^{3}H(p,2p)nn and ^{3}He(p,2p)pn reactions at their respective spectator angles.

after suffering a scattering from the edges of the collimator slits will have a lower energy and hence a correspondingly lower M_{56}.

Figures 6.2.2 and 6.2.3 show Watson-Migdal fits to the ^3H and ^3He missing mass spectra respectively. Only the range of M_{56} corresponding to T_{56} between 0 MeV and 5 MeV was used for fitting since the W-M model is valid only for small values of T_{56}. The curves represent the following expression (Eq.2.23)

$$d\sigma \sim R_4(\vec{P}, E)(F_s + W_t F_t) \qquad (3)$$

The four-body phase space factor is obtained by numerically summing the differential distribution $dR_4/(dT_3 d\Omega_3 dT_4 d\Omega_4)$ over constant bins of M_{56}. The resultant phase space distribution in M_{56} $dR_4/(d\Omega_3 d\Omega_4 dM_{56})$ is smooth as long as the bins for M_{56} (equivalently bins for T_3 and T_4) are sufficiently small($\Delta T \sim 0.1$MeV). In each case, a Gaussian resolution function (see Appendix III) has been folded in to the expression given above. Guassian widths (FWHM) of 0.6 MeV and 0.5 MeV were used for the ^3H and ^3He spectra respectively. For the ^3H spectrum, the width of the Gaussian was determined experimentally from p-p coincidence spectra using a hydrogen target (CH_2) of the same thickness. For the ^3He spectrum, the width was taken to be the FWHM of the $^3He(p,2p)d$ peak. The low energy scattering parameters used for the fit are summarized in Table 6.2

It is apparent that no fit can be obtained for reasonable

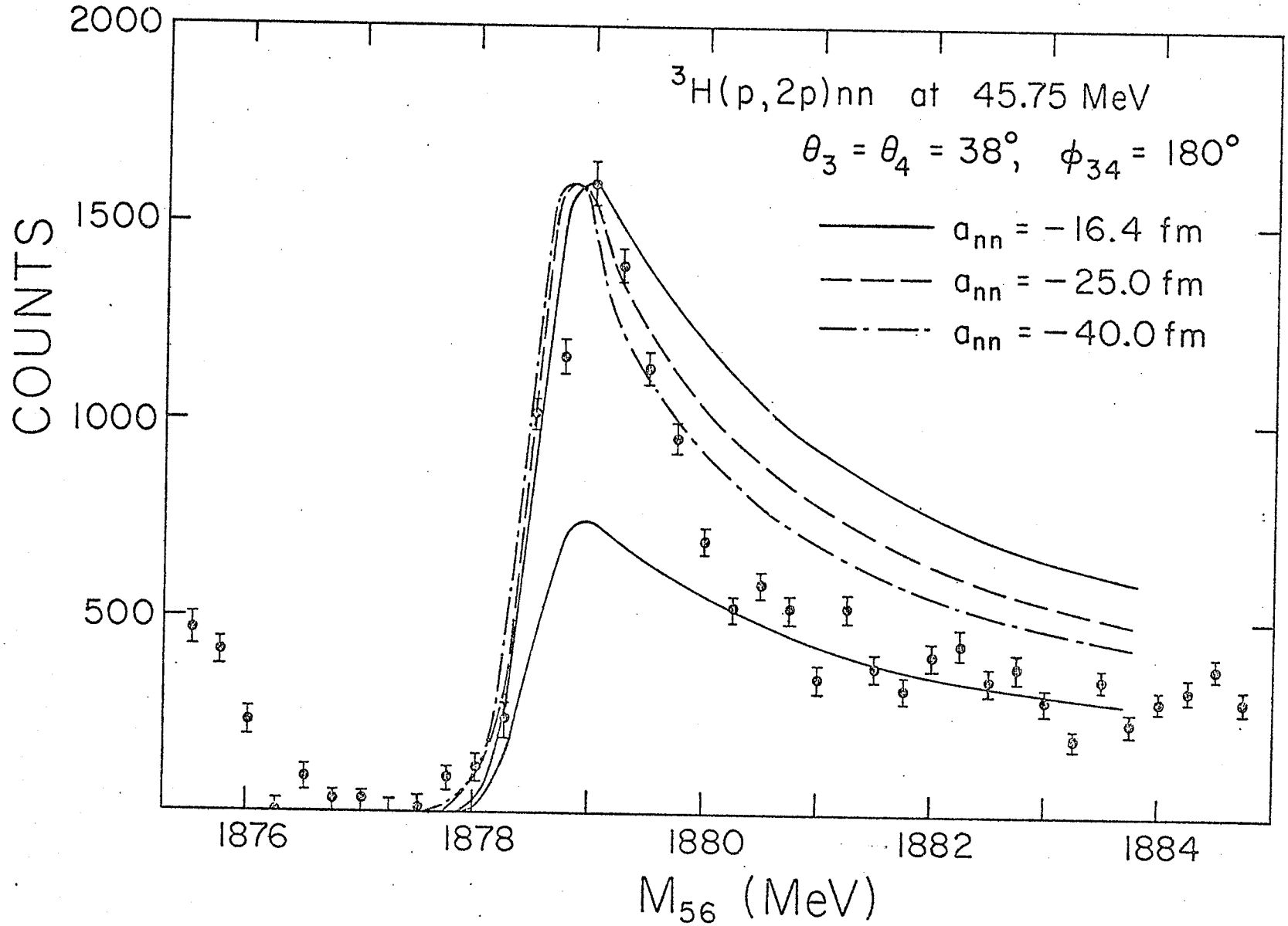

Fig. 6.2.2: Comparison of the ^{3}H(p,2p)nn missing mass data with the Watson-Migdal predictions for different scattering lengths. The upper three curves are normalized to the peak while the bottom one is normalized to the tail.

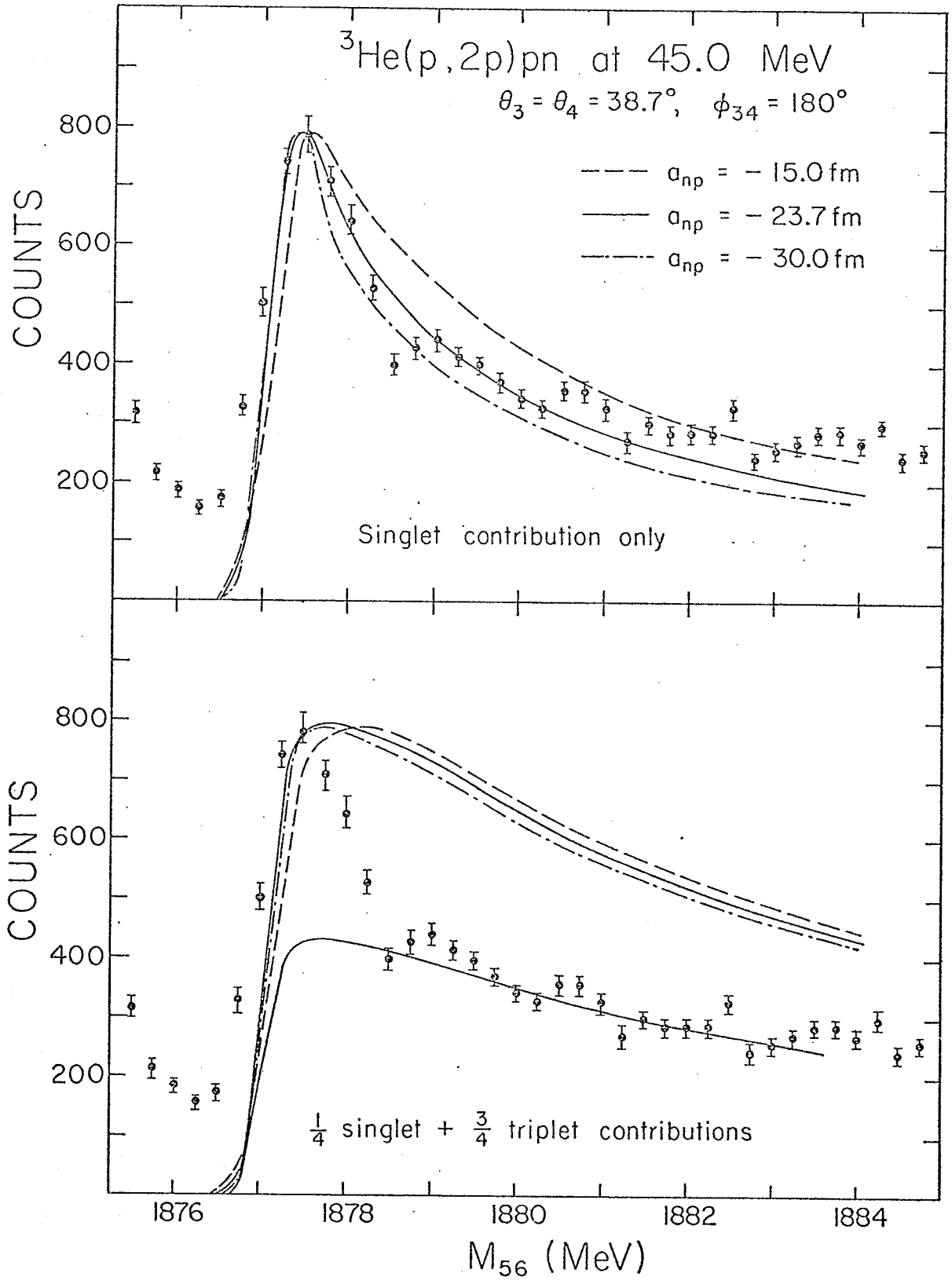

Fig.6.2.3: Comparison of the ^{3}He(p,2p)pn missing mass data with the Watson-Migdal predictions for different scattering lengths and different contributions of triplet n-p FSI.

Table 6.2

Low energy N-N scattering parameters used as inputs to the Watson-Migdal enhancement factor (Da68)

	a (fm)	r_o(fm)
singlet n-p	-23.715	2.758
triplet n-p	5.426	1.732
singlet n-n	-16.4	2.7

values of the scattering lengths for either the tritium spectrum or the ^{3}He spectrum if in the latter case a statistically weighted triplet n-p FSI contribution is included. In particular, if the expression is normalized to the high missing mass end, then the experimental data have values at the peak ($M_{56} = m_5 + m_6$) which are considerably larger than the W-M prediction. This is not surprising since along the locus where $M_{56} \gtrsim m_5 + m_6$ there is a region corresponding to the QFS condition, i.e. low spectator momenta. This leads to the conclusion that the QFS process dominates the peak at $M_{56} = m_5 + m_6$ and that the FSI represents only a rescattering correction.

However, one puzzling feature remains. This is the apparent agreement with the ^{3}He missing mass spectrum when only the singlet n-p FSI contribution is considered in calculating the W-M enhancement factor. A similar conclusion was reached by Fritts et al(Fr72). in their study of the ^{3}He(p,2p)pn reaction at 20 MeV.

An important difference exists in the shape of the two missing mass spectra, namely the $M_{56} = m_5 + m_6$ peak in the tritium spectrum is much narrower than the corresponding one in the ^3He spectrum. The reason for this difference may be seen in Fig. 6.2.4 where the four-body continua for the two reactions are plotted in a three-dimensional representation. In both spectra, enhancements are seen in regions satisfying the QFS condition. However, in regions of phase space not satisfying the QFS condition, the distribution of events is relatively flat in the ^3H spectrum but not so in the ^3He spectrum. Specifically, for the ^3He spectrum, a gradual rise in the distribution of events is seen for increasing T_4(or T_3) for a constant value of T_3 (or T_4) near the low energy cut-off (i.e. ~ 5 MeV). The reason for this behavior is not fully understood. It may be the manifestation of a FSI between the spectator pair and one of the detected protons. An investigation of the four-body continua for asymmetric spectator angle pairs should help to pinpoint the cause of this different behavior. Unfortunately, no such data exists at the present time. It is the enhancement near the region of (low T_3, high T_4) and (low T_4, high T_3) which causes the missing mass spectrum to have a much more gradual fall-off to the right of the peak at $M_{56} = m_5 + m_6$ in the case of ^3He.

Unless a complete theory exists which accounts for the interplay of QFS and FSI, it would seem that the study of reactions leading to a four-body final state such as the $^3H(p,2p)nn$

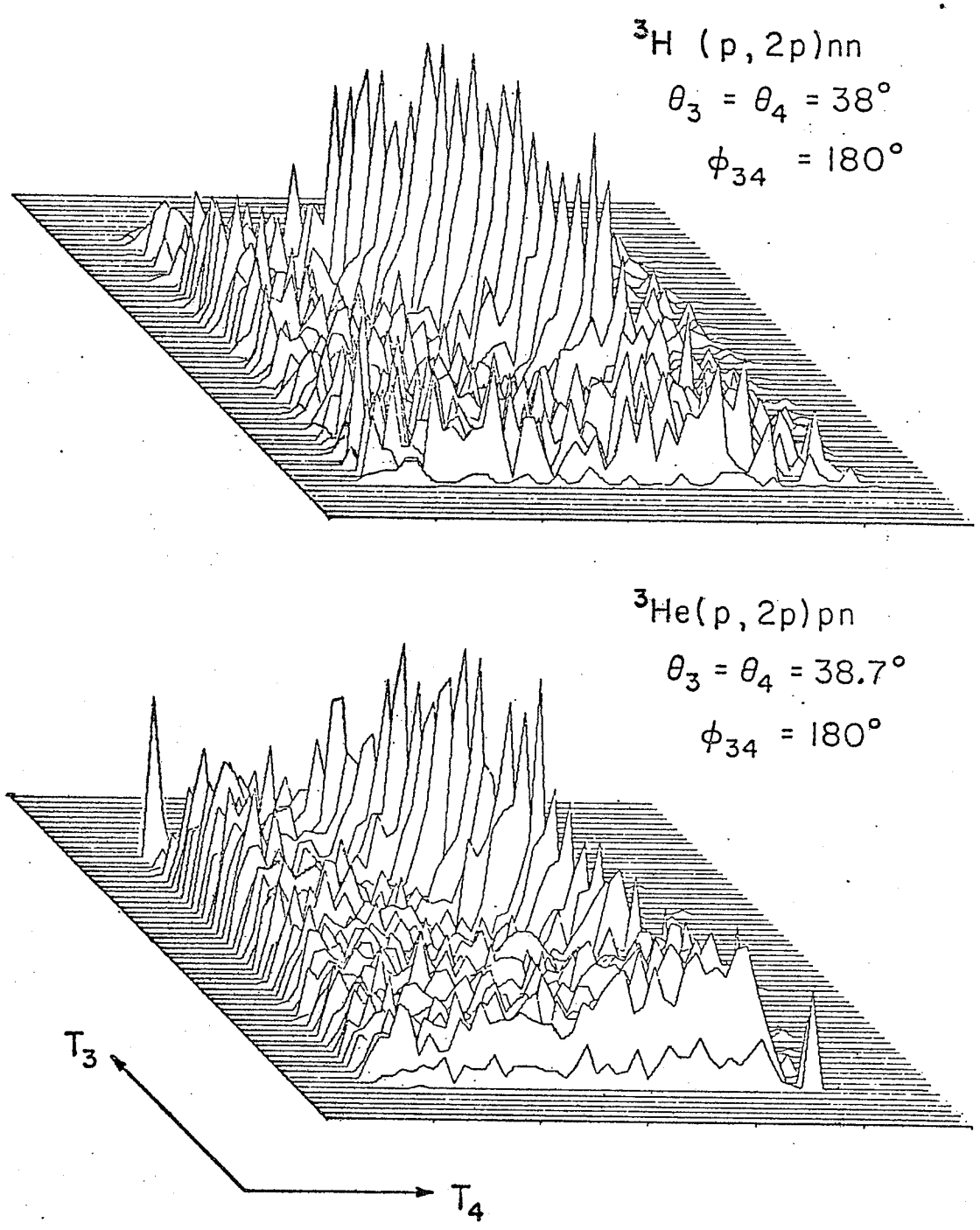

Fig.6.2.4: Comparison of the four-body continua for the reactions ^{3}H(p,2p)nn and ^{3}He(p,2p)pn, both displayed in a three-dimensional representation.

and ^{3}He(p,2p)pn reactions is not too suitable for extracting the N-N scattering parameters with any accuracy.

6.2.2 n-p final-state interaction in ^{3}H(p,pd)n

Fig.6.2.5 shows the projected proton energy spectrum for the ^{3}H(p,pd)n reaction at $\theta_p = \theta_d = 55^\circ$. The peak near $T_p = 9.5$ MeV corresponds to the final state interaction between the proton and the unobserved neutron while the peak at $T_p = 28$ MeV is due to phase space. Kinematic loci for different variables are plotted in Fig.6.2.6. The locus of relative energy T_{pn} is seen to have a minimum of 100 keV at $T_p = 9.5$ MeV. The phase space distribution function, plotted in relative units, is slowly varying in the region of minimum T_{pn} but is peaked at the high energy end. Moreover, the neutron momentum near the region of minimum T_{pn} is high thus ensuring that the FSI is relatively free from the QFS process.

Figures 6.2.7 (a),(b) and (c) show W-M fits to the FSI peak for $a_{np} = -18.0$ fm, -23.72 fm and -30.0 fm respectively. In each case, the fit is normalized to the peak value of the experimental data. In addition, the effect of adding varying contributions of the $^3S_1$ np FSI is examined. The n-p low energy scattering parameters used are those given in Table 6.2. The W-M fit is obtained from the expression:

$$d\sigma \sim R_3(\vec{P}, E)\,(F_s + W_t F_t) \qquad (4)$$

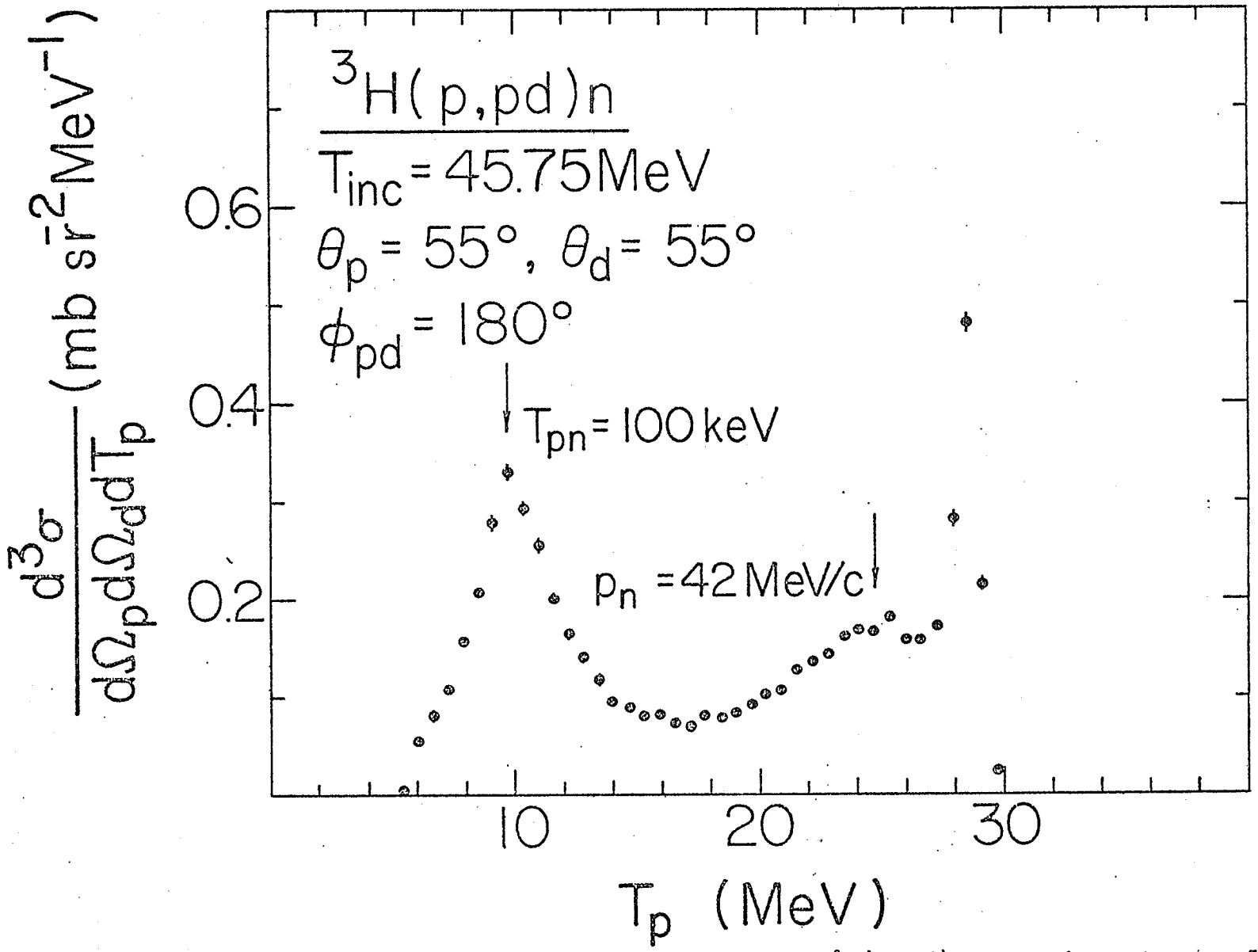

Fig. 6.2.5: Projected proton energy spectrum from the ^{3}H(p,pd)n reaction at θ_p = 55°, θ_d = 55°. The peak to the left is due to an n-p FSI while the peak at the high energy end is due to phase space alone.

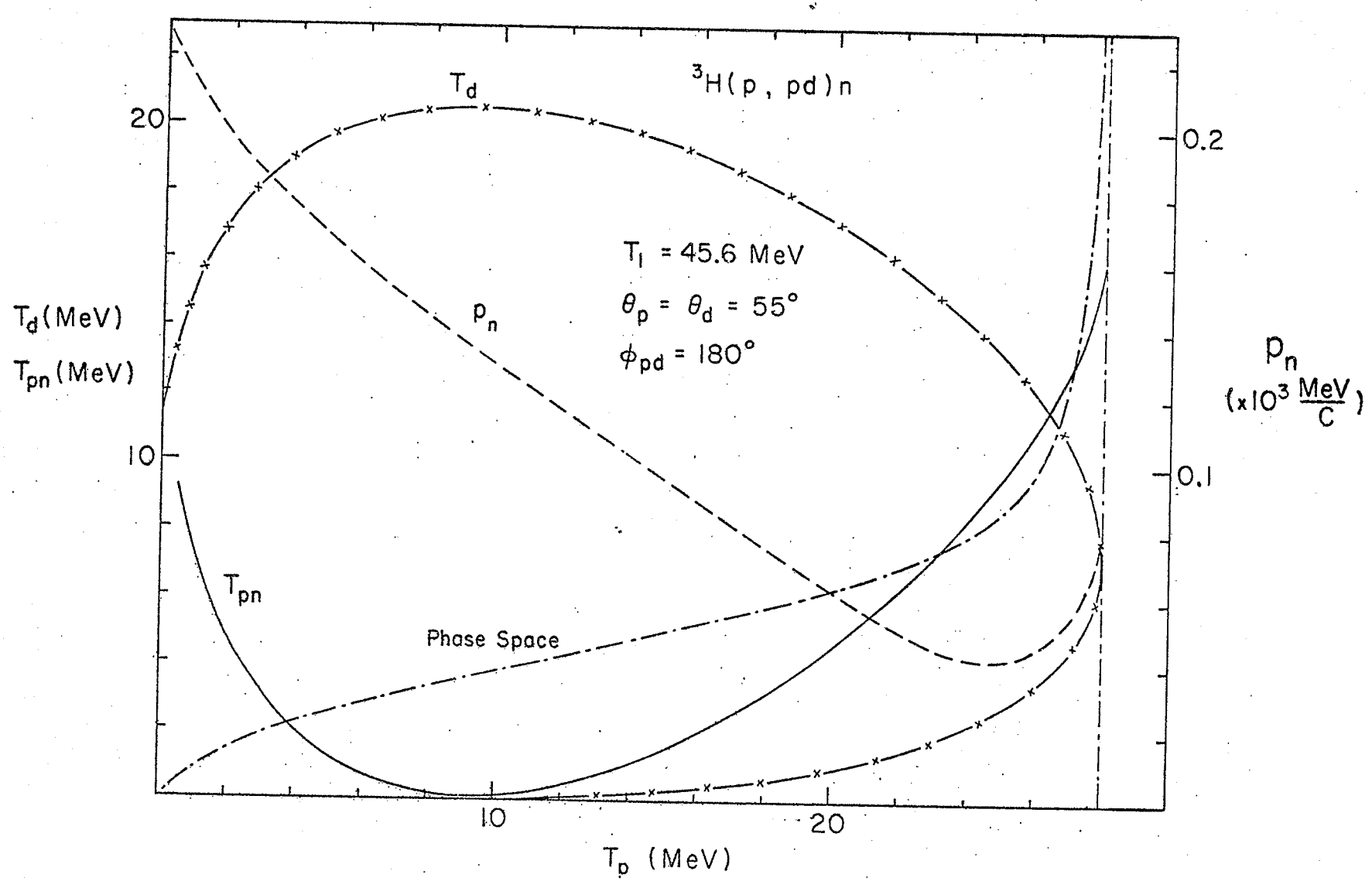

Fig. 6.2.6: Three-body kinematics for the $^3H(p,pd)n$ reaction at 45.6 MeV. All kinematic variables are plotted as function of T_p. The phase space factor is plotted in arbitrary units only.

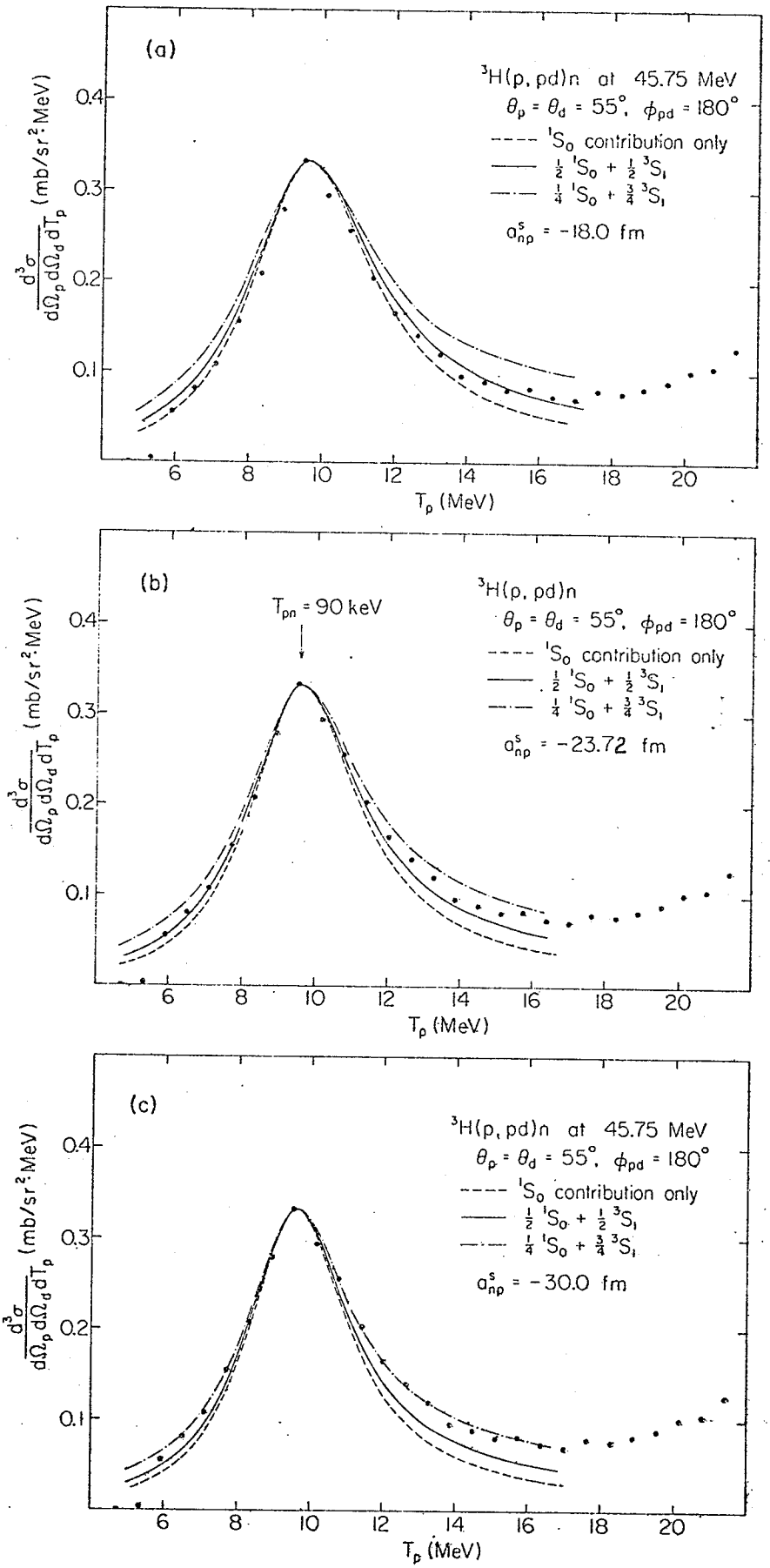

Fig.6.2.7: W-M fits to the n-p FSI for different values of the singlet n-p scattering length. A Gaussian resolution function of 0.5 MeV FWHM has been folded into the fits.

The form of the enhancement factor F (s and t refer respectively to the singlet and triplet contribution and W is a real number weighting factor) has been given in equation (22) of chapter 2. ρ_3, the three body phase space, is identical to the kinematic factor given in equation (12) of chapter 2. The width of the Gaussian resolution function is 0.5 MeV which was the experimentally determined value obtained from p-p coincidence spectra. This value can be used since the projection of the ^{3}H(p,pd)n reaction is made onto the proton axis. The results show that a reasonable fit cannot be obtained for a value of -18.0 fm for a_{np}^s. The best agreement was for a_{np}^s = -30.0 fm when only the singlet n-p FSI is included. Using the accepted value of a_{np}^s viz. -23.72 fm, a reasonable fit can only be obtained if an equally weighted $^3S_1$ n-p FSI is included. Widths of 0.4 MeV and 0.6 MeV for the Gaussian resolution function have been tried, but in each case the resulting change in the fit was insignificant.

In view of the absence of other competing processes, one is lead to conclude from the above results that the W-M model as described does not adequately explain the n-p FSI in the ^{3}H(p,pd)n reaction.

6.3 Search for excited states in ^{3}H

As already discussed in section 2.1, the presence of a resonance or excited state in ^{3}H will manifest itself as an enhancement in the four-body continuum of the $^{3}H(p,2p)nn$ reaction. Fig.6.3.1 shows the missing mass spectra for all the angle pairs studied. The peak at $M_{56} = m_5 + m_6$ was already understood to be due primarily to the quasi-free scattering process. However, both the 47.5°-47.5° and 55°-55° spectra show distinct enhancements over a smooth variation of the four-body continuum, indicated by the arrows. In Fig.6.3.2, the four-body continua are projected onto the T_3 axis for all the spectra which have enough counts to make the projected spectrum statistically meaningful. To avoid the QFS peak from masking any events which might be present inside the continuum, events with T_{56} between 0.0 and 1.8 MeV have been excluded. This procedure largely excludes the contribution from the $^{3}H(p,2p)[nn]$ reaction. The curves shown are the projected four-body phase space distributions (equation (11) in chapter 2) taking into account the experimental low energy cut-off in T_4 and the externally imposed exclusion of events near the boundary. The same normalization was used for all the spectra. It is apparent from these comparisons that the 47.5°-47.5° spectrum shows pronounced enhancements at $T_3 \sim 7$ MeV and $T_3 \sim 22$MeV while the 55°-55° spectrum shows enhancement at $T_3 \sim 8$ MeV.

To examine these enhancements more closely, the four-body continua for both spectra are plotted in a three-dimensional

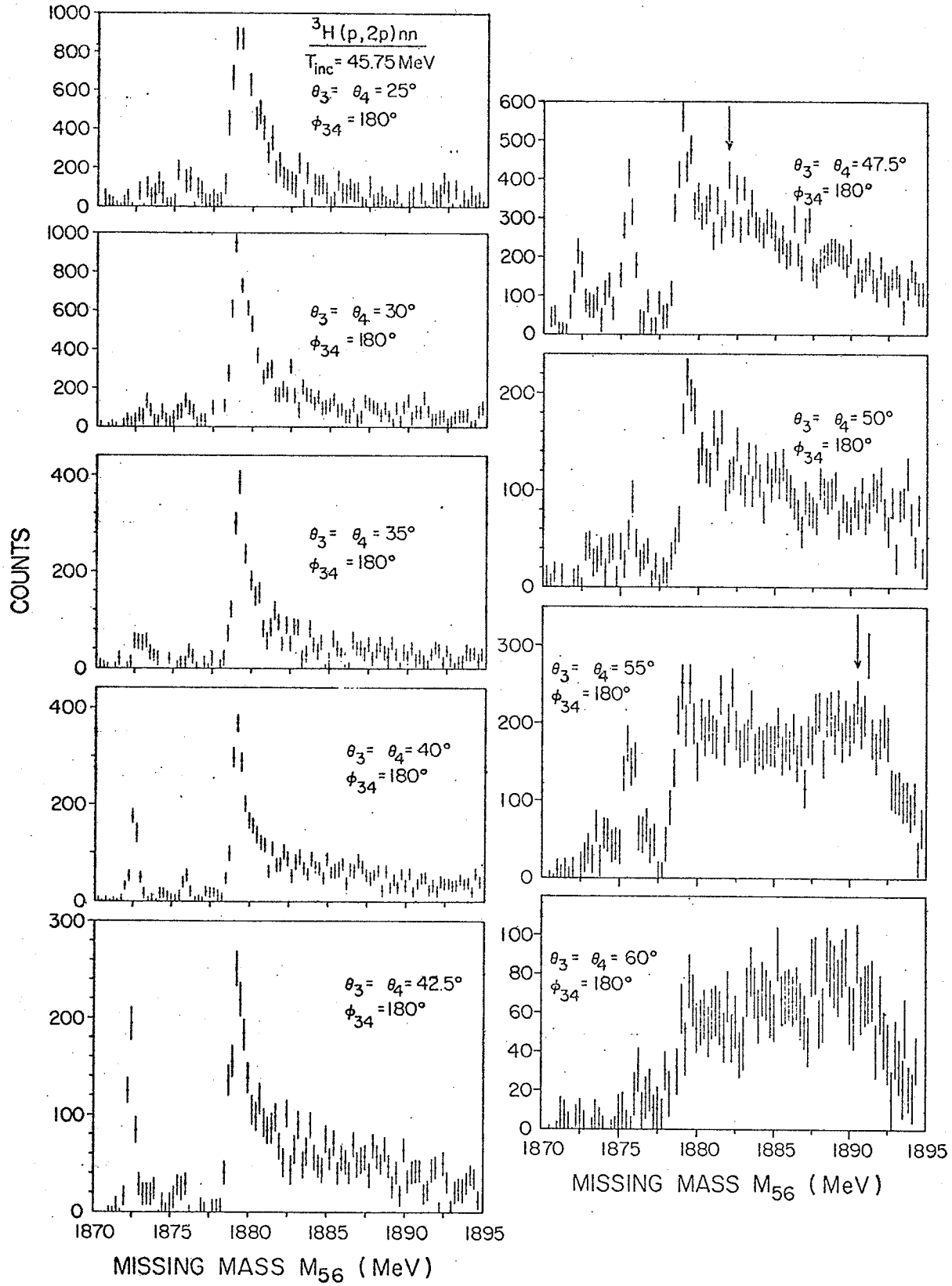

Fig.6.3.1 Missing mass spectra for the ^{3}H(p,2p)nn reaction at symmetric angle pairs.

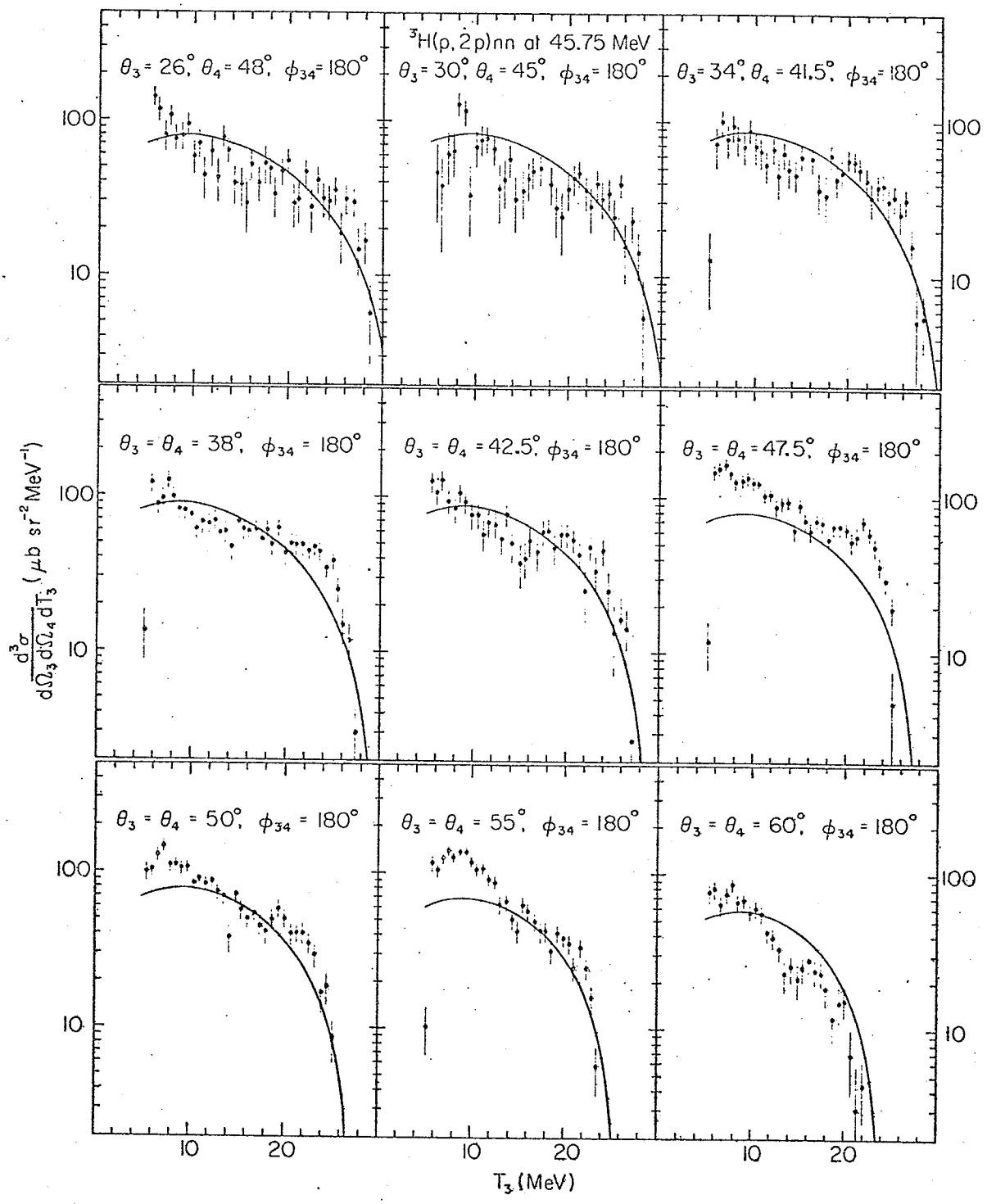

Fig.6.3.2: Data from the continuum of the reaction ^{3}H(p,2p)nn (excluding ^{3}H(p,2p)[nn]) projected onto the T_3 axis. The smooth curves are due to a direct numerical calculation of the four-body phase space distribution. The same normalization constant is used for all spectra.

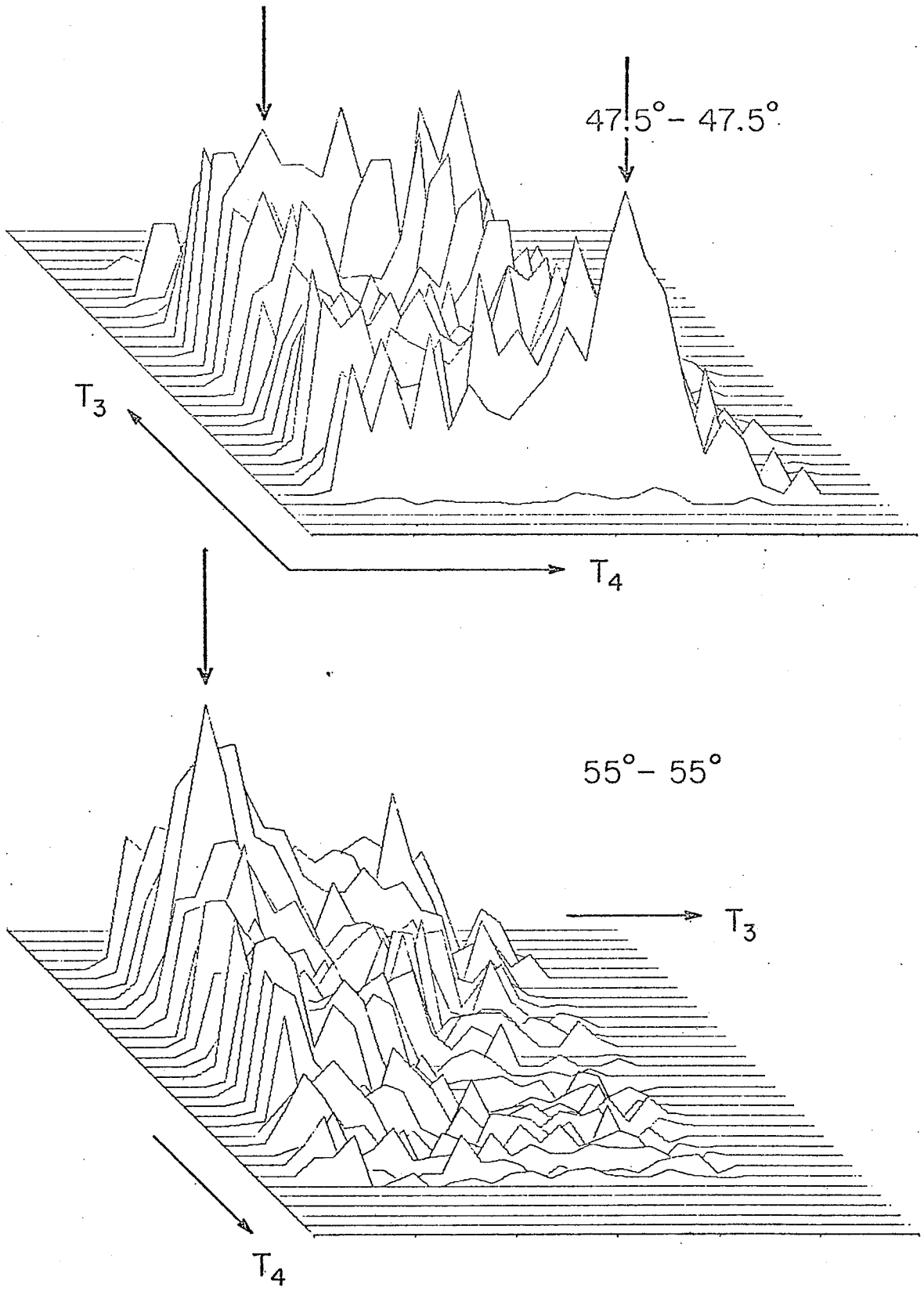

Fig.6.3.3: A three-dimensional display of the (T_3, T_4) spectra for the ^{3}H(p,2p)nn reaction at angle pairs 47.5-47.5 and 55-55. Arrows indicate regions of enhancement (see text for explanation).

representation in Fig.6.3.3. The regions of enhancement are now quite clear and two explanations can be given.

1. For the 47.5°-47.5° spectrum, the enhancement is due to the p-d* quasi-free scattering process in which the d* is detected as a proton with half the energy of the virtual particle. Kinematics corresponding to this process reproduces the observed positions of the enhancement.
2. For the 55°-55° spectrum, the only interpretation which is consistent with the data is the occurence of a

$$p + t \longrightarrow d^* + d^*$$

reaction in which the two virtual particles leave at 55° on opposite sides of the beam and are detected as protons with half the energy of the d* system. This process represents a hitherto unobserved reaction mechanism. It is possible that the proton picks up a neutron from the triton while existing in a n-d* configuration to form not a deuteron but a d* system. The process may be represented in the pole diagram shown in Fig.6.3.4.

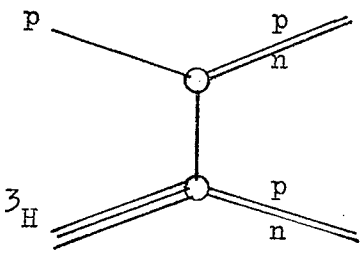

Fig.6.3.4: Possible diagram for the $p + t \longrightarrow d^* + d^*$ reaction.

The kinematics for this reaction also reproduces the observed peak position.

The $^{3}H(p,2p)nn$ continuum (not including $^{3}H(p,2p)[nn]$) appears to follow the four-body phase space distribution predictions. We see no evidence for any resonances in the ^{3}H three-body system. However, structures above the smooth phase space distribution are observed that can be interpreted as due to two-body processes. Specifically, the p-d* quasi-free scattering process and the reaction $p + t \longrightarrow d^* + d^*$. Furthermore, the appreciable enhancements observed indicates the importance of nucleon-nucleon correlations in the ^{3}H ground-state wave functions.

7. DISCUSSION

From the quasi-free scattering data, the momentum distributions of the d and [nn] systems in ^{3}H and of the d and d* systems in ^{3}He have been extracted within the framework of the PWIA. The comparison between the experimental and theoretical distributions shows that the PWIA adequately describes the shape of the ^{3}H ---> p-[nn] momentum distribution but requires the introduction of a cut-off radius in order to fit the ^{3}H ---> n-d and ^{3}He ---> p-d distributions. For the ^{3}H(p,pd)n and ^{3}He(p,2p)d reactions, the PWIA predicts cross sections which are a few times larger than the experimental ones. These results suggest that the multiple scattering contributions are important and lead primarily to a reduction in the cross sections.

In the present analysis, not all possible pole diagrams were included. For example, in the ^{3}H(p,pd)n reaction, two diagrams must also be considered in addition to the p-d QFS diagram (see Fig.7.1).

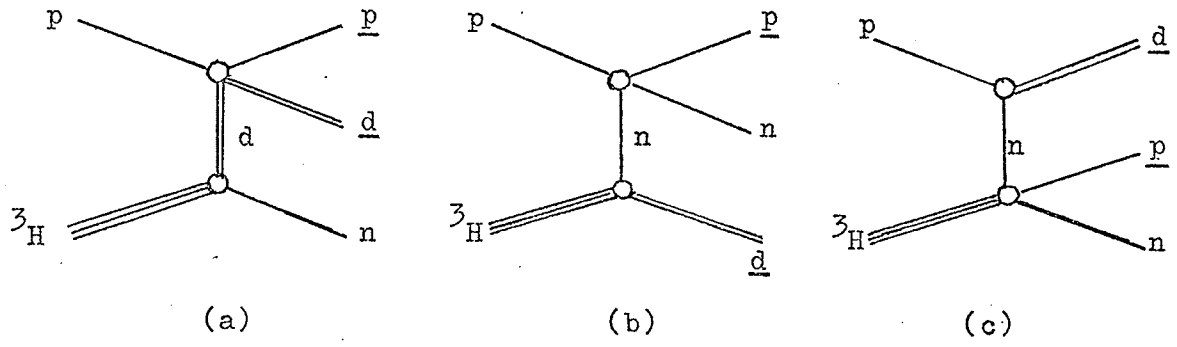

Fig.7.1: Pole diagrams for the ^{3}H(p,pd)n reaction. (a) represents p-d QFS , (b) represents p-n QFS and (c) represents the neutron pick-up diagram. Underlined particles are the detected particles.

These diagrams add coherently and destroy the factorizability of the cross section given by the impulse approximation. A similar situation

also exists in the ^{3}He(p,pd)p reaction (Ep71). Supporting evidence for the existence of the neutron pick-up process is given by the ^{3}H(p,pd)n projected energy spectra which deviate significantly from the PWIA predictions both in the magnitude and the position of the quasi-free scattering peak.

The data for the ^{3}H(p,2p)[nn] reaction show a preference for the final state energy prescription in the choice of the two-body off-the-energy-shell scattering amplitude although some improvement is obtained through the use of a more correct treatment e.g. the half-off-the-energy-shell T-matrix amplitude calculated using some model. Moreover, the p-p quasi-free scattering process in this reaction follows the PWIA predictions in that it is isotropic in the centre of mass scattering angle of the incident and struck protons.

It is apparent from results of the above studies that in order to obtain useful information about the dynamics of the three body system, a proper treatment of the multiple scattering series must be made. However, in the absence of such a detailed treatment, the use of Lehman's pole dominance approach (Le72) which takes into account all the non-negligible diagrams should prove useful. Calculations using this approach are currently being performed by Lehman and collaborators. Results of their calculation should be available soon.

The study of the missing mass spectra for the ^{3}H(p,2p)nn and ^{3}He(p,2p)pn reactions shows that in each case, the peak at $M_{56} = m_5 + m_6$ is completely dominated by the quasi-free scattering process. This is reflected in the good agreement in shape of the ^{3}H(p,2p) nn angular correlation data obtained with the PWIA and the failure of the Watson-Migdal model to give adequate fits to the missing mass spectra.

In addition, at large angle settings e.g. 55° - 55°, the spectator pole is no longer dominant while the unobserved pair still has a low relative energy at $M_{56} = m_5 + m_6$. A peak due to FSI is therefore still expected. However, no such peak is observed in the 55°-55° missing mass spectrum at the minimum of M_{56}. These facts lead to the conclusion that the peak at the minimum of M_{56} is due primarily to the quasi-free scattering process (spectator pole) while the FSI between the spectator pair only contributes as a rescattering correction. It follows therefore that the W-M formalism cannot be applicable in fitting the missing mass spectra. Only a detailed and complete theory which takes into account the interplay of QFS and FSI will permit the extraction of the low energy scattering parameters from these spectra.

A close examination of the four-body continua reveals distinct differences between the ^{3}H(p,2p)nn and ^{3}He(p,2p)pn reactions at their respective spectator angle pairs. These are the differences in the distribution of events near regions of low T_3, high T_4 and low T_4, high T_3. These differences cannot be attributed to experimental effects since both spectra were taken under the same experimental conditons including detectors, electronics, kinematics and beam properties. Moreover, the existing ^{3}He(p,2p)pn data taken earlier by another group at this laboratory under quite different experimental conditions agree with our present

data. No simple reason can be given for the difference in the four-body continua of these two reactions. However, an examination of the kinematics shows that regions corresponding to (low T_3, high T_4)/ (low T_4, high T_3) are also regions of low T_{35} / T_{45}. In these regions, particle 5 (the spectator) will be a n-p pair with low relative energy in the ^{3}He spectrum or a n-n pair with low relative energy in the ^{3}H spectrum. The fact that only enhancements are seen in the ^{3}He spectrum implies that possibly the correlation between a n-p pair and a proton is stronger than that between a n-n pair and a proton. The investigation of the ^{3}H(p,pn)pn and ^{3}He(p,pn)pp reactions under similar conditions should provide a conclusive test of this assumption.

Comparison of the continua for the ^{3}H(p,2p)nn reaction with four-body differential phase space distributions reveals strong enhancements at angle pairs 47.5°- 47.5° and 55°- 55°. These enhancements, however, are not associated with any resonance in the ^{3}H system but are due to pseudo two-body processes. In particular, the evidence points to p-d* QFS in the 47.5°-47.5° spectrum while the 55°-55° spectrum shows evidence for the $p + t \longrightarrow d^* + d^*$ reaction.

In conclusion, reactions leading to a four-body final state such as ^{3}H(p,2p)nn and ^{3}He(p,2p)pn can be understood in terms of phase space distribution and dominant two-body processes where they are kinematically allowed. No evidence was found for the existence of an excited state or resonance in the ^{3}H system.

The plane wave impulse approximation does not fully describe the quasi-free scattering process but does represent the driving term for the process. Although the p-p QFS process is isotropic, in accordance with the PWIA, the angular dependence of the $^{3}H(p,pd)n$ reaction indicates the existence of other reaction mechanisms. This suggests that no one reaction can be described by a single pole diagram. Moreover, the interference effects between the various pole graphs contributing to the same reaction must also be investigated. An exact treatment in the Faddeev formalism appears to be in order.

In the presence of the competing QFS process, the Watson-Migdal model is unable to predict the FSI behavior of the spectator pairs in both reactions. Moreover, it also fails to predict the shape of the n-p FSI peak in the projected energy spectrum for the $^{3}H(p,pd)n$ reaction.

BIBLIOGRAPHY

Am63 R.D.Amado, Phys.Rev.132,485(1963).

Aa64 R.Aaron, R.D.Amado and Y.Y.Yam, Phys.Rev.136,B650(1964); Phys.Rev.Letters 13,574(1964).

Aa65 R.Aaron, R.D.Amado and Y.Y.Yam, Phys.Rev.140,B1291(1965).

Ar71 H.Arenhovel, M.Danos, and H.T.Williams, Nucl.Phys.A162, 12(1971).

Al73 R.G.Allas, L.A.Beach, R.O.Bondelid, E.M.Diener, E.L.Petersen, J.M.Lambert, P.A.Treado and I.Slaus, to be published.

Be64 B.L.Berman,L.J.Koester,Jr.,and J.H.Smith,Phys.Rev.133,B117(1964).

Bl52 J.M.Blatt and V.F.Weisskopf, Theoretical Nuclear Physics (John Wiley and Sons, New York,1952), Chapter VIII.

Ba66 T.E.Baumgartner, H.E.Conzett, E.Shield, and R.J.Slobodrian, Phys.Rev.Letters 16,105(1966).

Bu66 J.J.Burgerjon,B.Hird, F.Konopasek and K.G.Standing, IEEE Tran. on Nucl. Sci.,NS-13,422(1966).

Ba68 E.Bar-Avraham and L.C.Lee, Nucl. Instr. and Meth. 64,141 (1968).

Br69 C.N.Bressel, A.K.Kerman, and B.Rouben, Nucl.Phys. A124, 624(1969).

Ba70 I.M.Barbour, and A.C.Phillips, Phys.Rev.C1,165(1970).

Br72 W.H.Breunlich, S.Tagesen, W.Bertl, and A.Chaloupka in reference (Fe72) p.100.

Bu72 S.N.Bunker, M.Jain, C.A.Miller, J.M.Nelson, and W.T.H.van Oers, Can.J.Phys.50,295(1972).

Bo73 D.I.Bonbright, private communication.

Ba64 B.M.Bardin and M.E.Rickey, Rev.Sci.Instr.35,962(1964).

Ch54 O.Chamberlain and M.O.Stern, Phys.Rev.94,666(1954)

Cr61 A.H.Cromer, Phys.Rev.129,1680(1961).

Cr63 A.H.Cromer and E.H.Thorndike, Phys.Rev.131.1680(1963).

Co63 H.Collard, R.Hofstadter, A.Johansson, R.Parks, M.Ryneveld, A.Walker, R.Yearian, R.B.Day, and R.T.Wagner, Phys.Rev. Letters 11,132(1963).

Co65 H.Collard, R.Hofstadter, E.B.Hughes, A.Johansson, M.R. Yearian, R.B.Day, and R.T.Wagner, Phys.Rev.138,B57(1965).

Ch69 C.C.Chang, E.Bar-Avraham, H.H.Forster, C.C.Kim, P.Tomas, and J.W.Verba, Nucl. Phys. A136,337(1969).

Ca70 R.T.Cahill and I.H.Sloan, in Three Body Problem in Nuclear and Particle Physics,ed. by J.S.C.McKee and P.M.Rolph, (North-Holland Publishing Company, Amsterdam, 1970),p337.

Co72 A.A.Cowley, V.K.C.Cheng, H.G.Pugh, P.G.Roos and R.Woody, University of Maryland Progress Report on Nucl. Phys.1972, p.19.

Ch73 V.K.C.Cheng, Ph.D.thesis, University of Maryland, 1973.

Da68 J.C.Davis and H.Barschall, Phys.Letters 27B,636(1968).

De71 J.D.Detch,Jr., R.L.Hutson, N. Jarmie and J.H.Jett, Phys. Rev.C4,52(1971).

Ep71 M.B.Epstein, I.Slaus, D.Shannon, J.R.Richardson, J.W.Verba, H.H.Forster, C.C.Kim and D.Y.Park, Phys.Letters36B,305(1972).

Fa60 L.D.Faddeev, Zh.Eksperim.iTeor.Fiz. 39,1459(1960) Transl.: Soviet Phys. - JETP 12,1014(1961).

Fe65 V.N:Fetisov, A.N.Gorbunov and A.T.Varfolomeev, Nucl.Phys. 71,305(1965).

Fo62 R.Fox, Phys.Rev.125,311(1962).

Fe55 H.Feshbach and S.I.Rubinow, Phys.Rev. 98,188(1955)

Fr71 R.Frascaria, V.Comparat, N.Marty, M.Morlet, A.Willis and N.Willis, Nucl.Phys.A178,307(1971).

Fe72 Few Particle Problems in the Nuclear Interaction, ed. by I.Slaus, R.P. Haddock, S.A.Moszkowski and W.T.H.van Oers, (North-Holland Publishing Company, Amsterdam,1972).

Fr72 M.J.Fritts and P.D.Parker, Nucl.Phys.A198,109(1972)

Fr72b M.J.Fritts, Ph.D. thesis, Yale University (1972), appendix B.

Fr74 R.Frascaria, V.Comparat, N.Marty, M.Morlet and A.Willis, to be published.

Gu51 J.C.Gunn and J.Irving, Phil.Mag.42,1353 (1951).

Gi64 J.Gillespie, Final-state Interactions (Holden-Day, San Francisco, 1964)

Gr64 T.A.Griffy and R.J.Oakes, Phys.Rev.135,B1161(1964).

Gu64 M.L.Gursky and L.Heller, Phys.Rev.136,B1693(1964).

Gi67 B.F.Gibson and G.B.West, Nucl.Phys. 131,349(1967).

Gr70 E.E.Gross, E.V.Hungerford, J.J.Malanigy, and R.Woods, Phys. Rev.C1,1365(1970).

Hu57 L.Hulthen and M.Sugawara, in Handbuch der Physik, edited by S.Flugge (Springer-Verlag, Berlin,1957),Vol.39.

Ha64 R.Hagedorn, Relativistic Kinematics (W.A. Benjamen, N.Y., 1964) Chapter 7.

Hu66 E.B.Hughes, M.R. Yearian, and R.Hofstadter, Phys.Rev.151, 841(1966).

He67 L.Heller, Rev.Mod.Phys.39,584(1967).

He67b E.M.Henley, F.Richards, and D.U.L.Yu, Nucl.Phys.A103, 361(1967).

He69 E.M.Henley in Isospin in Nuclear Physics, ed., D.H.Wilkinson (North-Holland : Amsterdam, 1969)

He72 E.M.Henley, p.221 in reference (Fe72).

He72b E.M.Henley and T.E.Keliher, Nucl.Phys.A189,632(1972)

Ha73 R.D.Haracz and T.K.Lim, Phys.Rev.Letters31,1263(1973).

Jo64 A.Johansson, Phys.Rev.136,B1030(1964).

Ja66 J.F.Janni, Technical Report No. AFWL-TR-65-150, Air Force Weapons Laboratory Technical Report (Sept.,1966)

Ja69 M.Jain, Ph.D. thesis, University of Maryland,1969.

Ja74 M.Jain, S.N.Bunker, C.A.Miller, J.M.Nelson and W.T.H.van Oers, Lett.Nuovo Cimento, in press.

Ki72 P.Kitching, G.A.Moss, W.C.Olsen, W.J.Roberts, J.C.Alder, W.Dollhopf, W.J.Kossler, C.F.Perdrisat, D.R.Lehman and J.R.Priest, Phys.Rev. C6,769(1972)

Ku72 B.Kuhn, H.Kumpf, S.Parzhitsky,and S.Tesch, Nucl.Phys. A183 (1972)

Le71 D.R.Lehman, Phys.Rev.C3,1827(1971).

Le72 D.R.Lehman, Phys.Rev.C6,2023(1972).

Mi55 A.B.Migdal, Soviet Phys.- JETP 1, 2 (1955).

Mo64 M.J.Moravsik, Phys.Rev.136,B624(1964).

Ma66 M.H.MacGregor, R.A.Arndt and R.M.Wright, UCRL Report No. 50426, April 1966.

Mi69 M.D.Miller, M.S.Sher, P.Signell, N.R.Yoder, and D.Marker, Phys.Lett.30B,157(1969).

Ma70 D.J.Margaziotis, G.Paic, J.C.Young, J.W.Verba, W.J.Braithwaite, J.M.Cameron, D.W.Storm and T.A.Cahill, Phys.Rev. C2,2050(1970).

Mc70b M.McMillan and D,Maroun, Nucl.Phys.A159,661(1970).

Mc71 M.McMillan, Phys.Rev.C3,1702(1971).

Mi72 C.A.Miller, private communication.

Mc70 J.S.McCarthy, I.Sick, R.R.Whitney, and M.R.Yearian, Phys. Rev.Letters 25,884(1970).

No63 H.P.Noyes,Phys.Rev.130,2025(1963).

No64 H.P.Noyes, Phys.Rev.Letters12,171(1964).

No68 H.P.Noyes and H. Fieldeldey, Three-Particle Scattering in Quantum Mechanics, ed. J.Gillespie and J.Nuttall (W.A. Benjamin, Inc., New York, Amsterdam, 1968) p.195.

Oe67 W.T.H.van Oers and I.Slaus, Phys.Rev.160,853(1967).

Or69 S.Oryu, S.Shioyama and Y.Takahashi,Progr.Theoret. Phys. (Kyoto) 42, 425 (1969)

Oe71 W.T.H.van Oers, Particles and Nuclei 2,207(1971).

Oe73 W.T.H.van Oers, M.Jain and S.N.Bunker, Nucl.Instr.and Meth. 112, 405 (1973).

Pa66 A.C.Paul and B.T.Wright, IEEE Tran. on Nucl. Sci., NS-13, 74(1966)

Pa67 A.C.Paul, UCLA Technical Report p79 (1967).

Pu74 H.G.Pugh, P.G.Roos, A.A.Cowley, V.K.C.Cheng and R.Woody, to be published. See also 1973 Progress Report, Cyclotron Laboratory, University of Maryland.

Ro69 J.G.Rogers, Ph.D. thesis, UCLA,1969.

Re70 E.F.Redish, G.J.Stephenson, Jr., and G.M.Lerner, Phys.Rev. C2,1665(1970).

Ro72 J.G.Rogers and D.P.Saylor, Phys.Rev. C6,734(1972).

Sc64 L.J.Schiff, Phys.Rev.133,802(1964).

Sk64 O.Skjeggestad, Proceedings of the 1964 Easter School for physicists, CERN Report 64-13.

Sh66 I.S.Shapiro, Proceedings of the International School of Physics, "Enrico Fermi ", Varenna, XXXVIII, 210,(Academic Press, New York, 1966).

Sm64 R.Smythe, Rev.Sci.Instr. 35, 1197(1964).

S167 I. Slaus, Simple Nuclear Systems and Nuclear Interaction in Few Body Problems Light Nuclei and Nuclear Interactions, ed. by G.Paic and I.Slaus, (Gordon and Breach, Science Publishers, 1967) Vol.I, p83.

S170 I.Slaus, Final State Interactions and Quasi-free scattering in Three Body Problem in Nuclear and Particle Physics, ed. by J.S.C.McKee and P.M.Rolph, (North-Holland Publishing Company, Amsterdam, 1970).

Se70 J.D.Seagrave, in reference sited above, p.41; Allred et al., Phys.Rev. 38, 433(1952); Brolley et al., Phys.Rev. 117, 1307 (1960); Wilson et al., Nucl.Phys. A130, 624(1969); Kocher et al., Nucl.Phys. A132, 455(1969); Cahill etal., Phys. Rev. C4, 1499(1971).

Sh70 M.S.Sher, P.Signell and L.Heller, Annals of Physics 58, 1(1970).

S171 I.Slaus, M.B.Epstein, G.Pais, J.R.Richardson, D.L.Shannon, J.W.Verba, H.H.Forster, C.C.Kim, D.Y.Park and L.C.Welch, Phys.Rev.Letters 27, 751(1971).

Sa72 R.M.Salter, M.Zeller, R.P.Haddock, D.Nygren and J.B.Czirr in reference (Fe72) p.112.

S173 I.Slaus, R.G. Allas, L.A.Beach, R.O.Bondelid, E.L.Petersen, J.M.Lambert and D.L.Shannon, Phys.Rev. C8, 444(1973).

Wa52 K.M.Watson, Phys.Rev. 68, 1163(1952).

Wa70 J.W.Watson, Ph.D. thesis, University of Maryland, 1970 ; private communication.

Wa71 R.E.Warner, G.C.Ball, W.G.Davis, A.J.Ferguson, and J.S. Forster, Phys.Rev.Letters 27, 961(1971).

Wi72 B.J.Wielinga, A.D.IJpenberg, K.Mulder, R.van Dantzig and I.Slaus in reference(Fe72) p.687; B.J.Wielinga, Ph.D. thesis, University of Amsterdam, IKO, 1972 (unpublished).

Wa73 J.M.Wallace, Phys. Rev. C7, 10 (1973); Phys.Rev. C8, 1275(1973).

Wa74 J.W.Watson, C.A.Miller, private communication.

Yu35 Yukawa,H Proc.phys.-math.Soc., Japan, 17, 48(1935).

Ya54 Y.Yamaguchi, Phys.Rev. 95, 1628(1954).

Zu64 Č.Zupančič, Kinematics of multiparticle reactions, MIJS report R-429, June 1964.

Ze72 B.Zeitnitz, R.Maschuw, P.Suhr and W.Ebenhoh in reference (Fe72) p.117.

APPENDIX I

Derivation of the two-body phase space in the centre of mass system

Consider particles 5 and 6 in their centre of mass system of total energy $\mathcal{E}$, we have from definition

$$R_2(0,\mathcal{E}) = \int \frac{d\vec{p}_5}{2E_5}\,\frac{d\vec{p}_6}{2E_6}\,\delta^3(\vec{p}_5+\vec{p}_6)\,\delta(E_5+E_6-\mathcal{E}) \qquad (1)$$

Integrating over particle 6 gives

$$R_2(0,\mathcal{E}) = \int \frac{d\vec{p}_5}{2E_5}\,\frac{1}{\partial E_6(p_5)}\,\delta(E_5+E_6(p_5)-\mathcal{E})$$

$$= \int \frac{p_5^2\,dp_5\,d\Omega_5}{4E_5E_6(p_5)}\,\delta(E_5+E_6(p_5)-\mathcal{E}) \qquad (2)$$

Integrating over $d\Omega_5$ yields 4π since particles are emitted isotropically in the centre-of-mass.

Using the δ-function relations

$$\int_a^b f(x)\,\delta(x-c)\,dx = f(c) \quad \text{for} \quad a<c<b$$
$$= 0 \quad \text{for} \quad c<a \text{ or } c>b$$

and

$$\int \delta(\phi(x))\,dx = \int \frac{\delta(y)}{\phi'(x)}\,dy \quad ,$$

integrating over p_5 yields

$$R_2(0,\mathcal{E}) = \frac{\pi p_5^2}{E_5E_6}\left(\frac{p_5}{E_5}+\frac{p_5}{E_6}\right)^{-1}$$

$$= \frac{\pi p_5}{\mathcal{E}} \qquad (3)$$

To express this in terms of the invariant mass M_{56}, we use the relations

$$M_{56} = \varepsilon = \sqrt{m_5^2 + p_5^2} + \sqrt{m_6^2 + (-p_5)^2}$$

yielding

$$p_5 = \frac{\left\{ [M_{56}^2 - (m_5 + m_6)^2][M_{56}^2 - (m_5 - m_6)^2] \right\}^{\frac{1}{2}}}{2 M_{56}}$$

Hence, finally we have

$$\underline{\underline{R_2(0, M_{56}) = \frac{\pi}{2 M_{56}^2} \left\{ [M_{56}^2 - (m_5 + m_6)^2][M_{56}^2 - (m_5 - m_6)^2] \right\}^{\frac{1}{2}}}} \quad \text{- - - (4)}$$

APPENDIX II

Evaluation of the Fourier transform of the overlap integral between the spatial wave function of the target nucleus and the residual nucleus

The Irving-Gunn wave function for the ^3He (or ^3H) system is

$$\psi_{^3He}(r,\rho) = \frac{A \exp\left\{-\tfrac{1}{2}\alpha\left(2r^2 + 3/2\,\rho^2\right)^{1/2}\right\}}{\left(2r^2 + 3/2\,\rho^2\right)^{1/2}} \qquad (1)$$

where $\vec{\rho} = \vec{r}_{23}$, $\vec{r} = \vec{r}_{12} + \vec{\rho}/2 = \vec{r}_{13} - \vec{\rho}/2$

$$A = \frac{3^{1/4}\alpha^2}{\sqrt{2}\,\pi^{3/2}}$$

$\alpha =$ 0.77 fm^{-1} for ^3He

1.00 fm^{-1} for ^3H

The value of α for ^3He is that obtained in the analysis of the photodisintegration (Be64). The same α was also found to fit the charge form factor and the Coulomb energy of ^3He. In the case of ^3H, α is obtained from variational calculation which gives the best binding energy for the ^3H system (Gu51). The Hulthén wave function for the deuteron is

$$\psi_d(\rho) = \frac{N\left(e^{-a\rho} - e^{-b\rho}\right)}{\sqrt{4\pi}\;\rho} \qquad (2)$$

where $N = \dfrac{\left[2ab\,(a+b)\right]^{1/2}}{(b-a)}$

$a = 0.231\ fm^{-1}$

$b = 1.440\ fm^{-1}$

The Fourier transform of the overlap integral is

$$\Phi(\vec{p}) = \int d^3\rho \int d^3r \; \psi_{3/2}(\vec{\rho},\vec{r}) \; e^{\,i\vec{p}\cdot\vec{r}} \; \psi_d(\rho) \qquad (3)$$

where $\vec{p}$ is the momentum of the struck particle before the collision

$$= AN \int d^3\rho \int d^3r \; \frac{\exp\left[\, i\vec{p}\cdot\vec{r} - \frac{1}{2}\alpha\left(2r^2 + \frac{3}{2}\rho^2\right)^{1/2}\right]}{\left(2r^2 + \frac{3}{2}\rho^2\right)^{1/2}}$$

$$\times \left(\frac{e^{-a\rho} - e^{-b\rho}}{\rho} \right) \qquad (4)$$

To evaluate this integral , we follow the method of reference (Gr64). Introducing the Fourier transform of the deuteron wave function

$$\frac{1}{(2\pi)^3} \int d^3x \; e^{\,i\vec{k}\cdot\vec{x}} \; \psi_d(\vec{x}) = \frac{N(b^2-a^2)}{4\pi^{5/2}(a^2+k^2)(b^2+k^2)} \qquad (5)$$

The integral then becomes

$$\Phi(\vec{p}) = \frac{AN(b^2-a^2)}{4\pi^{5/2}} \int \frac{d^3\vec{k}}{(a^2+k^2)(b^2+k^2)} \int d^3\rho \int d^3r$$

$$\frac{\exp\left[\, i(\vec{p}\cdot\vec{r} + \vec{k}\cdot\vec{\rho}) - \frac{1}{2}\alpha\left(2r^2 + \frac{3}{2}\rho^2\right)^{1/2}\right]}{\left(2r^2 + \frac{3}{2}\rho^2\right)^{1/2}} \qquad (6)$$

Next, we transform the two three-dimensional integrals over $\vec{\rho}$ and $\vec{r}$ into one six-dimensional integral with the substitution

$$R_{1,2,3} = \left(\frac{3}{8}\right)^{1/2} \alpha \vec{\rho} \quad ; \quad R_{4,5,6} = \left(\frac{1}{2}\right)^{1/2} \alpha \vec{r} \tag{7}$$

and

$$Q_{1,2,3} = \left(\frac{8}{3}\right)^{1/2} \left(\frac{1}{\alpha}\right) \vec{p} \quad ; \quad Q_{4,5,6} = \left(\frac{\sqrt{2}}{\alpha}\right) \vec{k}$$

The six-dimensional integral can then be written as

$$\Phi(\vec{p}) = \frac{AN(b^2-a^2)}{4\pi^{5/2}} \int \frac{d^3\vec{k}}{(a^2+k^2)(b^2+k^2)} \cdot$$

$$\frac{64\alpha}{3^{3/2}\alpha^6 2} \int \frac{\exp(i\vec{Q}\cdot\vec{R} - R]}{R} d^6R \tag{8}$$

The angular part of the six dimensional integral may be performed by expanding the plane wave in Gegenbauer polynomials and using the integral properties

$$\int \frac{\exp[i\vec{Q}\cdot\vec{R} - R]}{R} d^6R = \frac{8\pi^3}{Q^2} \int_0^\infty e^{-R} J_2(QR) R^2 dR$$

$$= \frac{\alpha^2}{\pi^{1/2}} \frac{\Gamma(5/2)}{(1+Q^2)^{5/2}} \tag{9}$$

where Γ are the tabulated hypergeometric functions.

Equation 8 can now be expressed as

$$\Phi(\vec{p}) = \frac{256\pi^{3/2}(b^2-a^2)AN}{\sqrt{3}\,\alpha^5} \times$$

$$\int_0^\infty \frac{k^2 dk}{(a^2+k^2)(b^2+k^2)\left[1+\left(\frac{8k^2}{3\alpha^2}+\left(\frac{\alpha^2 p^2}{\alpha^2}\right)\right]^{5/2}\right.} \tag{10}$$

The integral in equation 10 can be evaluated analytically or by simple numerical techniques e.g. Simpson's rule.

The Fourier transform of the overlap integral between a trion wave function and a scattering wave function (e.g. d* or a [nn] system) cannot be reduced to an analytic form and numerical integration becomes the only means of evaluation.

We shall consider the case of the overlap of $\psi_{^3He}\,\psi_{d^*}$ or $\psi_{^3H}\,\psi_{[nn]}$

The Fourier transform of the overlap integral is

$$\Phi(\vec{p}) = \frac{1}{(2\pi)^{3/2}} \int_0^\infty d^3\rho \int_0^\infty d^3r \; e^{i\vec{p}\cdot\vec{r}} \; \frac{e^{-\frac{1}{2}\alpha(2r^2+\frac{3\rho^2}{2})^{\frac{1}{2}}}}{(2r^2+\frac{3}{2}\rho^2)^{\frac{1}{2}}} \cdot \frac{a_s(1-\frac{\rho}{a_s}-e^{-\xi\rho})}{\rho} \qquad (11)$$

where $\frac{a_s(1-\rho/a_s-e^{-\xi\rho})}{\rho}$ is the two-body scattering wave function and ξ is a constant related to a_s, the singlet scattering length.

Integrating over the angular part yields

$$\Phi(p) = \frac{4\cdot 3^{\frac{1}{4}}\alpha^2 \cdot a_s}{\pi} \int_{r=0}^{\infty}\int_{\rho=0}^{\infty} \frac{e^{-\frac{1}{2}\alpha(2r^2+\frac{3}{2}\rho^2)^{\frac{1}{2}}}}{(2r^2+\frac{3}{2}\rho^2)^{\frac{1}{2}}} \left(1-\frac{\rho}{a_s}-e^{-\xi\rho}\right) \frac{\sin pr}{r} \rho\, d\rho\, r\, dr \qquad (12)$$

This two-dimensional integral can be evaluated using standard numerical techniques (e.g. Gaussian quadruture). A cut-off radius is introduced when the lower limit r=0 is replaced by $r=r_c$.

In the above foumule, $\hbar = c = 1$, $\vec{p} = \hbar\vec{k}$ is in fm^{-1}, r is in fm so that $|\Phi(p)|^2$ is in fm^3.

APPENDIX III

Gaussian resolution folding

Given a theoretical spectrum N(E), N_i represents the number of counts (events) at channel i with a corresponding energy $E_i - E_i + \Delta E_i$. The effect of finite resolution is to produce a redistribution of events in each channel. If this redistribution follows a Gaussian distribution, the folded spectrum N'(E) will have for it's j^{th} channel

$$N_j' = \frac{1}{\sqrt{2\pi}} \sum_{i=-\infty}^{\infty} \frac{\Delta E_j}{\sigma} N_i \; e^{-\frac{(E_i - E_j)^2}{2\sigma^2}} \qquad (1)$$

where ΔE_j represents the channel width $E_j - E_{j-1}$ and N_i represents the number of counts at channel i in the theoretical spectrum. The standard deviation σ is related to the full-width-at-half-maximum (FWHM) of the Gaussian by

$$\sigma = \frac{FWHM}{\sqrt{8 \ln 2}} \qquad (2)$$

Moreover, because of the rapidly decreasing behavior of the exponential term, only channels near j give significant contribution and need be summed in expression (1). It is also evident that the total number of counts in the folded spectrum remains unchanged from the theoretical one.